

HEXACYANOFERRATE-BASED NANOCOMPOSITES
FOR THE ELECTROCHEMICAL SENSING OF
HYDROGEN PEROXIDE AND NICOTINE

LEE PUI KEE

FACULTY OF SCIENCE
UNIVERSITI MALAYA
KUALA LUMPUR

2020

HEXACYANOFERRATE-BASED NANOCOMPOSITES
FOR THE ELECTROCHEMICAL SENSING OF
HYDROGEN PEROXIDE AND NICOTINE

LEE PUI KEE

**THESIS SUBMITTED IN FULFILMENT OF THE
REQUIREMENTS FOR THE DEGREE OF DOCTOR OF
PHILOSOPHY**

**DEPARTMENT OF CHEMISTRY
FACULTY SCIENCE
UNIVERSITI MALAYA
KUALA LUMPUR**

2020

UNIVERSITI MALAYA
ORIGINAL LITERARY WORK DECLARATION

Name of Candidate: **LEE PUI KEE**

Matric No: **SHC 160012**

Name of Degree: **DOCTOR OF PHILOSOPHY**

Title of Project Paper/Research Report/Dissertation/Thesis (“this Work”):

**HEXACYANOFERRATE-BASED NANOCOMPOSITES FOR
THE ELECTROCHEMICAL SENSING OF HYDROGEN PEROXIDE
AND NICOTINE**

Field of Study:

ANALYTICAL CHEMISTRY (ELECTROCHEMIST

RY)

I do solemnly and sincerely declare that:

- (1) I am the sole author/writer of this Work;
- (2) This Work is original;
- (3) Any use of any work in which copyright exists was done by way of fair dealing and for permitted purposes and any excerpt or extract from, or reference to or reproduction of any copyright work has been disclosed expressly and sufficiently and the title of the Work and its authorship have been acknowledged in this Work;
- (4) I do not have any actual knowledge nor do I ought reasonably to know that the making of this work constitutes an infringement of any copyright work;
- (5) I hereby assign all and every rights in the copyright to this Work to the University of Malaya (“UM”), who henceforth shall be owner of the copyright in this Work and that any reproduction or use in any form or by any means whatsoever is prohibited without the written consent of UM having been first had and obtained;
- (6) I am fully aware that if in the course of making this Work I have infringed any copyright whether intentionally or otherwise, I may be subject to legal action or any other action as may be determined by UM.

Candidate’s Signature

Date:

Subscribed and solemnly declared before,

Witness’s Signature

Date:

Name:

Designation:

**HEXACYANOFERRATE-BASED NANOCOMPOSITES FOR THE
ELECTROCHEMICAL SENSING OF
HYDROGEN PEROXIDE AND NICOTINE**

ABSTRACT

Metal hexacyanoferrate (MeHCF) is a unique material that not only acquired immense research interest in electrochemical sensing field but also possesses potential as energy storage material. As such, the present thesis sought to investigate the facile method to synthesis MeHCF-based nanocomposites and explore its possible applications. First, comparative research on the synthesis of Prussian blue-polypyrrole (PB-PPy) nanocomposite by novel self-assembly (SA) method and conventional electrodeposition technique was performed. PB-PPy nanocomposites were prepared by the novel self-assembly method and via the electrodeposition approach. The nanocomposites were compared in term of surface morphology and its electrochemical and electrocatalytic characteristics. The results indicated that the SA PB-PPy with 10 deposition cycles demonstrated good sensing behaviour towards hydrogen peroxide (H_2O_2) with a sensitivity of $384.7 \text{ mA M}^{-1} \text{ cm}^{-2}$ whereas capacitive property was observed when the deposition cycles were increased to 20. The SA approach offers easy preparation of electrodes, which allows control of its electrochemical behaviour and sensitivity towards H_2O_2 . The second part of this work emphasised on the facile synthesis of PB analogue: copper hexacyanoferrate (CuHCF) towards nicotine. Reduced graphene oxide (rGO) was used as a substrate to enhance operational stability. The linear range of this fabricated electrochemical sensor was between 0.03 to 5 mM, which is the highest among the reported works, with a compatible sensitivity of $211.5 \text{ mA M}^{-1} \text{ cm}^{-2}$. In addition, this sensor was applied for the detection of nicotine in vape (e-cigarette) sample from the market. For the last section of this work, the capacitive behaviour of SA PB-PPy by 20 deposition cycles was investigated as capacitor material. The areal capacitance of PB-

PPy was at least ten-fold of pristine PB. This revealed PB-PPy can be a promising candidate for energy storage purpose.

Keywords: Metal hexacyanoferrate; nanocomposites; electrochemical sensing; electrochemical capacitor

University of Malaya

**KOMPOSIT NANO BERASASKAN HEKSASIONOFERAT UNTUK
PENDERIA ELEKTROKIMIA HIDROGEN PEROKSIDA DAN NIKOTIN**

ABSTRAK

Logam heksasionoferat (MeHCF) merupakan bahan unik yang bukan sahaja menarik perhatian dalam bidang penyelidikan penderia elektrokimia, malahan ianya adalah bahan yang berpotensi untuk penyimpanan tenaga. Oleh itu, tesis ini adalah untuk menyiasat kaedah mudah untuk sintesis komposit nano berasaskan MeHCF dan meneroka potensi aplikasinya.

Pertama, penyelidikan komparatif terhadap biru Prusia -polipirola (PB-PPy) dengan kaedah pemasangan sendiri (SA) dan teknik elektropemendapan konvensional telah dilakukan. Komposit nano PB-PPy yang disediakan menggunakan kaedah baru dan pendekatan elektropemendapan telah dibandingkan dari segi morfologi permukaan serta sifat elektrokimia dan elektrokatalitiknya. Keputusan menunjukkan SA PB-PPy dengan 10 kitaran pemendapan menunjukkan tingkah laku penderiaan yang baik terhadap hidrogen peroksida (H_2O_2) dengan kepekaan $384.7 \text{ mA M}^{-1} \text{ cm}^{-2}$ manakala sifat kapasitif diperhatikan apabila kitaran pemendapan meningkat kepada 20. Pendekatan ini menawarkan penyediaan elektrod yang mudah dan membolehkan kawalan tingkah laku elektrokimia dan kepekaan terhadap H_2O_2 . Bahagian kedua tesis ini menekankan sintesis mudah untuk analog PB: heksasionoferat tembaga (CuHCF) ke arah pengesanan nikotin. Grafin oksida terturun (rGO) digunakan sebagai substrat untuk meningkatkan kestabilan operasi. Julat linear bagi penderia yang telah dibangunkan ini adalah antara 0.03 dan 5 mM, merupakan yang tertinggi di antara laporan terdahulu, dengan kepekaan sebanding $211.5 \text{ mA M}^{-1} \text{ cm}^{-2}$. Tambahan pula, penderia ini digunakan untuk pengesanan nikotin dalam sampel rokok elektronik (e-rokok). Di samping itu, tingkah laku kapasitif SA PB-PPy tersebut telah disiasat selanjutnya. Dalam sesi terakhir laporan ini, kapasiti PB-PPy

adalah sekurang-kurangnya sepuluh kali ganda dari PB. Keputusan ini mendedahkan PB-PPy sebagai calon yang berpotensi untuk tujuan penyimpanan tenaga.

Kata kunci: Logam heksasionoferat; komposit nano; penderia elektrokimia; bahan penyimpanan tenaga

University of Malaya

ACKNOWLEDGEMENTS

The completion of this research work has been made possible by the support of many, and I am truly thankful to the following people who have played a vital role along this doctoral journey:

First and foremost, my sincere gratitude goes to my supervisor, Dr. Woi Pei Meng. I am inspired by her passion, dedication and success in research. Thank you for your comprehensive advice towards the completion of this work, and for believing in me to achieve more than I myself could imagine. Secondly, I would like to thank Professor Dr. Yatimah Binti Alias. It is such a privilege to work in her prestigious lab.

The completion of this undertaking could not have been possible without the contribution of precious research expertise from Associate Professor Dr. Sharifah Binti Mohamad, Dr. Pooria Moozarm Nia, Dr Teh Swe Jyan, Dr. Farnaz Lorestani, Mahtab Mahdavifar and Dr. Shanaz. I would like to express my gratitude to the devoted staff in the Department of Chemistry, especially En. Shukri, Cik Nani and Miss Kumuthini towards their service and technical support.

To all my friends (Pei Qie, Jee, Yeet Hoong, Dr. Ayesah, Christelle, Valarie, Aqidah, Dr. Vicit, Mastura and Sofia) I have met in Universiti Malaya, thank you for your valuable advice and moral support throughout this journey. Also, I would like to thank my family for moral support. Last but not least, I am grateful for the financial support from Universiti Malaya through grants UMRG Sub-program RP020C- 16SUS by Universiti Malaya and Fundamental Research Grant Scheme (FRGS) FP051-2014A by Ministry of Education Malaysia.

TABLE OF CONTENTS

ABSTRACT	iii
ABSTRAK	v
ACKNOWLEDGEMENTS	vii
TABLE OF CONTENTS	viii
LIST OF FIGURES	xiii
LIST OF TABLES	xviii
LIST OF SYMBOLS AND ABBREVIATIONS	xix
CHAPTER 1: INTRODUCTION	21
1.1 Preface.....	21
1.2 Thesis outline.....	22
1.3 Objectives of the research.....	24
CHAPTER 2: LITERATURE REVIEW	25
2.1 Metal hexacyanoferrate	25
2.2 MeHCF and its nanocomposite	27
2.2.1 Nanocomposite of MeHCF with conducting polymer	27
2.2.2 Nanocomposite of MeHCF with carbon nanomaterial.....	27
2.2.3 Nanocomposite of MeHCF with noble metal.....	28
2.2.4 Ternary MeHCF nanocomposite	28
2.3 Application of MeHCF and its nanocomposite	28
2.3.1 Electrochemical sensor	28
2.3.1.1 Sensitivity.....	31
2.3.1.2 Stability	38
2.3.1.3 Selectivity.....	41

2.3.1.4	Other criteria	42
2.3.2	Energy storage material	42
2.3.2.1	Supercapacitor	43
2.3.2.2	Batteries	45
2.3.3	Dual electrochemical applications	46
2.3.4	Other application	47
2.3.4.1	Cesium decontamination	47
2.3.4.2	Electrochromism	47
2.3.4.3	Photocatalyst	48
2.4	Method development for preparation of MeHCF nanocomposite	48
2.4.1	Electrodeposition	
2.4.1.1	Two-steps electrodeposition	50
2.4.1.2	One-pot electrodeposition	51
2.4.1.3	Sonoelectrodeposition	52
2.4.2	Chemical approach	52
2.4.3	Photochemical synthesis	53
2.4.4	Layer-by-layer assembly	53
2.4.4.1	Combination of electrodeposition and chemical approach	54
CHAPTER 3: METHODOLOGY		56
3.1	Material	56
3.2	Method of preparation for MeHCF-PPy nanocomposite	56
3.2.1	Pre-treatment of glassy carbon electrode	56
3.2.2	Self-assembly MeHCF-PPy nanocomposite	57
3.2.2.1	PB-PPy	57
3.2.2.2	CuHCF-PPy	57
3.2.2.3	PB	58

3.2.2.4	CuHCF	58
3.2.3	Electrosynthesis method of PB-PPy	58
3.2.3.1	Electrochemical experimental set-up	58
3.2.3.2	One-pot pulse electrodeposition of PB-PPy	59
3.3	Characterisation of modified electrode	60
3.3.1	Surface characterisation	60
3.3.1.1	Fourier transform infrared spectroscopy	60
3.3.1.2	Field emission scanning electron microscopy	61
3.3.1.3	Energy dispersion X-ray spectroscopy	61
3.3.2	Electrochemical characterisation	61
3.3.2.1	Cyclic voltammetry	61
3.3.2.2	Electrochemical impedance spectroscopy	62
3.3.2.3	Chronoamperometry	62
3.3.2.4	Galvanostatic charge-discharge test	63
3.3.3	Real-sample analysis	64
3.3.3.1	Pre-treatment of real sample	64
3.3.3.2	High performance liquid chromatography analysis	64
CHAPTER 4: RESULTS AND DISCUSSION		65
4.1	Comparative synthesis methods for the preparation of Prussian blue- polypyrrole nanocomposite	65
4.1.1	Mechanism of formation of PB-PPy	67
4.1.2	Comparison of surface characterisation for PB-PPy film	68
4.1.2.1	Field emission scanning microscopy	68
4.1.2.2	Energy dispersive X-ray spectroscopy	71
4.1.2.3	Fourier transform infrared spectroscopy	72
4.1.3	Electrochemical behaviour of modified electrode	73

4.1.3.1	Cyclic voltammogram	73
4.1.3.2	Surface coverage and estimated thickness of PB-PPy film.....	81
4.1.3.3	Electrochemical impedance spectroscopy	83
4.1.4	Electrochemical sensing of H ₂ O ₂	92
4.1.4.1	Interference study	95
4.1.4.2	Comparison with other work	96
4.2	Self-assembly of PB analogue-CuHCF-PPy nanocomposite as nicotine electrochemical sensor	97
4.2.1	Electrodeposition of rGO as substrate	98
4.2.2	Mechanism of formation of CuHCF-PPy nanocomposite	99
4.2.3	Surface characterisation of CuHCF-PPy film	100
4.2.3.1	Field-emission scanning microscopy	100
4.2.3.2	Energy dispersive X-ray spectroscopy	102
4.2.3.3	Fourier transform infrared spectroscopy	103
4.2.4	Electrochemical behaviour of modified electrode.....	104
4.2.4.1	Cyclic voltammogram	104
4.2.4.2	Electrochemical impedance spectroscopy	106
4.2.5	Electrochemical sensing towards nicotine	109
4.2.6	Application as nicotine sensor	118
4.2.6.1	Interference test, stability and reproducibility.....	119
4.2.6.2	Real sample application	121
4.2.6.3	Comparison with other work	122
CHAPTER 5: CONCLUSION AND RECOMMENDATIONS		124
5.1	Summary	124
5.2	Preliminary result for MeHCF-PPy nanocomposite as potential	

energy storage material.....	126
5.3 Limitation of the study.....	141
REFERENCES.....	142
LIST OF PUBLICATIONS AND PAPERS PRESENTED	159
LIST OF APPENDICES.....	164

University of Malaya

LIST OF FIGURES

Figure 2.1: Schematic diagram of various nanocomposite structure: (i) bi-layered MeHCF-CP/carbon/noble metal; (ii) single layer MeHCF-CP/carbon/noble metal (irregular or regular shape); (iii) MeHCF-CP/carbon/noble metal core-shell structure.....	49
Figure 3.1: Three electrodes electrochemical system.....	58
Figure 4.1: Schematic diagram of the preparation process of PB-PPy film.....	67
Figure 4.2: FESEM images of (A) ED PB-PPy (10), (B) ED PB-PPy (20) and (C) SA PB-PPy (10) and (D) SA PB-PPy (20)	68
Figure 4.3: Particles size distribution of (A) ED PB-PPy (20) and (B) SA PB-PPy (10)	70
Figure 4.4: EDX spectra of (A) ED PB-PPy (10), (B) ED PB-PPy (20), (C) SA PB-PPy (10) and (D) SA PB-PPy (20).	71
Figure 4.5: (A) FTIR spectra of (a) ED PB-PPy (10) and (b) ED PB-PPy (20). (B) FTIR spectra of (a) SA PB-PPy (10) and (b) SA PB-PPy (20).	72
Figure 4.6: Current density response of SA PB-PPy (10) electrode vs. pH.....	73
Figure 4.7: CV of 1 st and 50 th cycles of SA PB-PPy (10) in 0.05 M pH 4.00 citrate buffer with 0.10 M KNO ₃ . The scan rate is 50 mV s ⁻¹	74
Figure 4.8: CV of SA PB-PPy with (a) 10 (b) 20 and (c) 30 NDC. The scan rate is 50 mV s ⁻¹ . The electrolyte used was 0.05 M pH 4.00 citrate buffer with 0.10 M KNO ₃	74
Figure 4.9: CV of (a) SA PB (10) and (b) SA PB (20). The scan rate is 50 mV s ⁻¹ . The electrolyte used was 0.05 M pH 4.00 citrate buffer with 0.10 M KNO ₃	76
Figure 4.10: CV of electrodeposited PB-PPy electrodes with (a) 10 and (b) 20 repetitions. The scan rate is 50 mV s ⁻¹ . The electrolyte used was 0.05 M pH 4.00 citrate buffer with 0.10 M KNO ₃	77
Figure 4.11: (a) CV of SA PB-PPy (10) (b) ED PB-PPy (20) in 0.05 M pH 4.00 citrate buffer with 0.01 M KNO ₃ as supporting electrolyte at applied potential 0.50 to -0.10 V at 50 mV s ⁻¹ scan rate.....	78

Figure 4.12: CV of ED PB-PPy (20) in 0.05 M pH 4.00 citrate buffer with 0.10 M KNO ₃ as supporting electrolyte in different scan rate; (A) 1 (B) 5 (C) 10 (D) 20mV s ⁻¹	79
Figure 4.13: (A) CV of the SA PB-PPy (10) in 0.05 M pH 4.00 citrate buffer with 0.10 M KNO ₃ as supporting electrolyte at various scan rate (from inner to outer curve); 10, 20, 40, 60, 80 and 100 mV s ⁻¹ . (i) Plot of peak current vs. scan rate for SA PB-PPy (10). (B) CV of the ED PB-PPy (20) in 0.05 M pH 4.00 citrate buffer with 0.10 M KNO ₃ as supporting electrolyte at various scan rate: 10, 20, 40, 60, 80 and 100 mV s ⁻¹ . (ii) Plot of peak current vs. scan rate for ED PB-PPy (20).	80
Figure 4.14: Nyquist plot of ED PB-PPy (10), ED PB-PPy (20), SA PB-PPy (10) and SA PB-PPy (20). Inset: Equivalent circuit. The electrolyte used was 0.05 M pH 4.00 citrate buffer with 0.10 M KNO ₃ as supporting electrolyte.	84
Figure 4.15: Evolution of the real part vs. frequency of ED PB-PPy (10), ED PB-PPy (20), SA PB-PPy (10) and SA PB-PPy (20). Electrolyte used was 0.05 M pH 4.00 citrate buffer with 0.10 M KNO ₃ as supporting electrolyte.	85
Figure 4.16: Evolution of imaginary capacitance vs. frequency of ED PB-PPy (10), ED PB-PPy (20), SA PB-PPy (10) and SA PB-PPy (20). Electrolyte used was 0.05 M pH 4.00 citrate buffer with 0.10 M KNO ₃ as supporting electrolyte.	86
Figure 4.17: Bode phase of ED PB-PPy (10), ED PB-PPy (20), SA PB-PPy (10) and SA PB-PPy (20). Electrolyte used is 0.05 M pH 4.00 citrate buffer with 0.10 M KNO ₃ as supporting electrolyte.	88
Figure 4.18: Nyquist plot of SA PB-PPy (30). Inset: Equivalent circuit. Electrolyte used was 0.05 M pH 4.00 citrate buffer with 0.10 M KNO ₃ as supporting electrolyte.	90
Figure 4.19: Bode phase of SA PB-PPy (30). Electrolyte used is 0.05 M pH 4.00 citrate buffer with 0.10 M KNO ₃ as supporting electrolyte.	91
Figure 4.20: CV of (A) ED PB-PPy (20), (B) SA PB-PPy (10) and (C) SA PB-PPy (20) modified electrode in the absence (a) and the presence of 1 mM H ₂ O ₂ (b) in 0.05 M pH 4.00 citrate buffer with 0.10 M KNO ₃ as supporting electrolyte.	92
Figure 4.21: (A) CV of the SA PB-PPy (10) in 0.05 M pH 4.00 citrate buffer with 0.10 M KNO ₃ as supporting electrolyte at various concentration of H ₂ O ₂ (1–8): 0, 0.5, 1, 1.5, 2, 2.5, 3 and 3.5 mM, potential scan rate:	

50 mV s ⁻¹ . (B) The plot of catalytic peak current vs. H ₂ O ₂ concentration.....	94
Figure 4.22: SA PB-PPy (10) electrode response to H ₂ O ₂ (1 mM) and glucose, fructose, ascorbic acid and uric acid as interfering compounds (1 mM) in 0.05 M pH 4 citrate buffer with 0.10 M KNO ₃ as supporting electrolyte Applied potential: 0.10 V vs. (Ag/AgCl)/V.	95
Figure 4.23: rGO/GCE with different deposition cycle (from 1 to 15 cycles) in 5 mM Fe(CN) ₆ ^{3-/4-} with 0.1 M KCl as supporting electrolyte. Scan rate: 50 mV s ⁻¹	98
Figure 4.24: Schematic diagram of the self-assembly process of CuHCF-PPy film.....	100
Figure 4.25: FESEM images of (A) rGO/CuHCF-PPy at low magnification (6,000 x) (i) and (ii) of rGO/CuHCF-PPy, (B) rGO/CuHCF and (C) CuHCF-PPy and (D) CuHCF at high magnification (50,000 x).	101
Figure 4.26: EDX spectrum for (A) CuHCF, (B) rGO/CuHCF and (C) rGO/CuHCF-PPy.	102
Figure 4.27: FTIR spectrum of (a) GO, (b) rGO/ CuHCF and (c) rGO/CuHCF-PPy and (d) CuHCF-PPy. Insets: Magnification of GO spectrum.	104
Figure 4.28: CV of (a) CuHCF and (b) CuHCF-PPy (c) rGO/CuHCF, (d) rGO/CuHCF-PPy. The scan rate is 50 mV s ⁻¹ . The electrolyte used was 0.1 M KCl.	105
Figure 4.29: CV of (i) Bare GCE and (ii) rGO. The scan rate is 50 mV s ⁻¹ . The electrolyte used was 0.1 M KCl.	106
Figure 4.30: Nyquist plot (a) rGO, (b) rGO/CuHCF, (c) rGO/CuHCF-PPy, (d) CuHCF (20). Inset: Equivalent circuit (i) for rGO, CuHCF, CuHCF-PPy and (ii) rGO/CuHCF and rGO/CuHCF-PPy. Electrolyte used is 0.1 M KCl solution containing 5 mM Fe(CN) ₆ ^{3-/4-} (1:1).	107
Figure 4.31: Bode phase of (a) rGO/CuHCF and (b) rGO/CuHCF-PPy.	108
Figure 4.32: CV of (a) GCE and (b) rGO in the absence (solid) and presence (dotted line) of 1 mM nicotine; c) rGO/CuHCF-PPy in the absence (solid) and presence (dotted line) of 1 to 3 mM nicotine with 0.1 M KCl as supporting electrolyte.	110
Figure 4.33: Mechanism of nicotine oxidation.	111

Figure 4.34: Oxidation current response of 1 mM nicotine vs. applied potential.....	112
Figure 4.35: Amperometric curve of rGO/CuHCF-PPy with 5 to 15 NDC towards 1 mM to 5 mM nicotine.	113
Figure 4.36: Amperometric testing curve of various modified electrodes: (a) CuHCF, (b) CuHCF-PPy, (c) rGO/CuHCF and (d) rGO/CuHCF-PPy; Insets: Amperometric curve of PPy towards 1-5 mM nicotine.	115
Figure 4.37: (A) Plot I_{pa} vs. scan rate and (B) Plot of E_{pa} vs. $\log v$	116
Figure 4.38: Amperometric response of rGO/CuHCF-PPy electrode upon successive addition of nicotine from 0.2 to 5 mM. Operating potential: +0.85 V. Insets: Calibration curve.	118
Figure 4.39: Amperometric current response of CuHCF-PPy to the addition of 0.5 mM nicotine (NIC), 1 mM glycerin, propylene glycol (PG), fructose, glucose, sucrose, uric acid (UA), H_2O_2 , 1 mM nicotine (NIC) and 2 mM nicotine (NIC) at operating potential +0.85 V.	119
Figure 4.40: Stability of modified electrode in three weeks.	120
Figure 4.41: (A) HPLC response of standard nicotine solution from 0 to 20 mM. (B) HPLC response of e-cigarettes (vape) solution.	121
Figure 4.42: HPLC calibration curve for nicotine standard solution.	122
Figure 5.1: FESEM images of (A) PB and (B) PB-PPy in 50,000 x magnification. ...	128
Figure 5.2 : FT-IR spectrum of (A) PB and (B) PB-PPy on glassy carbon electrode.	128
Figure 5.3 : Cyclic voltammograms of PB-PPy and PB in 1.0 M KNO_3 as electrolyte. Insets: CV of PPy. The potential range was from -0.2 V to 1.2 V with scan rate 50 mV s^{-1}	130
Figure 5.4: Log (i)- log (v) (A) PB and (B) PB-PPy. Determination of b-value from the peak anodic and cathodic current.	133
Figure 5.5: Galvanostatic charge/discharge curve (GDC) of (A) PB-PPy at current density (a) 0.2, (b) 0.5, (c) and (d) 2 mA cm^{-2} ; (B) comparison of (a) PB and (b) PB-PPy at 0.2 mA cm^{-2} in 1.0 M KNO_3	136

Figure 5.6: Normalised specific capacitances derived from galvanostatic charge/discharge at high current density 2 mA cm^{-2} in 1 M KNO_3 . Inset: Charge/discharge plot at 1, 100 and 200 cycles, respectively..... 137

Figure 5.7: (A) Nyquist plot of bare GCE, PB and PB-PPy. Inset: Magnification of Nyquist plot of PB-PPy. (B) Bode plot of PB and PB-PPy (C) Equivalent circuit for (i) bare GCE, (ii) PB and (iii) PB-PPy-modified electrode..... 140

University of Malaya

LIST OF TABLES

Table 2.1: MeHCF-based nanocomposites modified electrode and its sensing performance (effect of conductivity).....	32
Table 2.2: MeHCF-based nanocomposites modified electrode and its sensing performance (effect of nanoparticles).....	35
Table 2.3: MeHCF-based nanocomposites modified electrode and its sensing performance (effect of morphology).	37
Table 2.4: MeHCF-based nanocomposites modified electrode and its sensing performance (effect of hydrophilicity).	38
Table 2.5: MeHCF-based nanocomposites modified electrode and its affect to stability.	40
Table 2.6: MeHCF-based nanocomposites modified electrode and its effect towards selectivity.....	41
Table 2.7: MeHCF-based nanocomposite as supercapacitors.....	45
Table 4.1: The surface coverage and thickness of PB-PPy calculated.	82
Table 4.2: Electrochemical parameters obtained by fitting of EIS results.....	87
Table 4.3: Electrochemical parameters of SA PB-PPy (30) obtained by fitting of EIS results.....	91
Table 4.4: Comparison of several PB based H ₂ O ₂ electrochemical sensors.....	96
Table 4.5: Peak-to-peak separation (ΔE_p) of [Fe(CN) ₆] ^{3-/4-} for different layers of rGO.	99
Table 4.6: Electrochemical parameters obtained by fitting EIS results.	109
Table 4.7: Comparison of nicotine amperometric sensors.....	123
Table 4.8: The recovery of nicotine spiked in vape product (0 mg mL ⁻¹ nicotine) and detection of nicotine in vape sample (that containing nicotine).	122
Table 5.1: Areal capacitance of PB and PB-PPy calculated from GDC.....	135
Table 5.2: EIS parameters acquired by equivalent fitting.....	139

LIST OF SYMBOLS AND ABBREVIATIONS

Ag	:	Silver
Au	:	Gold
BG	:	Berlin green
<i>c.a</i>	:	<i>Circa</i>
CNT	:	Carbon nanotube
CoHCF	:	Cobalt hexacyanoferrate
CP	:	Conducting polymer
CuHCF	:	Copper hexacyanoferrate
CV	:	Cyclic voltammogram
DI	:	Deionised
ED	:	Electrodeposition
EDX	:	Energy dispersive X-ray spectroscopy
EIS	:	Electrochemical impedance spectroscopy
FESEM	:	Field emission scanning microscope
FTIR	:	Fourier transform infrared spectroscopy
GCD	:	Galvanostatic charge-discharge
GO	:	Graphene oxide
GQD	:	Graphene quantum dot
H ₂ O ₂	;	Hydrogen peroxide
HPLC	:	High performance liquid chromatography
LBL	:	Layer-by-layer
LoD	:	Limits of detection
LoQ	:	Limit of quantification
MeHCF	:	Metal hexacyanoferrate

MWCNT	:	Multi-walled carbon nanotube
NDC	:	Number deposition cycles
NIC	:	Nicotine
NiHCF	:	Nickel hexacyanoferrate
NP	:	Nanoparticles
PANI	:	Polyaniline
PB	:	Prussian blue
Pd	:	Palladium
PEDOT	:	Poly (3,4-ethylenedioxythiophene)
PG	:	Propylene glycol
PMPD	:	Poly (m-phenylenediamine)
PPy	:	Polypyrrole
PVP	:	Polyvinylpyrrolidone
PW	:	Prussian white
rGO	:	Reduced graphene oxide
RSD	:	Relative standard deviation
SA	:	Self-assembly
SCE	:	Saturated calomel electrode
SHE	:	Standard hydrogen electrode
SWCNT	:	Single-walled carbon nanotube
UA	:	Uric acid
V	:	Voltage

CHAPTER 1: INTRODUCTION

1.1 Preface

Transition metal hexacyanoferrate (MeHCF) denotes a vital class of synthetic coordination compounds, of which Prussian blue (PB) represents the classical prototype (Griffith, 1962). These group of compounds, including other structures analogues, have gained research interest, particularly in electrochemical sensing owing to their excellent electrocatalytic and electrochemical behaviour (Kong, Selomulya, Zheng, & Zhao, 2015).

To enhance the performance of pristine MeHCF component and to create novel properties, intense research works have been carried out to synthesis MeHCF-based nanocomposites. Nanocomposites are of special significance due to their distinctive characteristics are not solely come from the intrinsic properties but also from the synergistic effect of each component (Kao, Thorkelsson, Bai, Rancatore, & Xu, 2013). Hence, researchers are devoted to developing a new or improved fabrication method to engineer the MeHCF based nanocomposites in recent years. In general, materials that have been employed to form nanocomposite with MeHCF including conducting polymer (CP), carbon nanomaterials and noble metals.

In this work, hydrogen peroxide (H_2O_2) is first selected as the analyte of interest as it is one of the most common electroactive analytes which has been used to verify the electrochemical sensing performance of the modified electrodes. Moreover, H_2O_2 is a catalytic sub-product of various enzymes and extensively used in the chemical and food industries (W. Chen, Cai, Ren, Wen, & Zhao, 2012). The next investigated analyte in this work is nicotine. The sensing of nicotine is significant for medicine, toxicology and the tobacco industry. The detection of nicotine is a crucial analysis in the tobacco industry as the quality of cigarette products can be determined by its level of nicotine (Zuo et al., 2004). Nicotine can bring potential health problem, especially cardiovascular and

respiratory-related condition which is associated with lung cancer (Hall et al., 2014). Besides that, studies have been performed to understand its potential medical value towards diseases such as Alzheimer's (Winzer-Serhan, 2017) and Parkinson's disease (Quik, O'Leary, & Tanner, 2008).

In this present research, a facile technique to synthesise MeHCF-PPy nanocomposites is expected to be established in this study. Firstly, a comparative study on synthesis method of selected MeHCF-CP nanocomposite by a novel self-assembly approach and conventional electrochemical approach was conducted. Polypyrrole (PPy) is an appropriate CP to form nanocomposite with selected MeHCF as it can be easily oxidised by the precursor of MeHCF to form MeHCF-PPy nanocomposite film effortlessly. These fabricated MeHCF-CP nanocomposites were modified for electrochemical sensing of H_2O_2 and nicotine, respectively. It is worth to mention that reduced graphene oxide was used as a basal substrate for the sensing of nicotine to provide mechanical support of the active molecules as well as increasing the operational stability. In addition, it was found that the developed facile self-assembly technique allows the control of electrochemical behaviour, by behaving as an electrochemical sensor to an electrochemical capacitor material. Thus, the intercalation pseudocapacitive behaviour which exhibited by the as synthesised nanocomposites was discussed in the later part of this report.

1.2 Thesis outline

The work demonstrated in this thesis addresses the promising application of the facile synthesised MeHCF-PPy nanocomposites towards electrochemical sensors for hydrogen peroxide and nicotine. In addition, MeHCF-based nanocomposites as potential supercapacitive material for energy storage purpose was discussed.

Chapter 1 presents the general introduction on research background regarding metal hexacyanoferrate, conducting polymer, nanocomposites and their applications in

electrochemical sensors and materials for energy storage purpose, together with the scope and objectives of this thesis.

Chapter 2 describes the literature review on materials of interest- Metal hexacyanoferrates, MeHCF-based nanocomposites, its applications as electrochemical sensors, energy storage materials (batteries and supercapacitors) and other applications of MeHCF and its nanocomposites, as well as methods development for synthesising MeHCF-based nanocomposite.

Chapter 3 shows the chemicals, materials and techniques used to modify the surface of the electrode and the characterisation of the fabricated nanocomposites.

Chapter 4 presents the study of comparative synthesis method of self-assembly and one-pot pulse electrodeposition technique of PB-PPy nanocomposite. The optimisation and the sensing application toward H_2O_2 detection were demonstrated in this chapter (This work has been published in *Electrochimica Acta*, June 2017, Issues 246, pp. 841-852). Secondly, the alteration of PB composition in the nanocomposite to its analogues, copper hexacyanoferrate, and optimisation of the electrode as the electrochemical sensor for nicotine detection was discussed (This work has been published in *Journal of Electroanalytical Chemistry*, Feb 2019, Issue 246 pp. 67-75). Thirdly, the interesting intercalation pseudocapacitive behaviour of PB-PPy nanocomposite was illustrated in this section (This work has been published in *Journal of Applied Electrochemistry*, June 2019, Volume 49, Issue 6, pp. 631–638).

Chapter 5 draws the thesis summary and preliminary result of future works.

1.3 Objectives of the research

- i. To develop a facile procedure based on MeHCF nanocomposite for electrode modification.
- ii. To compare the developed of electrode modification with the conventional method.
- iii. To demonstrate the synthesised nanocomposite as the electrochemical sensor.

University of Malaya

CHAPTER 2: LITERATURE REVIEW

This chapter describes the introduction metal hexacyanoferrates (MeHCF) and its nanocomposite. The materials employed to form nanocomposites with MeHCF, particularly conducting polymers (CP), carbon nanomaterials, noble metals, as well as ternary nanocomposites were highlighted. Besides that, the advantages of forming MeHCF-based nanocomposite in electrochemical applications, especially as electrochemical sensors and energy storage materials were explained. In addition, the chapter explained other applications of MeHCF-based nanocomposites and synthesis approach to form MeHCF-based nanocomposites.

2.1 Metal hexacyanoferrate

Transition metal hexacyanoferrates (MeHCF) is an important group of mixed-valence compounds with the general formula of $A_hM_k[Fe(CN)_6]_{l.m}H_2O$ (h, k, l, m= stoichiometric number, M= transition metal ion). The unit cell length is 10.2 Å. MeHCF have a face-centred cubic framework with octahedral coordination of the M and Fe ions links by $N\equiv C$ and $C\equiv N$ ligands, respectively (Ferlay, Mallah, Ouahès, Veillet, & Verdaguer, 1995). The alkali metal cations, A are situated in the tetrahedral position which responsible for charge compensation. In some circumstances, coordinated water molecules and anions could present in this assembly.

Prussian blue (PB) is considered as the oldest synthetic coordination compound and has a long history. PB was first synthesised by artist Diesbach in 1704 in Berlin by coincidence (Kraft, 2008). Nonetheless, the novel research of PB on its electrochemical behaviours was only revealed in 1978. Subsequently, abundant studies were carried out on its electrochemical, electrochromic, magnetic, electro and photo-catalytic behaviours. Owing to their excellent electrochemical and photochemical behaviours, PB has been used for various applications. For instance, as electrochemical sensors, self-rechargeable

batteries, supercapacitors, electrochromic displays, fuel cells, sodium and potassium ion batteries, and signal-enhancing nanodevices.

The assembly of PB is a three-dimensional (3D) network comprising of alternating ferrous and ferric ions on cubic framework position in each framework of PB, ferric ferrocyanide with an iron(III) atom is linked to nitrogen atom and iron(II) atom is linked to the carbon atom, which permitting for high-spin and low-spin electron alignment, respectively (Kong et al., 2014; Pasta et al., 2014). Also, the counter-cations and other small molecules can intercalate in the interstitial site and vacancies of PB.

A distinctive cyclic voltammogram (CV) of PB interfaces comprises of two sets of peaks, results from two reversible reduction/oxidation reactions: (i) the conversion of PB into its reduced form, Prussian white (PW); (ii) the oxidation of PB to a mixture of Prussian yellow (PY) and Berlin green (BG). This is due to a combination of BG and PY is often formed instead of pure BG (Itaya, Ataka, & Toshima, 1982).

The redox couple at a more negative potential (0.2 V vs. Ag/AgCl) resembles to the redox of high-spin system (Prussian blue/Berlin green, $\text{Fe}^{3+}/\text{Fe}^{2+}$), whereas the other peaks at a more positive potential (1.0 V vs. Ag/AgCl) are due to redox reaction of low spin $\text{Fe}(\text{CN})_6^{3-/4-}$ (Prussian blue-Berlin green).

2.2 MeHCF and its nanocomposite

In the field of material science, an interesting research topic relies on the synthesis of composite material. Composites not only possess the excellent characteristics of the individual material but the synergistic materials demonstrated the fine qualities of both organic and inorganic individual based materials (Kao et al., 2013). This will enhance the performance of MeHCF, or even creates multifunctional materials with novel outstanding behaviour if the combination is in the nanometre scale. Typically, the materials employed to form nanocomposites with MeHCF are elaborated as follow:

2.2.1 Nanocomposite of MeHCF with conducting polymer

It is common that conducting polymer (CP) arises as a natural component to form a composite or hybrid material, owing to its excellent physical, chemical properties and simple synthesis. Moreover, CP has the advantages of high conductivity, high charge storage ability, facile preparation and cheap in costing.

CP is a polymer with the p-conjugated chain backbone structure, consisting of a series of alternating single and double bonds (Balint, Cassidy, & Cartmell, 2014). This characteristic attributed to delocalisation of p-electrons along the whole polymer chain, resulting in their unique conducting properties (Y. W. Park, 2010). The common CP used to form nanocomposites with MeHCF in the field includes polypyrrole (PPy), polyaniline (PANI) and poly (3,4-ethylenedioxythiophene) (PEDOT).

2.2.2 Nanocomposite of MeHCF with carbon nanomaterial

Carbon nanomaterials which were employed to form nanocomposites with MeHCF are generally including carbon nanotube (CNT), graphene, reduced graphene oxide (rGO) and graphene quantum dot (GQD). CNT is further categorised into multiwalled CNT (MWCNT) and single-walled CNT (SWCNT). All these carbon nanomaterials possess high conductivity and are able to facilitate the electron transfer of PB, as well as employed

as a support layer for the deposition of MeHCF (Borisova, Karyakina, Costlier, & Karyakin, 2009).

2.2.3 Nanocomposite of MeHCF with noble metal

Noble metals such as gold (Au), platinum and silver (Ag) were extensively used to form nanocomposite with MeHCF due to the distinctive features of noble metal. It is well known that noble metal nanoparticles can enhance the conductivity and the electron transfer rate of the MeHCF. Noble metals also act as a catalyst for the growth of MeHCF.

2.2.4 Ternary MeHCF nanocomposite

Researches were dedicated to design ternary nanocomposites as it offers insight of creating novel composites besides the fascinating synergistic augmentation of three components in the ternary nanocomposites (Pan, Gu, & Dong, 2016).

2.3 Application of MeHCF and its nanocomposite

2.3.1 Electrochemical sensor

An electrochemical sensor converts the interaction of analyte between the analyte and electrode into a viable electrochemical signal. Electrochemical sensing is a relatively significant field in analytical chemistry and is employed to detect countless analytes. Electrochemical sensors are especially remarkably useful for electro-active compounds detection due to its inherent nature to the analytes (Leake, 2006), thus it can offer a simple, rapid, sensitive and cost-effective detection and most importantly, enable real-time detection (J.Wang, 2006b).

Prussian blue (PB) and its analogues such as nickel hexacyanoferrate (NiHCF) and copper hexacyanoferrate (CuHCF) (Oliveira et al, 2018) have been studied extensively for the development of electrochemical sensor due to its outstanding electrochemical and electrocatalytic behaviour. MeHCF is most renowned as hydrogen peroxide (H₂O₂)

sensor where PB is described as an artificial peroxidase that corresponds to the biological family of peroxidase enzyme for H_2O_2 (Karyakin, 2001; Karyakin, Karyakina, & Gorton, 2000). MeHCF has also been reported as a sensor for other analytes such as nicotine (C. Y. Yang, Chang, Chen, & Devadas, 2016), L-cysteine (N. Song, Zhu, Ma, Wang, & Lu, 2018) and hydrazine (C. Wang et al., 2010) at respective potential and can even serve as a biosensor, provided the enzyme or antibody cast on top of the MeHCF modified electrode (Karyakin, Gitelmacher, & Karyakina, 1994; X. Z. Zhang, Zhou, Zhang, Zhang, & Gu, 2016).

Hydrogen peroxide (H_2O_2) is a simple yet very vital molecule. H_2O_2 is a catalytic by-product of numerous oxidases including, glucose oxidase, cholesterol oxidase and a substrate for the horseradish peroxidase enzyme. It is also widely used in the chemical and food industries (Tsiafoulis, Trikalitis, & Prodromidis, 2005). H_2O_2 was chosen as one of the analytes of interest in this research due to its importance and the most common analyte for non-enzymatic electrochemical sensors. Hence, it is usual for a novel modified electrode to employ H_2O_2 as their respective analyte to verify the electrochemical sensing performance of the electrode.

Nicotine is a significant analyte of interest in the tobacco industry, medical and toxicology field. Firstly, regulation of nicotine content is important in tobacco industry (cigarettes and e-cigarettes) for consumers' safety (Lisko et al., 2015). Furthermore, nicotine is carcinogenic and able to increase the blood pressure, hence can bring some potential health problems, especially cardiovascular and respiratory-related condition like lung cancer (Smits, Temme, & Thien, 1993). Besides that, studies have been performed to understand its medical value towards diseases such as Alzheimer's (Winzer-Serhan, 2017) and Parkinson's disease (Quik et al., 2008). Up until today, there are still a quite a limited number of reports on nicotine detection especially using electrochemical sensor

and no specific material yet to be used in its electrochemical sensing. Nonetheless, a composite of palladium hexacyanoferrate with graphene oxide was reported as the highly sensitive amperometric nicotine sensor (G. Yang, Chang, Chen, & Devadas, 2016). This study indicated that MeHCF might be able to employ as the electrode for nicotine sensing.

Other analytes such as L-cysteine is vital in the physiologic and clinical analysis as it is the indicator for hepatic cystinuria and used in the treatment of alopecia (Clemente, Reig García-Galbis, & Martínez-Espinosa, 2018; Sumorok & Goldfarb, 2013). Previous report also employed PB-graphite quantum dots modified graphite felt to detect L-cysteine (L. Wang et al., 2016). Hydrazine which is a carcinogenic and hepatotoxic chemical, as well as possessing varied functions in industry and agriculture (Reilly & Aust, 1997). It has been detected using PB/carbon nanopolyhedra/PPy composite (J. Zhao et al., 2017).

Nonetheless, MeHCF materials typically demonstrated low conductivity (Z. Wang et al., 2014) and poor stability (R. Z. Zhang et al., 2015), especially in a neutral or alkaline solution. The OH^- ions which were produced from the electrochemical reduction of H_2O_2 can easily react with Fe^{3+} to form $\text{Fe}(\text{OH})_3$, which leads to Me-CN-Fe bond cleavage in MeHCF film (Karyakin, Karyakina, & Gorton, 1999). Using the study of H_2O_2 electrochemical sensor as an example, pristine MeHCF (PB, CuHCF and NiHCF) exhibited a sensitivity range from 0.14 to 188 $\text{mA M}^{-1} \text{cm}^{-2}$ (Fiorito, Brett, & Córdoba De Torresi, 2006; Karyakin et al., 2004), while the MeHCF (PB) in nanoscale may only demonstrate sensitivity up to 200 $\text{mA M}^{-1} \text{cm}^2$ towards the detection of H_2O_2 (Puganova & Karyakin, 2005). Therefore, the improvement of these MeHCF based electrochemical sensors is the focus of the current research.

One of the strategies to enhance the electrochemical sensing performance is by forming nanocomposite with other conducting materials to utilise the synergistic effect

between the binary components. Additionally, the forming of MeHCF nanocomposites is expected to improve their sensing performance in terms of sensitivity, stability as well as selectivity, which are the important criteria in the electrochemical sensor.

2.3.1.1 Sensitivity

Sensitivity is defined as the slope of the calibration curve, and the calibration curve is plotted as a steady-state response against analytes concentration (Thévenot, Toth, Durst, & Wilson, 2001). The sensitivity can be enhanced by the following factors:

(a) Conductivity

Conducting materials such as CP, carbon nanomaterials and noble metal increase the electronic conductivity and facilitate the electron transfer between MeHCF and the electrode, thus consequently contributes to the degree of sensitivity of synthesised nanocomposites towards electrochemical sensing of analytes. For instance, CuHCF-PPy demonstrated a sensitivity of $726 \text{ mA M}^{-1} \text{ cm}^{-2}$ towards H_2O_2 sensing, which was 5000 times higher than pristine CuHCF ($0.14 \text{ mA M}^{-1} \text{ cm}^{-2}$) due to the conductivity possessed by PPy which works as a molecular wire connecting the CuHCF catalytic site (Fiorito et al., 2006).

According to **Table 2.1**, the performance of ternary nanocomposites sensors often has a higher sensitivity if compared to pristine MeHCF or nanocomposites which formed from two conductive components. A ternary PB/PANI/MWCNT nanocomposite exhibited the higher sensitivity as compared to PB/PANI electrode based sensor towards H_2O_2 sensing (Z. Wang et al., 2012). The outstanding sensitivity can be attributed to synergistic effects from three components, which two of them were the highly conducting PANI and CNT. Although the CP used in the reported work is different, the sensitivity of NiHCF/PANI/CNT electrode exhibited far higher sensitivity than NiHCF/PPy.

Table 2.1: MeHCF-based nanocomposite modified electrode and its sensing performance (effect of conductivity)

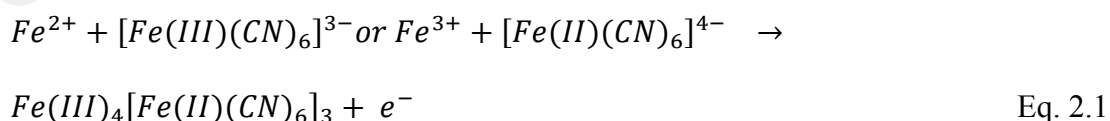
Target analyte	Type of electrode	Linear range	Sensitivity (mA M ⁻¹ cm ⁻²)	Detection limit (μM)	Ref.
H ₂ O ₂	CuHCF-PPy	Up to 0.5 mM	726	13	Fiorito et al. (2006)
	NiHCF/PANI/CNT	1 μM-3 mM	2288	12.4	Z. Wang et al. (2012)
	NiHCF/PPy	0.1 mM-0.9 mM	88.33	1	Fiorito et al. (2006)
	PB/PANI/MWCNT	8 nM-2 μM	526.43	0.005	Zou, Sun, & Xu, (2007b)
	PANI/PB/CNT	80 nM-5 mM	508.18	0.01	Zou, Sun, & Xu, (2007a)
	PANI-PB	10 μM-0.5 mM	485	NA	Amarnath & Sawant, (2019)

NA= not applicable

(b) MeHCF nanoparticle

Recent studies demonstrated that monomers, carbon nanomaterials and noble metal can work as reducing agents in the formation of MeHCF nanoparticles. Nanoparticles provide more surface area for analyte and hence increase the sensitivity.

Using the first discovered MeHCF-PB as an example, PB was conventionally synthesised via two different chemical routes (Ding, Hu, Gu, & Xia, 2009) as shown in Eq. 2.1.



These reducing agents elongate the reaction of the synthesis mechanism and make it easier to control the size of the PB nanoparticles formed (Qiu, Peng, Liang, Li, & Xia, 2007) as shown in Eq. 2.2 and Eq. 2.3. With the aid of additional reducing agents, Fe³⁺

will reduce to Fe^{2+} and subsequently these Fe^{2+} ions will react with $Fe(CN)_6^{3-}$ to form PB.



E. Jin, Bian, Lu, & Wang (2012) synthesised MWCNT/PPy/PB nanocomposites via direct mixing of Fe^{3+} and $[Fe(CN)_6]^{3-}$ in the presence PPy-MWCNT as a reducing agent. The PB nanoparticles with size between 12-24 nm were successfully formed on top of PPy-MWCNT. In the report, PPy was used to reduce Fe^{3+} to Fe^{2+} and then Fe^{2+} was reacted with $[Fe(CN)_6]^{3-}$ to form PB nanoparticle. The sensitivity of this sensor towards the detection of H_2O_2 was recorded as $345 \text{ mA M}^{-1} \text{ cm}^{-2}$. Similar to PPy, ethylenedioxythiophene (EDOT) can act as reductant for $Fe^{(III)}-Fe^{(III)}(CN)_6^{3-}$ complex (PB precursor) to form PB nanoparticles (Yang et al., 2017). As a result, PB-PEDOT core-shell structure was formed with an average diameter of about 52.6-16.7 nM. The morphology showed a 3D hierarchical porous structure.

Also, PB analogues can be formed by the same means of redox synthesis with CP. This is due to monomers such as pyrrole that could be easily oxidised by a variety of transition metals which forms metallic salt, for instance, $FeCl_3$, $Fe(NO_3)_3$, to $K_3[Fe(CN)_6]$ and $CuCl_2$ (Prasanth, Shankar, Gupta, Rana, & Ahn, 2015). All of which are regular oxidants for the synthesis of conducting PPy. Wong, Zhang, Yang, Chen, & Ying (2015) have reported the formation of lithium hexacyanoferrate-CP hybrid using $Li_3Fe(III)(CN)_6$ as the PB precursor and pyrrole as the reducing agent. Also, a cylinder-like PPy was observed when $K_3[Fe(CN)_6]$ was used as the oxidant in the polymerisation reaction of pyrrole (Tuo et al., 2016). Hence, the PB analogues such as CuHCF, NiHCF and CoHCF can be prepared by two suggested routes as follows: (i) by adding respective metal salt to

the PPy doped- $[\text{Fe}(\text{CN})_3]^{4-}$ complex or (ii) the redox process between pyrrole and Me^{n+} - $\text{Fe}^{(\text{III})}(\text{CN})_6^{3-}$ complex.

Besides that, carbon nanomaterials such as MWCNT was mixed with the PB precursors to form PB-MWCNT hybrid (J. Zhai, Zhai, Wen, & Dong, 2009). The formation of PB can be attributed to the lower Fermi level of MWCNT if compared to the redox potential of $\text{Fe}^{3+}/\text{Fe}^{2+}$. MWCNT is *ca* +0.5 V (vs. SHE) whereas the redox potential of $\text{Fe}^{3+}/\text{Fe}^{2+}$ is *ca* +0.783 V (vs. SHE). Hence, it is predicted that MWCNT can reduce Fe^{3+} to Fe^{2+} as a result of relative potential levels, followed by a spontaneous reaction of Fe^{2+} with $\text{Fe}(\text{CN})_6^{3-}$ to yield PB. The size of randomly deposited PB nanoparticles on MWCNT surfaces was around 40 nm with a narrow size distribution. Another mechanism route was also proposed in the formation of PB-SWCNT nanocomposites. The $\text{Fe}^{(\text{III})}$ - $\text{Fe}^{(\text{III})}(\text{CN})_6^{3-}$ complex has the redox potential of +1.20 V vs. SHE whereas SWCNT also has the similar Fermi level with MWCNT and hence the electrons transfer occurred from SWCNT to $\text{Fe}^{(\text{III})}$ - $\text{Fe}^{(\text{III})}(\text{CN})_6^{3-}$ (Choi et al., 2002). The size of PB nanoparticles formed with this mechanism was reported as 30 nm on top of SWCNT (W. Zhang, Wang, Zhang, Wang, & Fang, 2009).

Other examples of MeHCF-carbon nanocomposite included graphene quantum dots (GQD) (L. Wang et al., 2016), graphene (E. Jin, Lu, Cui, Chao, & Wang, 2010) and PB nanocubes on rGO (Cao, Liu, Zhang, & Lu, 2010), GO sheet-PB nanocomposites (X. W. Liu, Yao, Wang, & Wei, 2010). These nanocomposites were employed as hydrogen peroxide and hydrazine sensors. Unlike conducting polymer, PB analogues-carbon nanocomposites were unable to synthesise using this redox approach. This is presumably owing to the less oxidising strength of these MeHCF precursor salts. Hence, the formation of PB analogues such as yttrium hexacyanoferrate (YHCF) or cobalt hexacyanoferrate (CoHCF) on top of carbon layer is usually performed under electrodeposition technique

(Devadas, Yeh, Chen, & Piraman, 2014) or in situ chemical precipitation onto the carbon layer (Deng, Li, Qiu, Zhou, & Hou, 2015).

Furthermore, noble metal was able to effectively induce the formation of MeHCF nanoparticles similar to carbon nanomaterials or CP (Ni et al., 2013). The noble metal is able to catalytically reduce Fe^{3+} to Fe^{2+} and hence drives the formation of PB nanoparticles. Ni and co-workers (2013) electrodeposited Au nanoparticles (AuNPs) on GCE to catalyse the chemical deposition of PB to form PB@Au nanocomposite. Similar to that, J. Zhao and co-workers (2015) have electrodeposited Ag nanoparticles on graphite felt and PBNP (30-40 nm) was catalytically formed on the AgNP surface from an aqueous solution of $\text{K}_3[\text{Fe}(\text{CN})_6]$, FeCl_3 , KCl and HCl. Also, PBNPs formed around 30 to 60 nm with AuNP acted as the reducing agent for PB precursor as reported in the study of Qiu and co-workers (2007).

Table 2.2: MeHCF-based nanocomposite modified electrode and its sensing performance (effect of nanoparticles).

Target analyte	Type of electrode	Linear range	Sensitivity ($\text{mA M}^{-1} \text{cm}^{-2}$)	Detection limit (μM)	Ref.
H_2O_2	MWCNT/PPy/PB	4 nM-0.517 nM	345	0.08	E. Jin et al. (2012)
	PB/MWCNT hybrid	0.01-0.04 mM	1.54	0.567	J. Zhai et al. (2009)
	Nafion®/PB/graphene nanosheet	0.02-0.2 mM	196.6	1.9	E. Jin et al. (2010)
	PB-rGO	0.05 μM -0.12 mM	-	0.045	Cao et al. (2010)
	GO sheet-PB nanocomposites	0.05-140 mM	NA	NA	X. W. Liu et al. (2010)
	PB/AuNPs	2 μM -8.56 mM	562	0.1	Ni et al., (2013)

	PB/SWCNT	0.5-27.5 mM	NA	0.001	W.Zhang et al., (2009)
Hydrazine	PB@Ag	NA	26.06 (A M ⁻¹)	0.049	J. Zhao et al. (2015)
L-cysteine	PPy/GQD@PB/GF	0.2-50 μM; 50 μM-1 mM	0.41;0.15	0.15	L. Wang et al. (2016)

*NA= not applicable

(c) Special morphology

The controlled formations of unique structures such as nanotubes, nanofibers or hollow structures are very vital in material science, as it is important to provide a higher specific surface area and hence increase the sensitivity of the sensors.

Inspired by the facile redox reaction of PB precursors and pyrrole, PPy has been employed as a template to form various morphologies of PB-PPy nanocomposites. Owing to the shape of PPy, it can be tailored by using certain chemicals such as dye molecules methyl orange (MO) and ferric salt. Yang, Zheng, & Zheng (2016) reported an encapsulation of PB into hollow PPy, using Fe₃O₄ spheres as a template and the Fe³⁺ source for the formation of PB. Core-shell Fe₃O₄@PPy was formed by chemical polymerisation of pyrrole with FeCl₃ in the presence of sodium dodecyl sulfate. The PB nanocubes were subsequently formed on the surface of hollow PPy via the reaction between K₄[Fe(CN)₆] solution and Fe³⁺ was released from Fe₃O₄ in the acidic environment. This PB-H-PPy nanocomposite can reduce the diffusion resistance of analyte as well by offering a large surface area for H₂O₂ molecules adsorption and reaction due to its hollow structure. As a result, a H₂O₂ sensor with a comparable lower LoD of 1.6 μM and relatively high sensitivity of 484.4 mA M⁻¹ cm⁻² for a linear range between 5 μM to 2.775 mM was fabricated. Moreover, a three-dimensional (3D) PB-PPy aerogel was fabricated by Tuo and co-workers (2016), with the characteristics of high

porosity and large specific surface area, which are able to improve the contacts between electroactive materials in the aerogels modified electrodes and electrolytes. This PB-PPy aerogel was produced via freeze-drying of the self-standing PPy doped $\text{Fe}(\text{CN})_6^{3-}$ hydrogel when formed via MO and $\text{K}_3[\text{Fe}(\text{CN})_6]$ as template and oxidants. PB was formed on the aerogel surface by reacting with FeCl_3 . Hence, the PB-PPy aerogel demonstrated as a promising electrocatalyst towards the reduction of H_2O_2 .

For the cases of template-assisted synthesis between MeHCF-carbon materials, nanocomposites following the original shape of the carbon materials such as carbon nanofiber (CNF) can be formed. However, the shape of the carbon material cannot be tailored to spheres or other morphology like CP because of its inherent morphology. L. Wang and co-workers (2012) produced PB on COOH-functionalised CNF by similar redox reaction. A nanofiber with PB coated on the CNF surface was obtained. This PB-CNF nanocomposite was then used for glucose biosensing, demonstrating a sensitivity of $35.95 \mu\text{A}^{-2} \text{mM}^{-1}$ from 0.02-12 mM after glucose oxidase (GO) was drop-casting onto the modified electrode.

Table 2.3: MeHCF-based nanocomposite modified electrode and its sensing performance (effect of morphology).

Target analyte	Type of electrode	Linear range	Sensitivity ($\text{mA M}^{-1} \text{cm}^{-2}$)	Detection limit (μM)	Ref.
H_2O_2	PB/Hollow-PPy	5.0 μM -2.775 mM	484.4	1.6	Yang et al. (2016)
	PPy-PB	0.99 μM -8.26 mM	35.2	0.23	Miao & Liu, (2009)

(d) Hydrophilicity

Hydrophilicity contributes to sensitivity by allowing penetration of hydrophilic analytes through the electrode. The hydrophilicity of PB can be manipulated with incorporating with hydrophilic poly-(5-amino-1-naphthol) CP as shown in the work reported by (Limachi, Gonçalves, Cintra, & Córdoba De Torresi, 2013). A hydrophilic PB-poly-(5-amino-1-naphthol) nanocomposite was prepared, allowing permeation of H₂O₂ through both outer and bulk active site of the electrode and therefore presented a high sensitivity of 400 mA M⁻¹ cm⁻² towards H₂O₂.

Table 2.4: MeHCF-based nanocomposite modified electrode and its sensing performance (effect of hydrophilicity).

Target analyte	Type of electrode	Linear range	Sensitivity (mA M ⁻¹ cm ⁻²)	Detection limit (μM)	Ref.
H ₂ O ₂	PB/poly(5-NH ₂)1-NAP	Up to 0.7 mM	400	8	Limachi et al., (2013)

2.3.1.2 Stability

Stability can be divided into operational stability and storage stability. For the operational stability assessment, parameters such as analyte concentration, pH, and the continuous or sequential contact of the electrochemical sensor with the analyte solution, as well as buffer composition should be taken into consideration (Thévenot et al., 2001). For the storage stability determination, the important parameter is the state of storage (dry or wet) (Thévenot et al., 2001). The stability (operational and storage stability) of MeHCF could be increased by incorporating CP support or employing carbon or noble metal as a substrate.

In the case of MeHCF-CP nanocomposite, the adhesion of CP towards the electrode surface is robust enough to retain the electrode electrochemical activity. Tao and co-workers in 2013 revealed that the usage of poly (m-phenylenediamine) (PMPD) in a

hybrid film of PB-PMPD on a GCE surface increases the adhesion of nanocomposites to the electrode surface, consequently improving the operational stability of PB in neutral or weak alkaline solutions. This was evidenced by a higher degree peak current intensity in cyclic voltammogram (CV) of PB-PMPD if compared to pristine PB in pH 7.5. Moreover, the peak shape of PB-PMPD is still maintained even at pH 9.5 whereas the CV redox peak of pristine PB has already diminished. In another study, PPy was deposited onto PB/carbon nanopolyhedra (CNP) composite in order to enhance the stability of PB/CNP (J. Zhao et al., 2017). Although PB/CNP/PPy composite is in micrometre scale, it is worth mentioning that PPy can be a better option for covering the electrode surface than insulating Nafion® or PVP (polyvinylpyrrolidone) to protect electrodes from leaking. This is evidenced by the CV peak current of PB/CNP/PPy did not change significantly if compared to PB/CNP electrode. Moreover, this PB/CNP/PPy composite which still demonstrated the highest sensitivity (0.22 A M^{-1} from $0.75 \mu\text{M}$ to 1.65 mM) among all other hydrazine electrochemical sensors as tabulated in their report. On the other hand, the PB-PANI coated carbon nanotube (CNT) electrode covered by insulating PVP displayed a relatively low sensitivity ($0.91 \text{ mA M}^{-1} \text{ cm}^{-2}$) towards H_2O_2 (Sheng, Zhang, Wu, Zheng, & Tang, 2015) as compared to other nanocomposites which are tabulated in **Table 2.5**.

In the case of MeHCF-carbon nanocomposite, carbon nanomaterials are employed as support layer for the deposition of MeHCF, considering the ferric ions in the MeHCF structure exhibits high affinity towards carbon surfaces (Borisova et al., 2009). Husmann and co-workers (2014) have electrodeposited PB on CNT electrode surface to improve the operational stability of the PB towards H_2O_2 sensing. This stability effect was due to the π -to- π interaction between CNTs and PB, in which PB acts as the electron acceptor whereas CNT acts as the electron donor. Also, ionic interactions between Fe group of PB and functional groups at the surface of CNT contributed to a good interaction among these

materials (X. Zhai, Wei, Zeng, Liu, & Gong, 2006). On the other hand, the enhanced stability with graphene can be assigned to a high affinity between graphene with a 2D dimensional thin layer characteristic and the MeHCF nanoparticles (E. Jin et al., 2010).

For the MeHCF-noble metal nanocomposite, the affinity between nitrile group (-CN) of MeHCF and Au was able to enhance the stability of MeHCF via hybridisation of AuNPs and PB (Bai & Shiu, 2015). Z. Song and co-workers (2010) combined beneficial roles of AuNPs where the robust binding between gold nanoparticles and nitrile group of PB ensured the stable deposition of PB; electrodeposited AuNPs on surface of PB-MWCNT-AuNPs nanocomposite acted as immobilisation platform for antibodies and a protection layer to prevent leakage of PBNP.

As far as storage stability is concerned, the NiHCF/PANI/CNT electrode was stored in PBS buffer solution and the response current of the nanocomposite was only reduced by 11.3% after 40 days (Z. Wang et al., 2012). This is due to the support from PANI and CNT.

Table 2.5: MeHCF-based nanocomposites modified electrode and its affect to stability.

Target analyte	Type of electrode	Linear range	Sensitivity ($\text{mA M}^{-1} \text{cm}^{-2}$)	Detection limit (μM)	Ref.
H_2O_2	PMPD-PB	5 μM -1 mM	134	0.6	Tao et al. (2013)
	PVP protected PB/PANI coated CNT	NA	0.91	NA.	Sheng et al. (2015)
	PB/CNT paste electrode	NA	31.4	0.00479	Husman et al., (2014)
Hydrazine	PB/CNP/PPy	0.75 μM - 1.65 mM	220	NA	J. Zhao et al., (2017)
Glucose	PB/CNT	4 μM - 2 mM	0.6	2.5	X.Zhai et al. (2006)

NA = not applicable

2.3.1.3 Selectivity

Selectivity is defined as the signal output with the analyte alone versus to that with the interference alone, at a similar concentration as that of the analyte (Thévenot et al., 2001).

Noble metals, especially Ag possess the peroxidase mimicking behaviour like MeHCF materials (Jiang, Chen, Cao, & Huang, 2012). Hence, noble metal-MeHCF nanocomposites may be a promising candidate to replace enzyme peroxidase as shown in the work. For example, Pandey, Singh, & Pandey (2015) synthesised Ag-PB and Ag-Au PB nanocomposite for the electrocatalyst of H₂O₂ and the kinetic parameters was at least three-fold as compared to horseradish peroxidase.

In addition, the high affinity of Au towards thiols (-SH group) and amino groups may improve the selectivity of the amino-based detection such as L-cysteine sensor. For instance, Pandey, Pandey, & Chauhan (2012) synthesised a PB-AuNP-palladium (Pd) nanocomposite for electrochemical detection of L-cysteine and this electrochemical sensor demonstrated the lowest detection limit at 0.18 μ M from a range of 0.3-400 μ M.

Table 2.6: MeHCF-based nanocomposites modified electrode and its effect towards selectivity.

Target analyte	Type of electrode	Linear range	Sensitivity (mA M ⁻¹ cm ⁻²)	Detection limit (μ M)	Ref.
L-cysteine	PB-Au-Pd	0.3 μ M-0.4 mM	0.18	21.3	Pandey et al., (2012)

2.3.1.4 Other criteria

Other performance criteria that are not really can be enhanced by the formation of nanocomposites includes:

- Reproducibility: measure of the variation in a series of observations or results performed over a period (Thévenot et al., 2001).
- Limits of detection (LoD): lowest analyte concentration at which detection is feasible; may well reside at some concentration below the linear range of an assay, where the calibration curve is no longer valid (Thévenot et al., 2001).
- Linear concentration range: The maximum and the minimum concentration values that the sensor can response to (Thévenot et al., 2001).

2.3.2 Energy storage material

The most common energy storage devices comprise of batteries and supercapacitors (SC). Batteries produce electrical energy by the transformation of chemical energy via redox reactions at the anode and cathode, whereas supercapacitor (also known as electrochemical capacitor or ultracapacitor) is a novel energy storage tool that bridges the conventional capacitor and rechargeable battery. This device combines the benefits of both traditional capacitor and rechargeable batteries, which are high power density and high energy density. The supercapacitor is employed as a complement for rechargeable batteries to deliver the extra power needed in various applications. For instance, SC shielded rechargeable batteries from the high-frequency fast discharge/charge process in electrical vehicles (EVs) (F. Wang et al., 2017).

In recent times, MeHCF has gained a rising interest as the electrode material for supercapacitor and battery (rechargeable battery). Iron hexacyanoferrate (PB) and its derivatives are recently gaining its second life as a potential material in the energy storage field after extensively being employed in painting, photography and later in

electrochemical sensing field (Paoletta et al., 2017). This is mainly because of their tuneable open channels that allow insertion of both molecular and ionic species into the electrochemically active sites for faradaic redox reaction and hence no phase change occurs upon the charge/discharge of MeHCF. The theoretical specific capacity of PB can be as high as 170 mAh g^{-1} . Other advantages of MeHCF includes easy preparation, being non-toxic, economical, leading the investigation of PB and its analogues as promising energy storage materials.

2.3.2.1 Supercapacitor

Supercapacitors generally can be categorised into two types based on their energy storage mechanism: (i) electrical double layer capacitors (EDLC) that stored charges at the electrode-electrolyte interface (E_{dl}) through electrostatic interaction and (ii) pseudocapacitors that rely on Faradaic reaction (Winter & Brodd, 2004). The electrode is an important factor that affects the performance of supercapacitors. The commonly-used EDLC materials are carbonaceous materials, such as CNT and graphene whereas transition metal oxides and conducting polymer are widely used as electrode materials for pseudocapacitor.

More recently, the idea of intercalation pseudocapacitance was proposed. This phenomenon was due to the presence of pseudocapacitance contribution in some electrode materials for metal ion batteries via the physical manipulation of electrode materials (F. Wang et al., 2017). The most studied electrode materials for intercalation pseudocapacitor comprised of nanostructured TiO_2 (Augustyn et al., 2013), Nb_2O_5 (Wei, Wei, Ichihara, & Zhou, 2008) and MoO_3 (Brezesinski, Wang, Tolbert, & Dunn, 2010). Nonetheless, MeHCF might be able to group into this sub-category as it is a battery-like material that can be used as the material in supercapacitor (Li et al., 2013; Safavi,

Kazemi, & Kazemi, 2011; H. Wang et al., 2014) Some of the important criteria of supercapacitor that can be improved by forming nanocomposites are stated as below:

(a) Specific capacitance

Specific capacitance, C_{sp} is a significant parameter in determining the performance of a supercapacitor. In general, C_{sp} of MeHCF can be improved by forming nanocomposite with carbonaceous material and CP. Carbonaceous such as carbon nanofiber (CNF) and MWCNT are able to increase the conductivity and hence contributed to C_{sp} whereas CP possesses characteristics of high capacitance and high electrical conductivity. X. Zhang and co-workers (2018) have prepared a CoHCF/MWCNTs nanocomposite and this nanocomposite exhibited C_{sp} 109% higher than of pure CoHCF. In another report, the PPy/NiCoHF nanocomposite showed an enhancement in C_{sp} (380 F g^{-1}) as compared to pristine PPy (258 F g^{-1}).

As mentioned earlier, the ternary composite demonstrated improved electrochemical performance than their pristine forms or even their binary composites, attributed to the synergistic effect from all three constituents. Hence, have reported a ternary PPy-PB-GO nanocomposite, which exhibited better performance as compared to the binary materials (PPy-PB and PPy-GO nanocomposite), in term of C_{sp} and cycling stability (will be discussed in section (b)). PPy-PB-GO nanocomposite demonstrated the highest C_{sp} among PPy and PPy-GO. All the parameters of MeHCF based materials as supercapacitor are tabulated in **Table 2.2**.

(b) Cycling stability

MeHCF has low cycling stability due to gradual dissolution during potential cycling (Martínez-García et al., 2006). To solve this main disadvantage, carbon nanomaterials were employed to form nanocomposite with MeHCF due to carbonaceous materials are

EDLCs with excellent cyclic life (>10,000 cycles). Also, it is very often that MeHCF-carbon nanocomposites possess higher C_{sp} . For instance, Luo and co-workers (2015) have prepared the PB/rGO nanocomposite and 92 % of recorded C_{sp} was persisted after 1000 cycles whereas C_{sp} retention of PB was only 58 %.

Table 2.7: MeHCF-based nanocomposite as supercapacitors.

Electrode material	Current density ($A\ g^{-1}$)	Specific capacitance ($F\ g^{-1}$)	Ref.
PB-PANI	1.5	774	Amarnath & Sawant (2019)
PPy/NiCoHCF	10	529 (aqueous) 668 (non-aqueous)	Ensafi, Ahmadi, & Rezaei (2015)
PB-PPy-GO	5	525.4	Zou et al. (2016)
CoHCF/CNF/PPy	0.5	512	Rawool, Punde, Rajpurohit, Karna, & Srivastava (2018)
Interlocked PB-rGO	0.25	428.83	M.Zhang, Hou, Halder, Ulstrup, & Chi (2017)
CoHCF/rGO	1	340	J. G. Wang, Zhang, Liu, & Wei (2017)
CoHCF	1.4	318	J. G. Wang et al. (2017)
Meso-CoHCF	1	314	Yue et al. (2015)

2.3.2.2 Batteries

PB and its derivatives are promising materials for batteries due to their high electrochemical reversibility, as well as low cost. Also, these materials have been investigated as both cathode and anode materials of batteries. The usage of MeHCF based nanocomposites batteries is far lesser than the electrochemical sensor and supercapacitor. However, the formation of nanocomposite enables the increase of discharge capacity, cyclic stability and Columbic efficiency of PB. Wong and co-workers (2015) have synthesised the LiHCF-PPy- polystyrenesulfonate polymer hybrid as the lithium battery cathode. This reported material preserved 70 % of the capacity after 200 cycles in which presumably due to the presence of CP that enhanced the cycle stability and discharge

performances. You and co-workers (2016) also reported a PB/CNT composite material which can operate in low temperature (-25 °C).

2.3.3 Dual electrochemical applications

By adjusting the composition or designing suitable MeHCF composite, nanocomposites with multifunctional electrochemical functions could be achieved. Amarnath & Sawant (2019) have reported a PB-PANI composite for both sensing of H₂O₂ and supercapacitor purposes. Although these mentioned PB-PANI composites were not in nanometre scales, the PB cube on top of the PANI rod (200 nm in size) was 75 nm. The PANI- PB composite with core-shell arrangements (PANI shell and PB core) offered the highest C_{sp}, owing to the pseudocapacitance properties of both PANI and PB which can be accessed easily. On the contrary, the co-synthesised PANI-PB displayed a high sensitivity of 485 mM⁻¹ cm⁻² from 0.01-0.5 mM towards H₂O₂. Also, M. Zhang and co-workers (2017) have reported a hybrid composite of PB-graphene which is capable of both electrochemical sensing and acts as an electrochemical capacitor. The PB nanocubes are enfolded by rGO nanosheets to obtain a highly stable interlocked structure, which exhibited a specific capacitance of 429 F g⁻¹ and a decent sensitivity of 250 mM⁻¹ cm⁻² towards H₂O₂ from 2.5-475 μM with a LoD of 2 μM.

Up to date, these were the only two reports demonstrated the possibility of MeHCF-based nanocomposite used for dual electrochemical applications. Therefore, this is a great research potential and prospect to develop MeHCF-based nanocomposite for electrochemical sensor and supercapacitor.

2.3.4 Other application

2.3.4.1 Cesium decontamination

Cesium (^{137}Cs) is the main component of radioactive waste generated from nuclear plants. These radionuclides are generally treated by various approaches such as co-precipitation, adsorption/ion exchange, evaporation/concentration and chromatography methods. MeHCF has been used in Cs removal due to its open zeolite-like structure, which is promising for ion exchange for Cs^+ . The Cs removal with MeHCF based materials was reported using the adsorption or ion exchange method, as well as electrically switched ion exchange technique (ESIX). S.C. Jang and co-workers (2015) reported a PB/ rGO foam composite for decontamination of Cs from polluted water based on adsorption mechanism. This composite demonstrated a 99.5% removal efficiency with the maximum adsorption capacity (Q_{max}) of 18.67 mg g^{-1} , owing to the high surface area of 3D porous rGO foam and decent ion-exchange behaviours of the PB nanoparticles. Other examples of MeHCF based materials used for adsorbent for Cs removal includes CuHCF/SWCNT (Draouil et al., 2017), PB nanoparticles (S.-C. Jang et al., 2014) and CuHCF nanofilms. On the other hand, CuHCF/MWCNT nanocomposite was reported as ESIX material, in which CuHCF acted as ion exchange component and MWCNT facilitated the electron transfer and conductivity. The CuHCF deposited on dendritic morphology was available for Cs^+ exchange. This reported electrochemical adsorption system for CuHCF/MWCNT hybrid showed outstanding Q_{max} (310 mg g^{-1}) (Zheng et al., 2017). In contrast, the traditional adsorption system only demonstrated Q_{max} with a value of 230 mg g^{-1} .

2.3.4.2 Electrochromism

Electrochromism, a colour change stimulated by electrochemical reactions, has been drawing immense interest due to its potential application to various devices, especially as smart windows and rear-view mirrors in the vehicle (Rosseinsky & Mortimer, 2001). A

smart window is an electrically switchable glass or glazing to regulate light transmission, which is appealing for energy-saving in building and automobiles (Granqvist, Avendaño, & Azens, 2003).

PB which features a deep blue colour has been used in the field of electrochromism. Colour change from blue to white occurs during the reversible transition from PB to PW, which corresponds to the potential between +0.6 and -0.4 V vs. SCE (Hara et al., 2007). In addition, PANI-PB multi-coloured electrochromic electrode was reported by DeLongchamp & Hammond (2004). The conducting PANI increased the switching speed of the transition of colour from green to blue at the potential range from -0.2 to -0.6 V (vs. SCE).

2.3.4.3 Photocatalyst

MeHCF also has been used as photocatalyst such as photo-oxidation of water. PB catalysed the photo-oxidation of water in the presence of tris (2,2' bipyridine ruthenium (II) complex) (Christensen, Harriman, Neta, & Richoux, 1985). Besides that, CuHCF has been reported as catalyst for sacrificial photo-reduction and photo-oxidation of water with visible light (Tennakone, Wickramanayake, & Fernando, 1987).

2.4 Method development for preparation of MeHCF nanocomposite

In the past decades, researchers have extensively investigated the preparation of MeHCF composites by various methods. The preparation strategies are of great significance due to these synthetic methods imposed upon the resulting products in terms of the morphology, thickness as well as arrangement or composition of each material in the nanocomposite and hence their performance or the applications. Each approach has its respective perks or to suit different material and purpose. The methods used for synthesising MeHCF nanocomposites are named as:

- i) Electrodeposition
- ii) Chemical approach
- iii) Photochemical synthesis
- iv) Layer-by-layer assembly
- v) Combination of electrodeposition and chemical methods

The schematic diagram below illustrates the arrangements of nanocomposites formed by different methods.

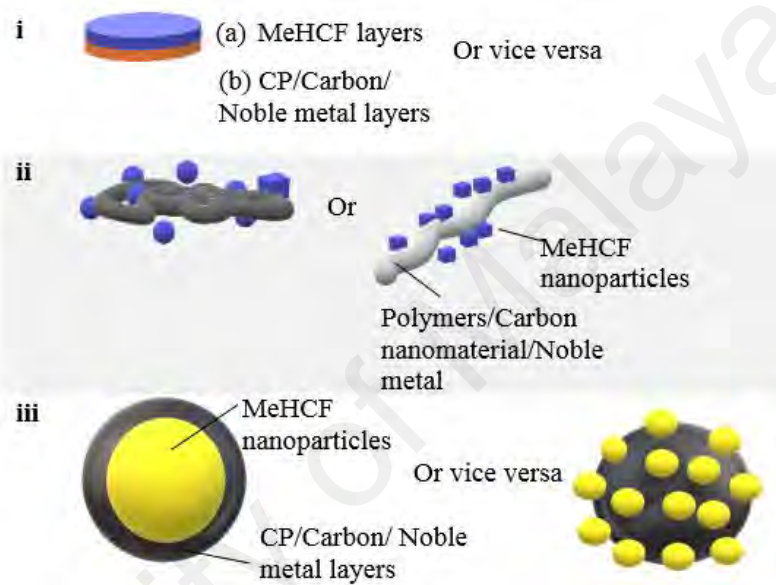


Figure 2.1: Schematic diagram of various nanocomposite structure: (i) bi-layered MeHCF-CP/carbon/noble metal; (ii) single layer MeHCF-CP/carbon/noble metal (irregular or regular shape); (iii) MeHCF-CP/carbon/noble metal core-shell structure.

Electrochemical deposition (ED) or electropolymerisation is the common method for preparing MeHCF nanocomposites, owing to its high stability, long term life and good reproducibility (Rapecki, Donten, & Stojek, 2010). Also, conducting materials can be deposited on the electrode surface easily by this approach. Furthermore, the size and shape of the conducting nanoparticles can be regulated facilely by changing the parameters of ED.

2.4.1.1 Two-steps electrodeposition

A two-steps electrochemical procedure is often employed in the electrodeposition of MeHCF nanocomposites with two layers, especially for MeHCF-CP nanocomposite. The schematic diagram of bilayer MeHCF nanocomposite is shown in **Figure 2.2 (i)**. Using MeHCF-CP composite as an example, CP was first deposited onto an electrode by electropolymerisation of the monomer, followed by the electrochemical reduction of metal hexacyanoferrates in a second electrolyte solution containing the metal (ferric or copper(II)) and ferricyanide ions. The CP can be synthesised by electropolymerisation with constant applied potential strategy or galvanostatic polymerisation whereas MeHCF were electrodeposited on the CP, commonly by potential cycling deposition strategy or applied potential strategy (Somani & Radhakrishnan, 2002; H. Zhao, Yuan, Adeloju, & Wallace, 2002) Alternately, the process can also be reversed, in which MeHCF was electrodeposited first on the substrate (Derwinska et al., 2003). These two steps method will form CP/MeHCF or MeHCF/CP nanocomposites with two different layers. CP can be replaced by other materials such as carbon-based material or noble metal. However, metal is usually deposited with constant potential whereas carbon material is normally drop-casted on electrodes followed by ED of MeHCF on carbon material surfaces (Y. Zhang, Sun, Zhu, Shen, & Jia, 2011).

In order to merge a MeHCF electrocatalyst onto the CP, another type of two-steps electrodeposition approach is used to form ferricyanide ions-CPs composites by potential cycling in electrolytes containing monomers and metal or ferricyanide ions (Fiorito et al., 2006; Gonales, Matsubara, Rosolen, & Córdoba De Torresi, 2011). It was then followed with the second step of potential cycling in an electrolyte consisting of the target metal ions to form MeHCF-CP. By this mean, a layer of MeHCF-CP nanocomposite will be fabricated (as shown in **Figure 2.2 (ii)**). Nevertheless, this type of electrodeposition method was only used for the formation of MeHCF-CP nanocomposite.

2.4.1.2 One-pot electrodeposition

One step electrosynthesis can be conducted via CV or the constant potential method to synthesis MeHCF based nanocomposites. Z. Wang and co-workers (2012) reported that the PANI/NiHCF was electrodeposited by CV approach due to the intrinsic characteristic of PANI and NiHCF. The PANI formed was first doped with $\text{Fe}(\text{CN})_6^{3-}$, and then, Ni^{2+} was doped onto the reductive state of PANI, where ferricyanide was also reduced to ferrocyanide in the CV potential range from -0.2 V to +0.85 V vs. saturated calomel electrode (SCE). The polymer PANI and the inorganic polynuclear NiHCF compound in the cubic hybrid microstructure should interact electrostatically with each other since the partially oxidised PANI was positively charged while NiHCF was in anionic state. Furthermore, a cubic of PANI-NiHCF as shown in **Figure 2.2 (ii)** will be formed on a CNT modified electrode. On the other hand, the constant potential method (+0.4 V vs. SCE) was employed to form PB-MWCNT on Au surface (C. Zhai, Sun, Zhao, Gong, & Wang, 2013). However, there is no study up to date to synthesise noble metal and Au in one-pot ED solution.

In the case of forming nanocomposite with CP that was not electroactive/conducting at the region where MeHCF redox species are electroactive, such as PPy, one-pot pulse ED method was employed (Kulesza et al., 2001). The initial approach was reported in such a way that the nanocomposite film, PB-PPy was deposited on the electrode surface by a one-stage procedure which comprised of multi CV in a solution containing Fe(III), $\text{Fe}(\text{III})[\text{CN}]_6$ and pyrrole. The potential employed was in the region of the monomer oxidation and the MeHCF salt reduction, which results in the formation of PPy and PB, respectively. However, it is hard to form both PB and PPy in the same potential range, owing to only small amounts of PPy was formed if the positive potential employed was lower than -0.7 V vs. Ag/AgCl (1 M KCl). On the other hand, the PB activity will be diminished if the upper switching potential is higher than 0.8 V vs. Ag/AgCl (1 M KCl)

(Karyakin & Chaplin, 1994). Hence, one-pot pulse ED was proposed by the researchers to form a composite film (Zolotukhina, Bezverkhyy, & Vorotyntsev, 2014). In the approach, periodical order comprised of the anodic pulse which was able to electro-oxidise the polymer on the electrode surface whereas cathodic pulse electro-reduces the precursor into inorganic MeHCF constituents of the composite. The effect of contrast potential towards both polymer and MeHCF components can be minimised by this mean. Moreover, the pattern, thickness and composition of the deposited composite can be manipulated by deposition potential (Özkale et al., 2014).

2.4.1.3 Sonoelectrodeposition

Sonoelectrodeposition is a relatively new electrodeposition technique to form MeHCF composite which performed under ultrasonic radiation. The size and dispersity can be controlled by altering the amplitude of the radiation. For example, Hostert, Alvarenga, Marchesi, Soares, & Vidotti (2016) presented a multiple sequence of the constant potential method ED of PPy and PB nanostructure under ultrasonic radiation. This report revealed that the film morphology varies from large aggregates into tiny particles which deposited uniformly on the electrode surface via changing the amplitude of radiation.

2.4.2 Chemical approach

The advantages of chemical approach are that this route can be used without any external devices such as potentiostat, it is rapid and is able to increase the stability of the composites via a chemical redox reaction. Due to the relative potential between additional materials and PB, this method is very popular in preparing MeHCF nanocomposite electrode as mentioned in the previous part. For example, Zou and co-workers (2016) have utilised one-pot chemical approaches to synthesis a ternary composite of PPy-PB-GO in which PPy works as the reducing agent and iron(III) ions as an oxidising agent for pyrrole monomer. This one-pot technique is also employed in the template-assisted

chemical approach. As mentioned earlier, special morphology (aerogel) PPy-PB was synthesised with the aid of methyl orange (MO) and ferricyanide ions (Tuo et al., 2016). A core-shell structure or single layer MeHCF based nanocomposites as demonstrated in **Figure 2.22 (iii)** will usually be fabricated by this type of chemical approach.

2.4.3 Photochemical synthesis

The photochemical method offers benefits including mild synthesis condition, and is capable to alter conditions in a stepwise means, specific rate control and morphology control. For instance, rGO-PB nanocomposite has been prepared via this means (Santos, Katic, Toledo, & Bonacin, 2018). A quartz cuvette containing the precursor solution was irradiated with UV light (400 nm) for 24 hours. The photochemical approach is a rather new approach used to prepare MeHCF based nanocomposite.

Nonetheless, the disadvantage of nanocomposite formed via all these chemical approaches (including photochemical synthesis) is the in-situ modification of electrodes could not be achieved. The nanocomposite was typically produced in advance and deposited on electrodes by the drop-casting method. Therefore, by exploiting the similar redox reaction between PB and PPy, PB-PPy nanocomposite was synthesised with the layer-by-layer assembly method in our previous study to accomplish in-situ electrode modification. This as synthesised nanocomposite particles size was in the nanometre scale. The synthesis details will be explained further in the following part.

2.4.4 Layer-by-layer assembly

The layer-by-layer (LBL) assembly was introduced to archive in-situ modification of electrodes. This self-assembly (SA) or LBL was first established in 2001 (Millward et al., 2001). Briefly, this approach is established on the sequential deposition of the oppositely charged particles. LBL assembly is a facile and effective method to create polymer nanocomposites and it can be employed for almost all materials. This method is

constantly forming novel materials and various applications. The other benefits include its ability to synthesise nanocomposites with adjustable composition and structures, as well as controlled thickness in nanoscale precision.

The novel self-assembly (SA) strategy which based on multiple sequential absorptions was inspired by these layer-by-layer assembly works reported before. For instance, Y. Liu, Chu, & Jin (2009) reported a self-assembled PB film on platinum foil formed by multiple sequential adsorptions of ferric ions and hexacyanoferrate ions. Platinum foil was successively immersed in two solutions containing ferric and ferrocyanide ions respectively. In addition, Y. Zhang, Chu, Shi, & Jin (2011) presented a self-assembled PB NPs based on multiple sequential absorptions produced of PB NPs on the surface of a positively charged PDDA polymer layer.

This method possesses advantages such as simplicity and great controllability for the formation of the nanostructure. Consequently, the weakness is time-consuming as a certain amount of deposition cycles are needed to synthesize an integrated film (Chu, Liu, & Jin, 2017).

2.4.4.1 Combination of electrodeposition and chemical approach

The combination scheme of electrodeposition and chemical methods have been used in some studies. This method basically starts with the deposition of CP by means of electropolymerisation or drop casting, subsequently by electrodeposition or SA of MeHCF onto the CP film. The previous reports included the ED of poly(o-phenylenediamine) (PoPD) using cyclic voltammetry, subsequently by the SA of PB on the pre-deposited PoPD films (Ojani, Hamidi, & Raouf, 2016), alternate SA and ED procedures were performed to form MWCNT-PET-Au/PB composites film (Y. Zhang, Chen, Gao, Chen, & Lin, 2012) and ED of PB on drop-casted PANI-HNT film (Sheng et al., 2015). Thus, to enhance the electrochemical stability of the composite, the CP layer

will sometimes be electrodeposited on top of the MeHCF layer. For instance, PPy was electrodeposited on the surface of the SA PB/GQD (graphene quantum dot) layer in order to increase the stability (L. Wang et al., 2016).

University of Malaya

CHAPTER 3: METHODOLOGY

This chapter focuses on the materials, techniques and experimental methods that were employed in this research to prepare and characterise the electrochemical sensors and electrochemical capacitor. The characterisation techniques mainly divided into surface and electrochemical characterisations. The surface characterisations employed include Fourier transform infrared spectroscopy (FTIR), field-emission scanning microscope (FESEM) and energy dispersive X-ray spectroscopy (EDX) whereas the electrochemical methods include cyclic voltammetry, amperometry, electrochemical impedance spectroscopy (EIS) and galvanostatic charge-discharge test (GDC). Other method for analysis in this research was high performance liquid chromatography (HPLC).

3.1 Material

All chemicals were of analytical grade and used as received. Potassium ferricyanide, potassium ferrocyanide, iron (III) nitrate nonahydrate were purchased from Friendemann Schmidt. Copper (II) chloride and pyrrole (99.5%) was purchased from Sigma-Aldrich whereas nitric acid (63%) was purchased from R&M chemicals. Deionised (DI) water was used for all experiments.

3.2 Method of preparation for MeHCF-PPy nanocomposite

3.2.1 Pre-treatment of glassy carbon electrode

Glassy carbon electrode (GCE) was used as the base electrode. The clean GCE was polished with alumina (1, 0.1, 0.05 mm diameter) slurries until a mirror surface was observed. The polished GCE was subsequently washed by DI water and ultrasonicated in DI water and ethanol, respectively, for one minute and dried in air.

3.2.2 Self-assembly MeHCF-PPy nanocomposite

3.2.2.1 PB-PPy

For the self-assembly (SA) of PB-PPy film, two solutions were prepared. Solution A: 0.01 M $K_3[Fe(CN)_6]$ + 0.01 M $Fe(NO)_3 \cdot 9H_2O$ + 0.10 M KNO_3 + 0.10 M HNO_3 and Solution B: 0.10 M pyrrole solution + 0.10 M KNO_3 + 0.10 M HNO_3 . Firstly, the pre-cleaned glassy carbon electrode (GCE) was successively dipped into solution A, followed by being immersed in deionised (DI) water and absolute ethanol, respectively. The electrode was then dipped into the solution B followed by consequent immersing in DI water and absolute ethanol, again. The dipping time in solutions A and B was 1 minute, respectively. These above-mentioned steps are denoted as one deposition cycle. The SA PB-PPy was prepared using 10, 20, 30 and 35 number of deposition cycles (NDC), which were then named as SA PB-PPy (10), SA PB-PPy (20), SA-PPy (30) and SA PB-PPy (35), respectively.

3.2.2.2 CuHCF-PPy

CuHCF-PPy was self-assembled on rGO electrodeposited GCE. For the preparation of rGO, rGO was electrodeposited on GCE with potential cycling from 0 to 1.5 V vs. Ag/AgCl (sat. KCl) with a scan rate 5 mV s^{-1} . 1 mg mL^{-1} of GO with 0.1 M KCl as supporting electrolyte solution was used. Graphene oxide (GO) was prepared by the Hummers method (Siong et al., 2018).

In this part, the $Fe(NO_3)_3$ - $K_3[Fe(CN)_6]$ solution was replaced with $CuCl_2$ - $K_3[Fe(CN)_6]$ to form CuHCF instead of PB. Briefly, two solutions containing $K_3[Fe(CN)_6]$ - $CuCl_2$ (Solution 1) and pyrrole (Solution 2) were prepared individually. The pre-treated GCE was sequentially immersed into the Solution 1, DI water, ethanol, Solution 2, DI water and ethanol. These mentioned steps are stand for one deposition cycle. CuHCF-PPy was synthesised using 5, 10 and 15 NDC.

3.2.2.3 PB

The pure PB was also self-assembled on the GCE as control by using the previously reported method with slight modification (Liu, Xu, & Chen, 2002). The composition of solution I and solution II were as follows, Solution I: 0.01 M $K_4[Fe(CN)_6]$ + 0.10 M KNO_3 + 0.10 M HNO_3 . Solution II: 0.01 M $Fe(NO_3)_3 \cdot 9H_2O$ + 0.10 M KNO_3 + 0.10 M HNO_3 . The SA PB was also synthesised using 10 and 20 deposition cycles, which were then named as SA PB (10) and SA PB (20). Briefly, the pre-treated GCE was first dipped in Solution I and Solution II. The GCE was then washed with DI water and absolute ethanol after dipping in each solution, respectively.

3.2.2.4 CuHCF

The pure CuHCF was prepared on the GCE surface as control in this experiment. The precursors used were selected according to earlier reports (Makowski, Stroka, Kulesza, Malik, & Galus, 2002). The Solution II was replaced by $CuCl_2$ solution. The procedure was similar to the formation of PB in **Section 3.2.2.3**.

3.2.3 Electrosynthesis method of PB-PPy

3.2.3.1 Electrochemical experimental set-up

All the electrochemical measurement including cyclic voltammetry, electrochemical impedance spectroscopy (EIS) and chronoamperometry were performed using a potentiostat/ galvanostat Metrohm Autolab model PGSTAT-302N. A conventional three-electrodes system was used as shown in **Figure 3.1**, which was composed of glassy carbon electrode (GCE) with a geometrical area of 0.07 cm^2 or a modified GCE as working electrode, saturated KCl Ag/AgCl reference electrode (standard electrode potential E^0 against standard hydrogen electrode (SHE) is $0.230V \pm 10mV$) and platinum rod as counter electrode, respectively.

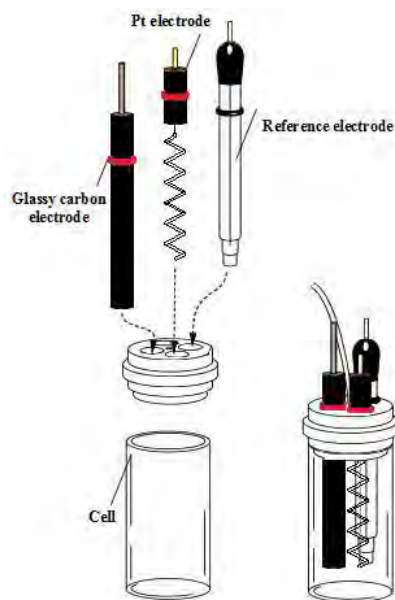


Figure 3.1: Three electrodes electrochemical system.

3.2.3.2 One-pot pulse electrodeposition of PB-PPy

The electrosynthesis method of PB-PPy film was adapted from the previous works (Özkale et al., 2014; Zolotukhina et al., 2014). For this purpose, the electrolytes with the same chemical compositions as SA, but with a lower concentration were used for one-pot pulse ED. The concentration of the salt and monomers was adjusted to sufficiently low to avoid the spontaneous redox reaction between PB and PPy. Hence, the mixture of electrolyte used in this experiment was supposed to be the highest concentration, in which the Fe salt does not form a blue colloidal solution with pyrrole monomer within the course of the ED. A solution of 0.50 mM $K_3[Fe(CN)_6]$ + 0.50 mM $Fe(NO)_3 \cdot 9H_2O$ + 1.00 mM pyrrole monomer + 0.10 M KNO_3 + 0.10 M HNO_3 was employed as the ED electrolyte. Firstly, one thin layer of polypyrrole was grown at +0.80 V (vs. Ag/AgCl) with a total deposition time of 15s. Subsequently, the intermediate sandwich PB-PPy layer was electrodeposited by the pulse ED. The polymer (PPy) was grown using an anodic phase (+0.80 V, one second) while metallic PB was grown at the cathodic phase (5.8 sec.) at a more negative potential +0.40 V. During the ED, a rest phase of 45 sec. was employed

between the deposition of PB and PPy. The ED PB-PPy was prepared using 10, and 20 electrodeposition repetitions, which were then named as ED PB-PPy (10) and ED PB-PPy (20).

For all the PB-based electrodes, they were preconditioned by cyclic voltammetry from -0.1 V to 0.5 V vs. Ag/AgCl (sat. KCl) in 0.1 M KNO₃/HNO₃ as supporting electrolyte until a stable voltammogram was obtained (Pellitero et al., 2017).

3.3 Characterisation of modified electrode

Various techniques were used to characterise the modified electrode. This section is devoted to explain the basic principles of the involved techniques.

3.3.1 Surface characterisation

3.3.1.1 Fourier transform infrared spectroscopy

Fourier Transform Infrared spectroscopy (FTIR) is an analytical technique used to analyse molecular configuration, functional group and bonding situation for organic and inorganic materials. It measures the absorption of infrared light (IR) wavelengths by the sample based on the vibration of the atoms within a molecule (Amand & Tullin, 1999). This absorption spectrum corresponds to the structure and bonding of the molecules. A Perkin Elmer Spectrum 400 FT-IR/FT-FIR spectrometer was used in this study. A total of 12 scans were collected for each spectrum at a resolution of 2 cm⁻¹ in the spectral range of 4000 to 500 cm⁻¹. However, only the spectrum from 4000 to 1000 cm⁻¹ was plotted as no significant peaks in the range from 1000 to 500 cm⁻¹.

3.3.1.2 Field emission scanning electron microscopy

Field emission Scanning Electron Microscopy (FESEM) is a technique used to acquire surface morphology. Briefly, secondary electrons are released from sample spot after bombards by the primary electrons which deflected by electronic lenses (Geert-Jan Janssen, 2005). The digital images were produced by a detector of the secondary electron. The surface images of modified electrode were acquired by a Field-emission Scanning Electron Microscope (FESEM) (Hitachi SU8200).

3.3.1.3 Energy dispersion X-ray spectroscopy

Energy dispersion X-ray spectroscopy (EDX) was a chemical microanalysis technique performed in combination in SEM. The elemental composition of the sample was obtained by perceiving the x-ray emitted from the sample during bombardment by an electron beam (Abd Mutalib, Rahman, Othman, Ismail, & Jaafar, 2017) . The EDX data was also obtained by Hitachi SU8200.

3.3.2 Electrochemical characterisation

3.3.2.1 Cyclic voltammetry

Cyclic voltammetry is the most widely used technique for acquiring qualitative information about electrochemical reactions. It is often the first experiment performed in an electroanalytical study. Cyclic voltammogram is the resulting plot of current versus potential. It offers a rapid location of redox potentials of the electroactive species and convenient evaluation of the effect of media upon the redox process. It also can provide other information such as the electrochemical kinetics of electrochemical sensor (surface-controlled or diffusion control), the surface coverage of the modified electrode and number of electrons involved in the reaction (Bard & Faulkner, 2002; J. Wang, 2006a).

3.3.2.2 Electrochemical impedance spectroscopy

Electrochemical impedance spectroscopy (EIS) is a powerful technique conducted to investigate the electrical properties of materials and the electrochemical process occurs at the interfaces of the electrodes. In this project, the potential in the electrochemical systems was conducted with respect to Ag/AgCl (sat. KCl) reference electrode and hence three-electrode cell set-up was used in this project. In general, EIS is measured by applying small-amplitude AC perturbation to the EC system and the variation of the impedance with frequency is recorded.

The parameters below were calculated for each frequency applied:

- Impedance modulus: $|Z|$ (Ω)
- Phase ($^\circ$)
- Real impedance, Z_{re}/Z'
- Imaginary impedance. $-Z_{im}/Z''$

The graphs generated include Nyquist plot ($-Z_{im}$ vs. Z_{re}) and bode plot ($|Z|$ vs. frequency and phase vs. frequency) (Lvovich, 2012a; Orazem & Tribollet, 2014)

3.3.2.3 Chronoamperometry

Chronoamperometry, which also known as amperometry involves stepping the potential of working electrode from a value at which no faradaic reactions occur to a potential at which the surface concentration of the electroactive species is effectively zero (J. Wang, 2006a).

In this research, chronoamperometry is mainly used for analytical purpose, the current measurements of the sensor were under constant potential/polarisation at a fixed time interval, while changing the analyte concentration. Additional transient background

contributions (associated with surface redox reactions) are common to solid-electrode chronoamperometric experiments.

3.3.2.4 Galvanostatic charge-discharge test

The galvanostatic charge-discharge (GCD) test is an important technique to investigate the electrochemical capacitance of materials under controlled current conditions. GCD can be considered as cyclic chronopotentiometry method (Bard & Faulkner, 2002). In this study, the GCD test was performed using a conventional three-electrode system. The materials of interest (PB-PPy) were deposited by the SA method on the working electrode. This method was widely used in the field of supercapacitor field to evaluate cycling stability and specific capacitance/areal capacitance.

The specific capacitance, C_{sp} ($F g^{-1}$) is calculated from the following equation (Y. Wang & Chen, 2014):

$$C_{sp} = \frac{It}{m\Delta V} \quad \text{Eq. 3.1}$$

Where i is current (A), t is the discharge time (s), m is the mass of the active material and ΔV is the voltage window (V).

The areal capacitance ($F cm^{-2}$) is calculated from the following equation (Huang et al., 2013):

$$C = \frac{Jt}{\Delta V} \quad \text{Eq. 3.2}$$

Where J is current density ($A cm^{-2}$), t is the discharge time (s), and ΔV is the voltage window (V).

3.3.3 Real-sample analysis

3.3.3.1 Pre-treatment of real sample

The vape solution purchased from the market was filtered with CHROMAFIL®Xtra PTFE syringe filter (0.20 µm) and diluted with DI water for analysis.

3.3.3.2 High performance liquid chromatography analysis

High performance liquid chromatography (HPLC) relies on interaction of analytes with the stationary phase and the mobile phase which resulted a separation of the compounds inside the analytes. In this study, the HPLC is coupled with a UV detector.

Shimadzu HPLC Pump LC 20-AT and Shimadzu DAD SPD-M20A were used for HPLC analysis of nicotine. The column used was Chromolith® HR RP-C18, which was purchased from Merck. The mobile phase was 70% of 0.1% formic acid: 30% acetonitrile with flow rate of 0.5 ml min⁻¹. The UV wavelength employed was 260 nm.

CHAPTER 4: RESULTS AND DISCUSSION

This chapter reports the novel fabrication methods of metal hexacyanoferrate (MeHCF)-based nanocomposites and their respective electrochemical applications. The first section begins with the comparative synthesis (self-assembly vs. one pot pulse electrodeposition) of Prussian blue (PB)-polypyrrole (PPy) nanocomposites and its application towards electrochemical sensing of the H_2O_2 . The second part focuses on the facile synthesis of another structure analogous to PB, copper hexacyanoferrate (CuHCF)-PPy nanocomposites and its electrochemical sensing of nicotine. Last part of this chapter reported on the potential of these MeHCF-polymer nanocomposites as supercapacitor and energy storage material.

4.1 Comparative synthesis methods for the preparation of Prussian blue-polypyrrole nanocomposite

The conventional method for the synthesis of PB film is based on the electrodeposition by using a solution comprised of ferric and ferricyanide ions with its supporting electrolyte (W. Zhao, Xu, Shi, & Chen, 2005). However, self-assembled PB thin film has been of significant interest, owing to its rapidity, simplicity and versatility in surface modification (Kong et al., 2015). To boost the performance of PB and to create novel properties based on the synergistic effect of PB composites (W. Jin et al., 2003), a lot of research works have been carried out to create PB composite. However, these reported PB-PPy nanocomposites were either prepared by the chemical method first, followed by drop-cast on the electrode or by electrodeposition approach.

To my best knowledge, no studies have been reported on PB-PPy nanocomposites synthesised using self-assembly (SA) method based on multiple sequential adsorptions of $FeCl_3$ - $K_3[Fe(CN)_6]$ and pyrrole. The objective of this work is to develop a very simple (facile) procedure, which will be efficient for the modification of glassy carbon electrode

(GCE) by PB and PPy-based nanocomposites, towards electrochemical applications. The electrocatalytic reduction of H_2O_2 was designated for its applications to investigate the applicability of this novel SA method as electrochemical sensor.

This alternate self-assembly attempt simplifies the extensive preparation of the PB-PPy nanocomposites (chemical method) or the requirement of an external voltage for the preparation (electrodeposition). Furthermore, this approach permits the control of electrochemical behaviour and its sensitivity towards H_2O_2 by simply tuning the number of deposition cycle. In the present SA procedure, the redox reactions of $\text{FeCl}_3\text{-K}_3[\text{Fe}(\text{CN})_6]$ in acidic solution and pyrrole occurred spontaneously. The $\text{FeCl}_3\text{-K}_3[\text{Fe}(\text{CN})_6]$ acted not only as a precursor for PB but also as strong oxidants for pyrrole (Itaya et al., 1982) while pyrrole played the reducing role in this reaction (E. Jin et al., 2012). Also, the entire method for PB-PPy nanocomposites preparation was performed in an aqueous media without any additional chemical reagents.

To compare the present SA method with the conventional electrodeposition approach, PB-PPy was also fabricated by electrodeposition method. For this purpose, PB-PPy was synthesised by one-pot pulse electrodeposition (ED) method with slight modification from the previous report (Özkale et al., 2014; Zolotukhina et al., 2014), in order to mimic the multiple absorptions by SA procedure as close as possible. In this section, PB-PPy nanocomposite was prepared by two different approaches, namely one pot ED and novel SA based on multiple sequential adsorptions of $\text{FeCl}_3\text{-K}_3[\text{Fe}(\text{CN})_6]$ and pyrrole. A comparative study in terms of morphology and its electrochemical, as well as electrocatalytic behaviours, was presented.

4.1.1 Mechanism of formation of PB-PPy

Firstly, PB-PPy was self-assembled on the glassy carbon surface with a very simple procedure. The proposed route for the preparation of PB-PPy film can be described as follows and illustrated in **Figure. 4.1**. Firstly, $\text{FeCl}_3\text{-K}_3[\text{Fe}(\text{CN})_6]$ was absorbed on the GCE surface due to the hydrophilic carbon surface which has a high affinity to ferric ions (Borisova et al., 2009). Pyrrole was then polymerised by $\text{FeCl}_3\text{-K}_3[\text{Fe}(\text{CN})_6]$ in acidic solution which is a strong oxidant for pyrrole. At the same time, Fe^{3+} was reduced to Fe^{2+} by pyrrole (Eq. 4.1) and reacted with $[\text{Fe}(\text{CN})_6]^{3-}$ ions to form PB particles (Eq. 4.2) which led to the formation of one layer of dark blue PB-PPy thin film. Repetitive cycling of the PB/PPy self-assembled process grew a thicker film. The mechanism of the formation of PB is as follows:

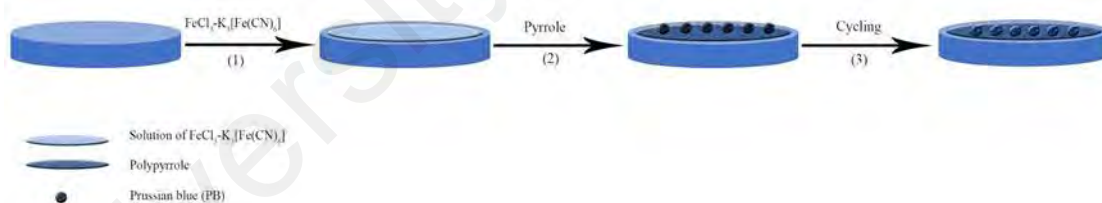
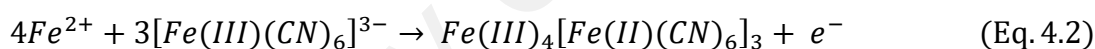


Figure 4.1: Schematic diagram of the preparation process of PB-PPy film.

For the one-pot pulse electrodeposition, the PB-PPy nanocomposite layer was electrodeposited by the pulse ED. The polymer (PPy) was grown using an anodic phase while metallic PB was grown at the cathodic phase.

4.1.2 Comparison of surface characterisation for PB-PPy film

4.1.2.1 Field emission scanning microscopy

Figure 4.2 shows field emission scanning electron microscopy (FESEM) images of PB-PPy electrode prepared with two different methods, ED and SA, respectively.

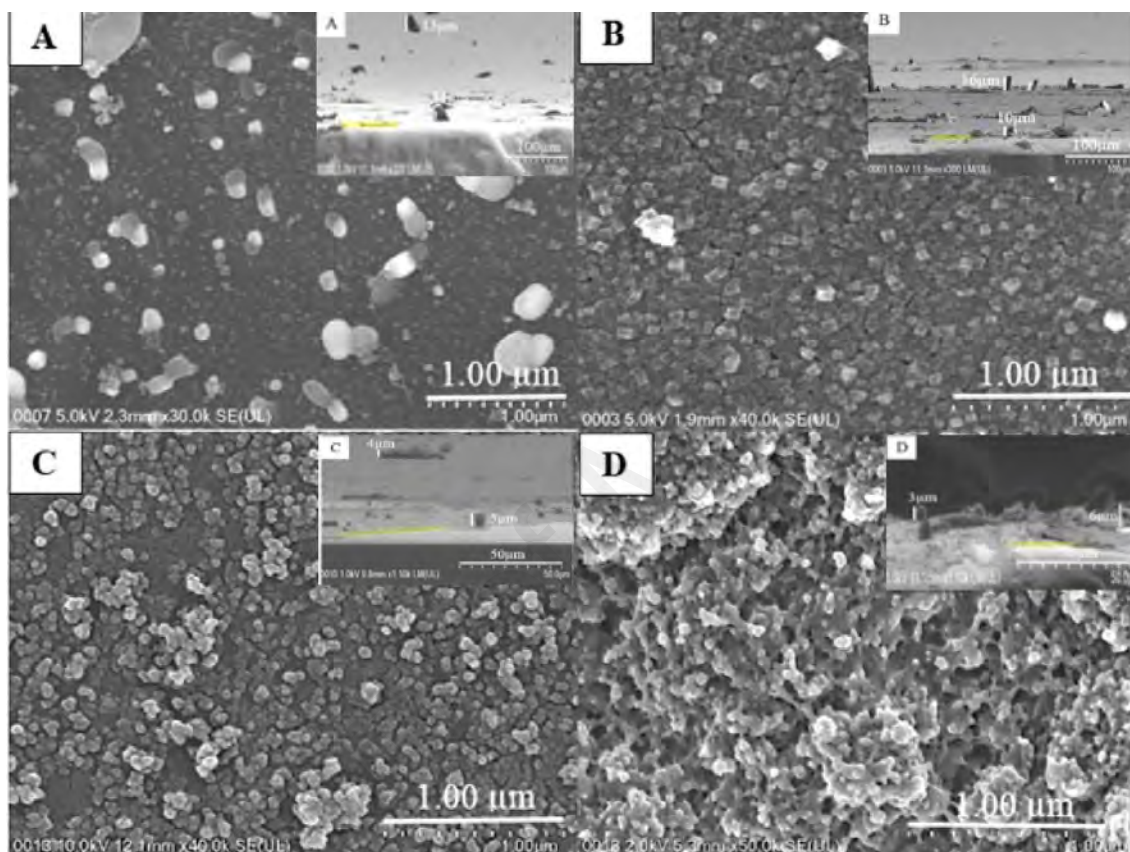


Figure 4.2: FESEM images of (A) ED PB-PPy (10), (B) ED PB-PPy (20) and (C) SA PB-PPy (10) and (D) SA PB-PPy (20). Inset: Cross-sectional of FESEM images.

According to **Figure 4.2 (A)**, ED procedure with 10 repetitions led to the formation of tiny cubic PB and irregular seeds PB-PPy which yet to be fully developed into cubic form. When the repetitions increased till 20, the nanocube of PB started to appear on top of the PPy film as shown in **Figure 4.2 (B)**. The type of PB deposited was the typical PB as it had a cubic lattice organization (Y. Zhang, Chu, et al., 2011) On the other hand, PB-PPy fabricated by the SA method had a very distinctive morphology. From **Figure 4.2 (C)**, the SA PB-PPy (10) film displayed an irregular globular morphology, which was in close

agreement with previous reports (Hostert et al., 2016; Tao et al., 2013). This morphological variation might be attributed to the complete growth of PB particles into cubic framework hindered by space limitation. These polymers acted as the host to the PB particles (Hostert et al., 2016) and provided the nucleation site for it (Y. Zhang, Chu, et al., 2011). According to **Figure 4.2 (D)**, it was clear that the particles with rougher surface and thicker PB-PPy film were formed on the SA PB-PPy (20) electrode. The PPy was overlapped with each other and the linkage between these polymers was clearly shown in **Figure 4.2 (D)**. The cross-sectional images of the modified electrodes are also shown in the insets of **Figure 4.2** which indicated uneven surfaces. Some part of surfaces has thick agglomeration with the estimated range of particle sizes from 3 to 16 μm . However, the thickness of the highlighted area from all the inset of **Figure 4.2** can be estimated to be less than 1 μm .

The average particle size and its distribution of PB-PPy synthesized by ED and SA methods were almost similar, as shown in **Figure 4.3 (A)** and **(B)**, correspondingly. The particles size of ED and SA PB-PPy was in the range of 51.1-63.2 nm, respectively. On the contrary, the PB particles which were electrodeposited on GCE without the co-deposition of polymer were 200 nm in sizes according to the previously reported work (Tao et al., 2013). The small size, large surface-to-volume ratio and the increase of the surface activity of nanoparticles when compared to those of bulk materials, qualify their use in catalysis and sensing.

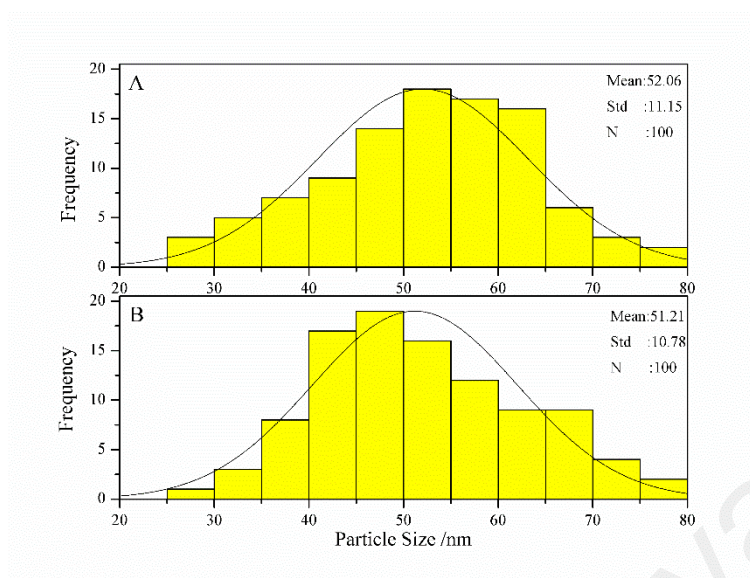


Figure 4.3: Particles size distribution of (A) ED PB-PPy (20) and (B) SA PB-PPy (10).

University of Malaya

4.1.2.2 Energy dispersive X-ray spectroscopy

Energy dispersive X-ray spectroscopy (EDX) analysis was employed to verify the elemental composition of PB-PPy film formed on the surface of the electrode. **Figure 4.4** presents the EDX spectra of PB-PPy. Element Fe was detected on all spectra, supporting that the PB was successfully deposited on the electrode. Moreover, the elements C, N and O were found in all spectra, showing PPy was successfully polymerised on the electrode.

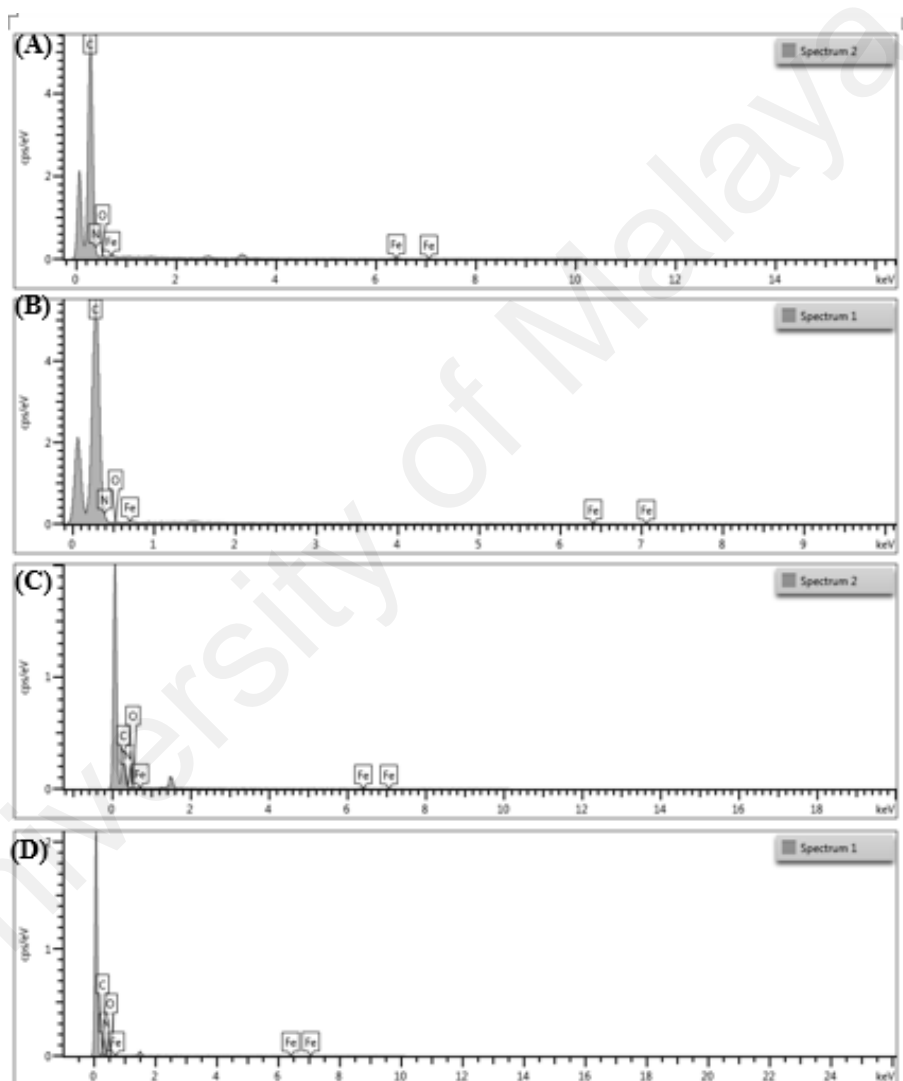


Figure 4.4: EDX spectra of (A) ED PB-PPy (10), (B) ED PB-PPy (20), (C) SA PB-PPy (10) and (D) SA PB-PPy (20).

4.1.2.3 Fourier transform infrared spectroscopy

The Fourier transform infrared spectroscopy (FTIR) transmission spectra of ED and SA PB-PPy composites are illustrated in **Figure 4.5 (A)** and **(B)**, respectively. These results further confirmed that PB and PPy were successfully deposited on all modified electrodes. The absorption peaks observed at 3300 and 2904 cm^{-1} are attributed to the N-H stretching vibration in the PPy rings. The C-N stretching vibration and C-H in plane ring deformation and bending modes appeared at 1353 and 1614 cm^{-1} (Sahoo, Jung, So, & Cho, 2007). A strong absorption peak at 2080 cm^{-1} was corresponded to CN stretching absorption band of CN group in $\text{Fe}^{2+}\text{-CN-Fe}^{3+}$ of PB (Planche, Thiéblemont, Mazars, & Bidan, 1994; Ke Wang et al., 2015). There was no peak observed at 2168 cm^{-1} , which is attributed to $\text{Fe}^{2+}\text{-CN-Fe}^{3+}$ of Berlin green (Pajerowski, Watanabe, Yamamoto, & Einaga, 2011), revealing that PB instead of Berlin green was formed on the surface of the electrode. These results showed that the PPy-PB composite was successfully deposited on the surface of the electrode.

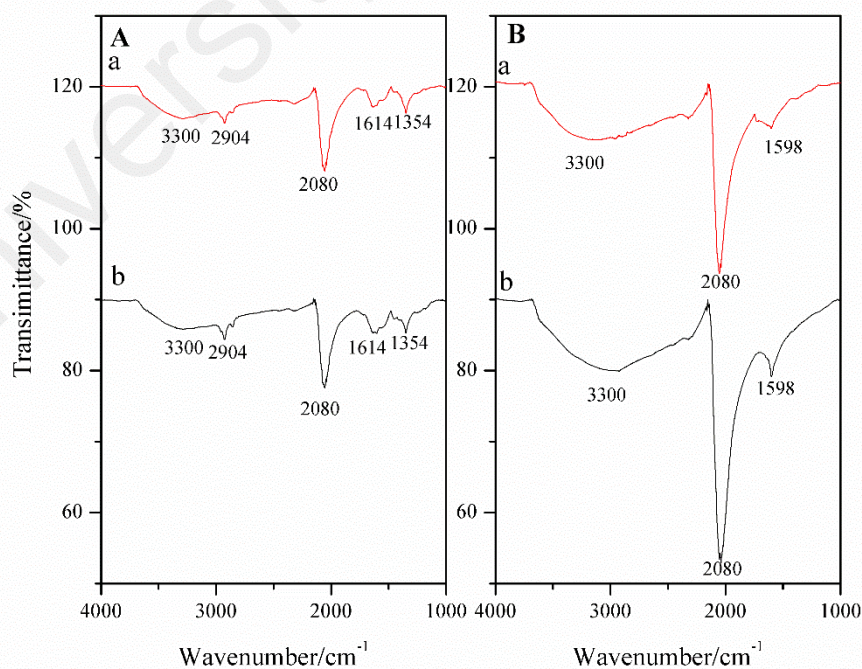


Figure 4.5: (A) FTIR spectra of (a) ED PB-PPy (10) and (b) ED PB-PPy (20). (B) FTIR spectra of (a) SA PB-PPy (10) and (b) SA PB-PPy (20).

4.1.3 Electrochemical behaviour of modified electrode

4.1.3.1 Cyclic voltammogram

It is well-known that PB is not stable in alkali solution due to the high affinity of OH^- ions react with Fe^{3+} ions which lead to the formation of $\text{Fe}(\text{OH})_3$ (Karyakin et al., 1999). To compare all of the modified electrodes even PB-PPy nanocomposites with the least PPy amount, as well as pristine PB, a slightly acidic electrolyte is selected. The acidity of the electrolyte should be not too low to ensure the practical electrochemical sensing application. Moreover, the CV current response of SA PB-PPy (10) increased dramatically from pH 3 to pH 4 and decreased in solution pH 5 as shown in **Figure 4.6**.

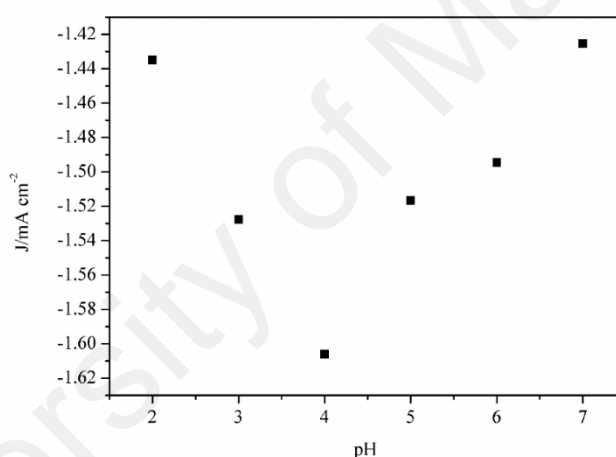


Figure 4.6: Current density response of SA PB-PPy (10) electrode vs. pH.

Besides that, there was almost the same in peak current after 50 cycles in pH 4 electrolyte (**Figure 4.7**). Hence, the electrolyte used was a 0.05 M citrate buffer solution (pH 4.00) with 0.10 M KNO_3 as the supporting electrolyte. This pH 4.00 electrolyte selected agrees with a previous study (Ojani et al., 2016).

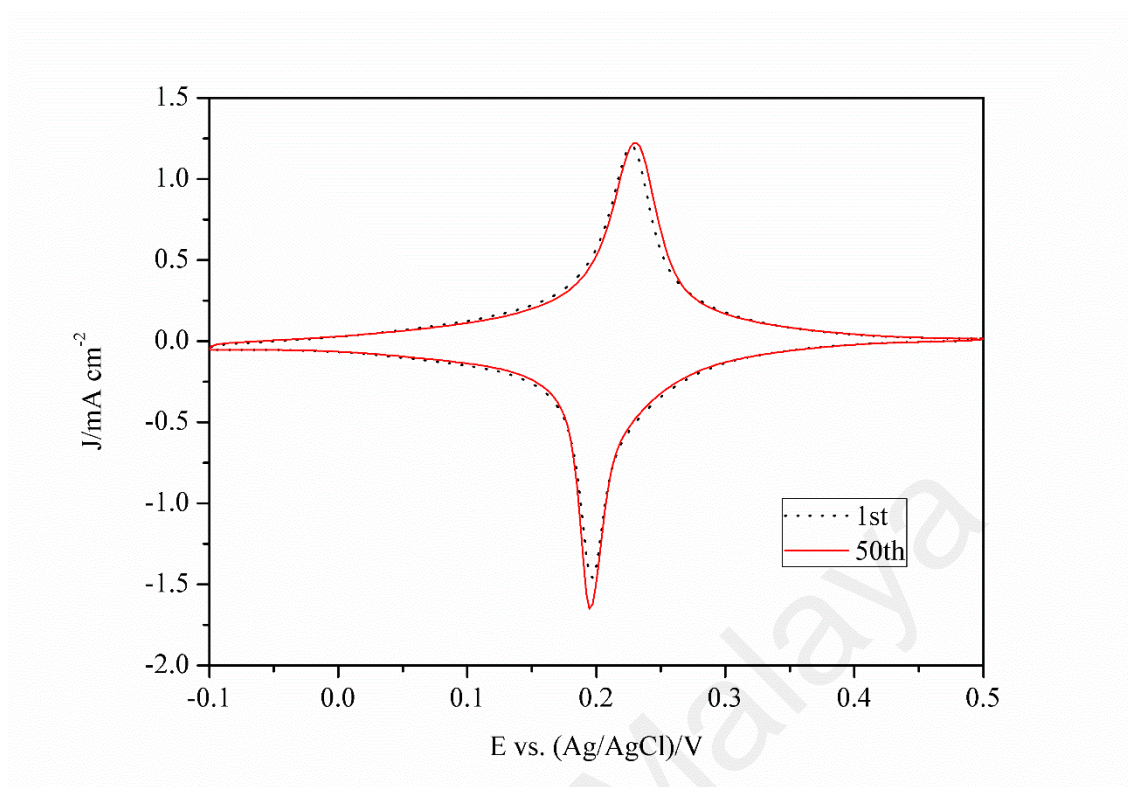


Figure 4.7: CV of 1st and 50th cycles of SA PB-PPy (10) in 0.05 M pH 4.00 citrate buffer with 0.10 M KNO₃. The scan rate is 50 mV s⁻¹.

Figure 4.8 illustrates the CV of PB-PPy self-assembled on the GCE surface with increasing number deposition cycle (NDC). As can be seen in **Figure 4.8**, there were two distinctive redox peaks in the CV curve, which are due to the conversion of PB into its reduced form, Prussian white (PW) and PW is re-oxidised to PB, respectively (Kong et al., 2015). On the other hand, there was no obvious redox peak corresponding to polypyrrole as its redox current was too low to be seen on bare carbon electrode (J. Wang, Xu, Yan, Zhu, & Wang, 2011) as compared with the high current of the nanostructured electrode material. As the NDC increased, the peak current increased, which can be related to the significantly higher amount of PB obtained under the presence of pyrrole which underwent oxidation and reduction of Fe (III) and thus the peak current was in proportional to the PB-PPy loading (Bellezza, Cipiciani, Costantino, & Elena Negozio, 2002).

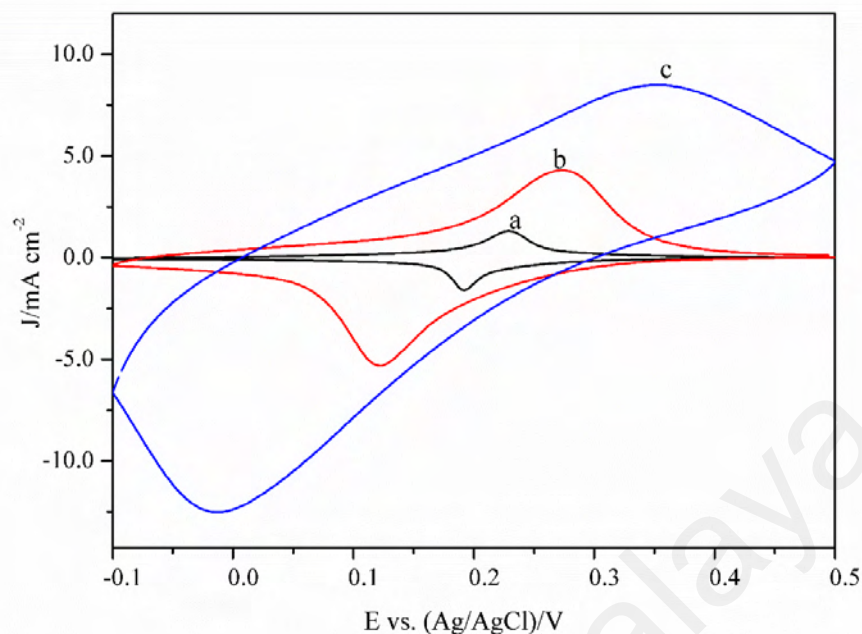


Figure 4.8: CV of SA PB-PPy with (a) 10 (b) 20 and (c) 30 NDC. The scan rate is 50 mV s^{-1} . The electrolyte used was 0.05 M pH 4.00 citrate buffer with 0.10 M KNO_3 .

Besides that, an increase of peak-to-peak separation (ΔE_p) was observed as a result of additional NDC of PB-PPy from curve **a** to **c**. As the two distinctive redox peaks corresponded to the redox process of Fe (II/III) of PB, the large peak separation was indicated the fact that the overpotential of the redox process of Fe (II/III) at SA PB-PPy electrode was greater and the electron transfer rate of Fe (II/III) was slower (Luo et al., 2015). This is presumably due to the increase in the amount of PPy, covering or forming a composite with PB and thus the rate of electron transfer between PB/electrolyte reduced. According to curve **b** of **Figure 4.8**, a voltammogram with much-improved current was observed when the NDC increases to 20 if compared to 10. Nevertheless, the PB-PW redox couple started to distort at 30 NDC as seen in curve **c** in **Figure 4.8**. This indicated that the thick film formed may inhibit the electron transfer of Fe (II/III) on the surface of the electrode (Y. Zhang et al., 2012).

Curve **a** and **b** in **Figure 4.9** show the CV of SA PB (10) and (20) which self-assembled on the electrode. The result proved that a very low amount of PB can be deposited on the electrode without the presence of the polymer albeit the same NDC was employed. The peak current of PB-PPy modified electrode was significantly higher than PB modified electrode, which was due to the synergistic effect of metal-polymer composite and the higher amount of PB formed in the presence of PPy was contributed by the oxidation of pyrrole and the reduction of Fe^{3+} .

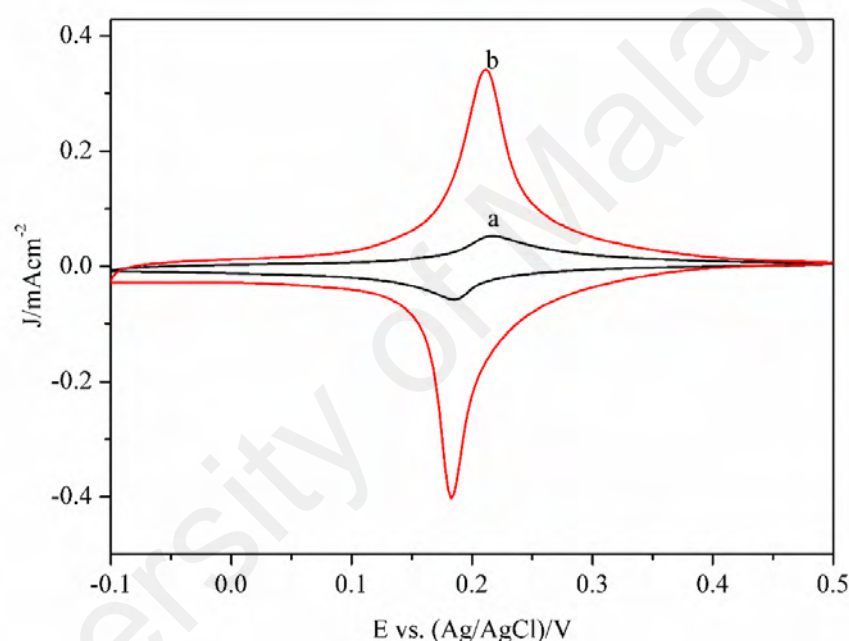


Figure 4.9: CV of (a) SA PB (10) and (b) SA PB (20). The scan rate is 50 mV s^{-1} . The electrolyte used was 0.05 M pH 4.00 citrate buffer with 0.10 M KNO_3 .

For comparison purpose, PB-PPy film was fabricated using a one-pot ED method from a single bath solution containing both monomer and the metal salt as displayed in **Figure 4.10**. The pulse deposition step was set to 10 (curve **a**) and 20 steps (curve **b**) in correspondence to the respective NDC in SA methods. As shown in **Figure 4.10**, the peak current increased with the number of deposition cycles. This revealed that the particle density grows with the number of deposition repetitions in pulse ED method. On the other

hand, PB-PPy electrodes were modified by the ED method seem to have two reduction peaks as shown in the CV in **Figure 4.10**. This special phenomenon will be explained further in the following part.

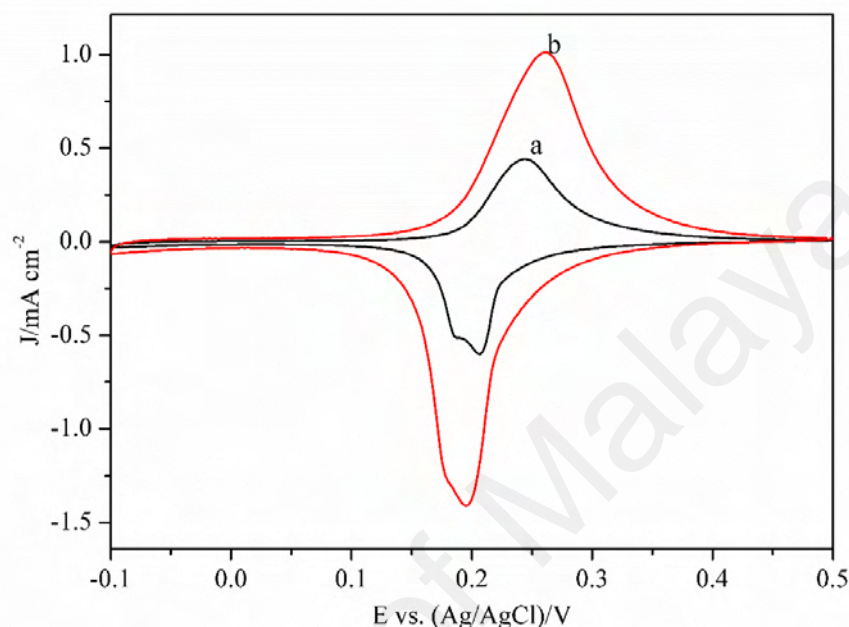


Figure 4.10: CV of electrodeposited PB-PPy electrodes with (a) 10 and (b) 20 repetitions. The scan rate is 50 mV s^{-1} . The electrolyte used was 0.05 M pH 4.00 citrate buffer with 0.10 M KNO_3 .

Figure 4.11 shows the CV of PB-PPy fabricated by SA (curve a) and ED (curve b) techniques. The PB-PPy electrode which showed the similar intensity of the redox peaks, prepared by SA and ED, respectively were chosen for the comparison study. Still, the peak currents of ED PB-PPy was slightly lower than SA PB-PPy and even the repetitions of ED were set to 20 while the NDC of SA PB-PPy was only 10 cycles. This may presumably due to some of the PPy and PB re-dissolved into the bath solution during the electrodeposition process as different potential were employed (Özkale et al., 2014). This phenomenon suggested that it was easier to prepare PB-PPy composites via self-assembly approach. Besides that, the redox couple peaks' width of electrode fabricated by one-pot ED was wider than the electrode modified by the SA method as displayed in **Figure 4.11**.

This was due to the facts that different electrochemical behaviours were exhibited by the PB-PPy synthesised by SA and ED techniques.

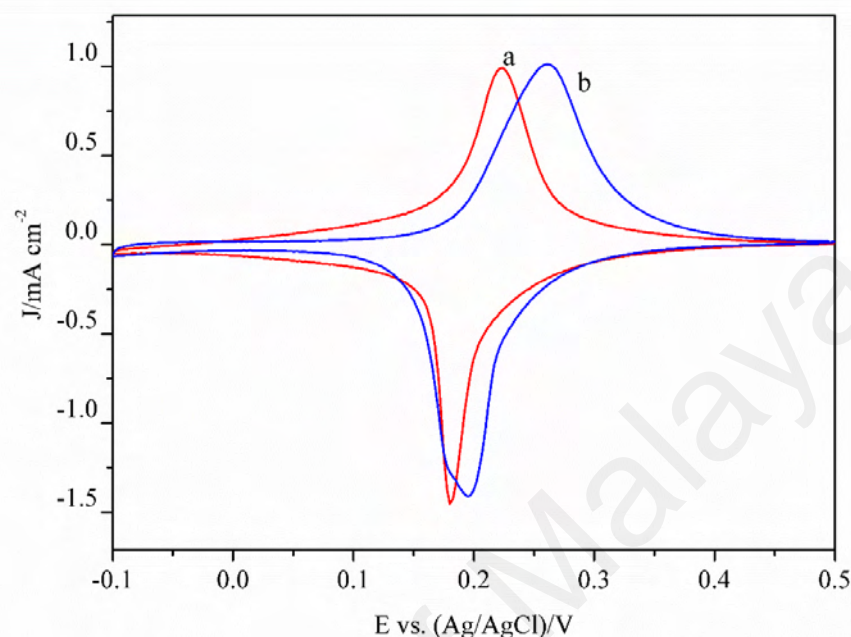


Figure 4.11: (a) CV of SA PB-PPy (10) (b) ED PB-PPy (20) in 0.05 M pH 4.00 citrate buffer with 0.01 M KNO₃ as supporting electrolyte at applied potential 0.50 to -0.10 V at 50 mV s⁻¹ scan rate.

According to the literature, common PB modified electrode usually had only one couple of voltammetric peaks at about 0.20 V vs. Ag/AgCl (sat. KCl) (Koncki, 2002). However, ED PB-PPy electrodes exhibited unconventional voltammetric behaviour as peaks splitting as seen in **Figure 4.11 and 4.12**. According to **Figure 4.12**, the intensities of these oxidation and reduction peaks varied with the increase of scan rate. **Figure 4.12 (A)** shows that the oxidation peak **a'** was higher than the oxidation peak **b'** when the scan rate was 1 mV s⁻¹. However, the order was reversed when the scan rates increased to 5 mV s⁻¹ as seen in **Figure 4.12 (B)**. The same phenomenon was observed for reduction peaks **a** and **b** as displayed in **Figure 4.12 (C)** and **(D)**. This indicated that the current peak **b** was directly proportional to the scan rate, suggesting that the electrochemical property of peak **b** was a surface-controlled process (Y. Zhang et al., 2012). Hence, peak

b could be attributed to the redox reaction of the surface atoms whereas, peak **a** could be ascribed to the redox reaction of the inner atoms of the nanoparticles (S. Q. Liu et al., 2002). These trends validated that the electrochemical behaviour of the PB nanoparticles synthesised by ED was different from PB prepared by the SA method. This was also depicted by the distinct morphologies observed in FESEM images of PB synthesised by ED and SA methods, respectively.

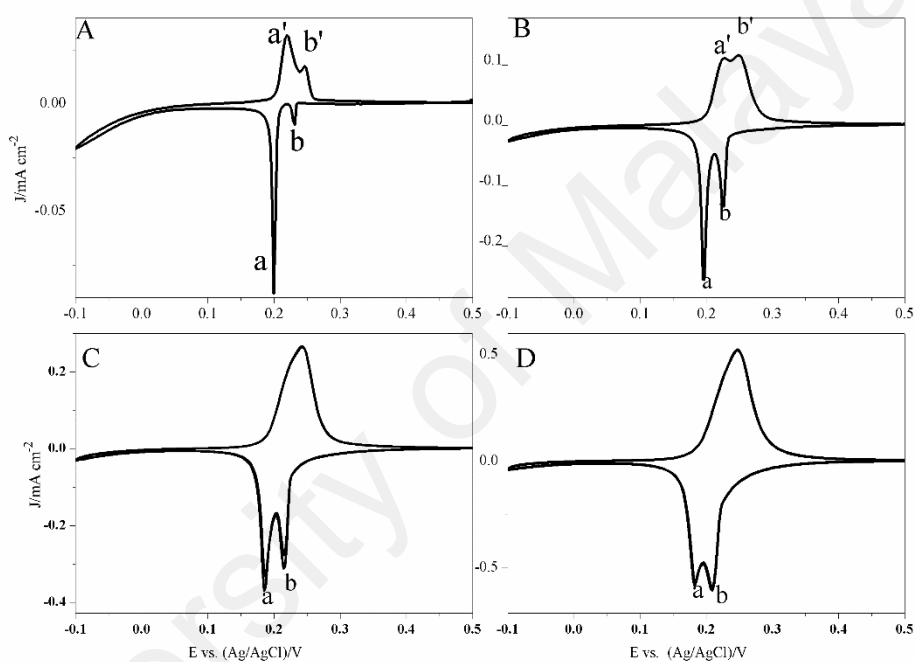


Figure 4.12: CV of ED PB-PPy (20) in 0.05 M pH 4.00 citrate buffer with 0.10 M KNO_3 as supporting electrolyte in different scan rate; (A) 1 (B) 5 (C) 10 (D) 20 mV s^{-1} .

As shown in **Figure 4.13**, the cathodic and anodic peak currents of SA PB-PPy (10) and ED PB-PPy (20) have been plotted against their respective scan rates, in order to understand the charge transport characteristics within reaction layer. The redox couple observed in **Figure 4.13** was due to the redox behaviour in which PB is reduced to Prussian white (PW) and is re-oxidised to PB.

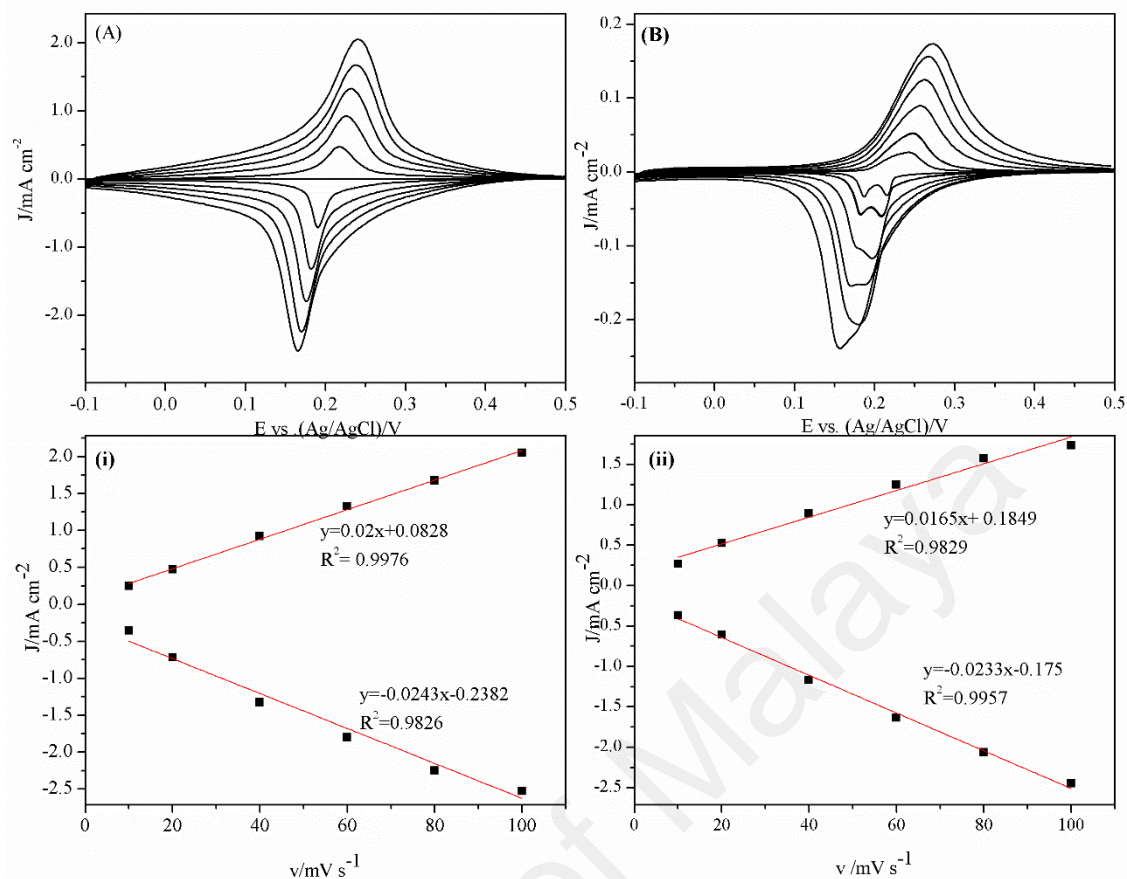


Figure 4.13: (A) CV of the SA PB-PPy (10) in 0.05 M pH 4.00 citrate buffer with 0.10 M KNO_3 as supporting electrolyte at various scan rate (from inner to outer curve); 10, 20, 40, 60, 80 and 100 $mV\ s^{-1}$. (i) Plot of peak current vs. scan rate for SA PB-PPy (10). (B) CV of the ED PB-PPy (20) in 0.05 M pH 4.00 citrate buffer with 0.10 M KNO_3 as supporting electrolyte at various scan rate (from inner to outer curve); 10, 20, 40, 60, 80 and 100 $mV\ s^{-1}$. (ii) Plot of peak current vs. scan rate for ED PB-PPy (20).

The linear relationship as observed in **Figure 4.13 (i) and (ii)** (from 10 $mV\ s^{-1}$ to 100 $mV\ s^{-1}$) validated the electrochemical behaviour of the PB in PB-PPy composite film as a reversible and surface-confined process (Bai & Shiu, 2015). The peak-to-peak separation of redox couple of PB to PW was approximately 10 mV at the scan rate of 10 $mV\ s^{-1}$. Hence, ideal Nernstian behaviour is approached for a relatively slow scan rate in this study, which is a normal phenomenon in practice, demonstrating the reversibility of the redox reaction on the electron surface (J. Wang, 2006a).

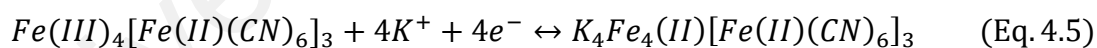
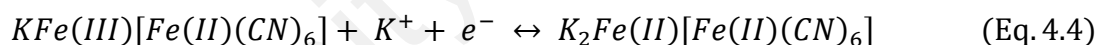
4.1.3.2 Surface coverage and estimated thickness of PB-PPy film

From a reversible surface reaction, the peak current is related to the surface concentration of the electroactive mediator (Γ), by the following equation;

$$I_p = \frac{n^2 F^2 \nu A \Gamma}{4RT} \quad (\text{Eq. 4.3})$$

where n is number of electron, F is the Faraday constant ($96,485 \text{ C mol}^{-1}$), ν is the potential sweep rate, A is the surface geometrical electrode (0.07 cm^2), Γ (mol cm^{-2}) is the surface coverage and R is the gas constant ($8.314 \text{ J K}^{-1} \text{ mol}^{-1}$) and T is the temperature at 298 K (J. Wang, 2006a).

By using the slope I_{pc} vs. scan rate, since the reduction of H_2O_2 depends on the reduction peak, the surface coverage (quantitative amount) of PB-PPy was calculated (**Table 4.1**). PB is known to exist in both soluble and insoluble forms, according to the following reactions;



The reduction procedure has been reported to lead to the incorporation of cations into the electrode regardless of whether the soluble (Eq. 4.4) or insoluble PB (Eq. 4.5) forms are involved (Kong et al., 2015). The Eq. 4.4 was selected in this case as the value of calculated surface coverage and the thickness was more reasonable. The polypyrrole was assumed to form a hybrid/composite with PB and in correspondence to the amount of PB.

In addition, the thickness of the studied layers was estimated from the following equations,

$$\Gamma = \frac{Q}{nFA} \quad (\text{Eq. 4.6})$$

where Q is the quantity of charge consumed during the reduction of the adsorbed layer (J. Wang, 2006a),

$$m = \frac{QM}{Fn} \quad (\text{Eq. 4.7})$$

where M is the molar mass of Prussian blue (Iftikhar et al., 2011), and

$$D = \frac{m}{AL} \quad (\text{Eq. 4.8})$$

where D is the density and L is thickness (Iftikhar et al., 2011).

Table 4.1: The calculated surface coverage and thickness of PB-PPy.

Modified electrode	Surface coverage (mol cm ⁻²)	Thickness (μm)
ED PB-PPy (10)	5.75E-09	9.76E-03
ED PB-PPy (20)	2.49E-08	4.25E-02
SA PB-PPy (10)	2.58E-08	4.39E-02
SA PB-PPy (20)	4.47E-08	7.47E-02

The calculated thickness was in an agreement with the estimated thickness from the highlighted cross-sectional FESEM images in **Figure 4.2**, which both values were less than 1 μm.

4.1.3.3 Electrochemical impedance spectroscopy

The electrochemical properties of the modified electrodes were further investigated by electrochemical impedance spectroscopy (EIS) measurements. EIS measurements were conducted in a frequency range of 10 Hz to 0.1 kHz with an AC voltage amplitude of 5 mV at the open circuit potential (OCP). A 0.05 M citrate buffer solution (pH 4.00) with 0.10 M KNO₃ was used as supporting electrolyte.

Figure 4.14 shows the Nyquist plot of PB-PPy electrode modified by pulse ED and SA methods. These Nyquist plots were interpreted by fitting the experimental data with an equivalent circuit using NOVA 1.11 software. The corresponding data is tabulated in **Table 4.2**. The simplest Randles equivalent circuit model as shown in the inset (A) of **Figure 4.14** was used in the fitting of all electrodes, except for SA PB-PPy (20), from the experiment data of the curves **a**, **b** and **c** in **Figure 4.14**, the Randles model $R_s[Q(R_{ct}, W)]$ consists of ohmic resistance of the solution (R_s), constant phase element (Q) and charge transfer resistance (R_{ct}) which is the resistance of layer, indicating the electron transfer kinetics of the redox probe at the electrode interface and consequently, showing conductivity of the sample. For the fitting of SA PB-PPy (20), the Warburg element, W, and hyperbolic tangent, T, were added in the equivalent circuit in order to describe the semi-infinite diffusion and finite diffusion, respectively, at low frequency (Azman, Lim, & Sulaiman, 2016). These elements selection were due to a straight line at an angle of almost 45° (Warburg resistance) and another straight line which was almost parallel to the imaginary axis/y-axis (hyperbolic tangent) of the Nyquist plot that were observed in the low frequency region (Oraon, De Adhikari, Tiwari, Bhattacharyya, & Chandra Nayak, 2016), as shown in curve **d** of **Figure 4.14**. Term B is associated with hyperbolic tangent, T in NOVA 1.11, which is the factor related to thickness of the diffusion layer. Its equivalent circuit is demonstrated in the inset (B) of **Figure 4.14**.

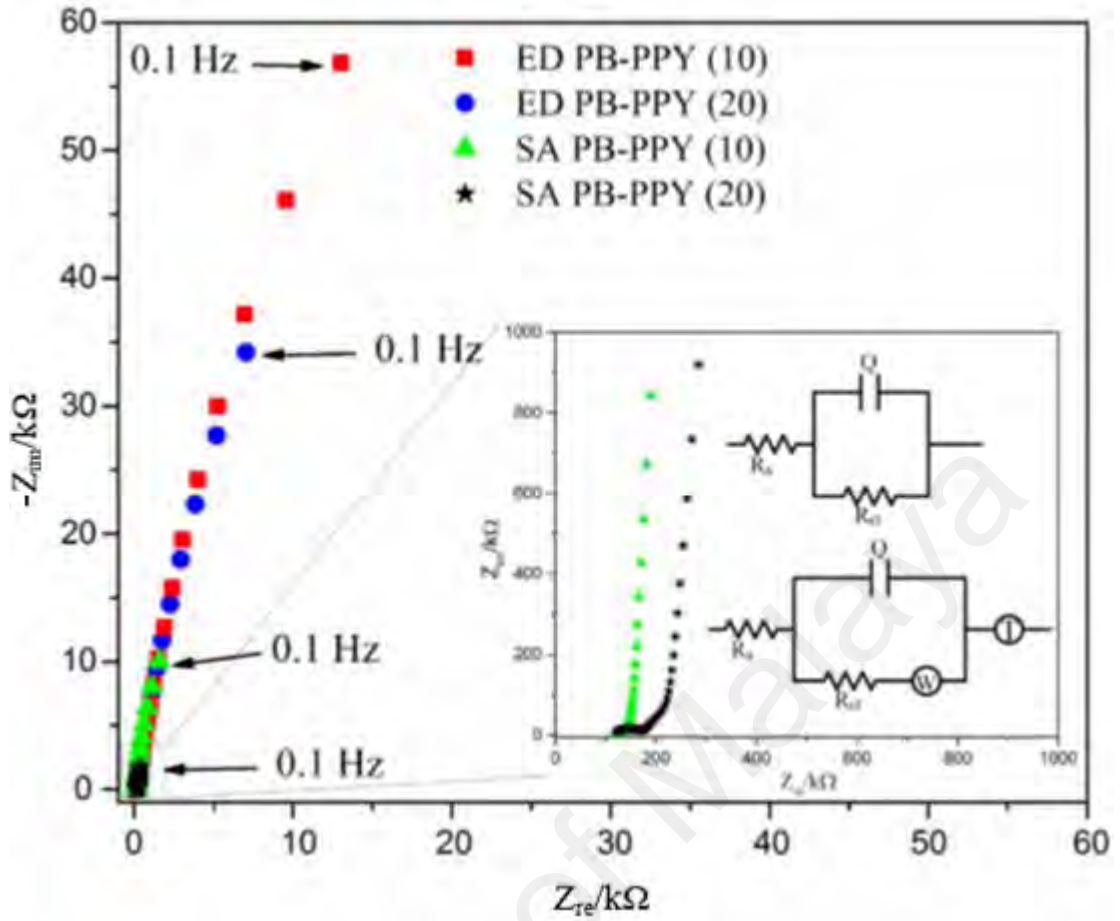


Figure 4.14: Nyquist plot of ED PB-PPy (10), ED PB-PPy (20), SA PB-PPy (10) and SA PB-PPy (20). Inset: Equivalent circuit. The electrolyte used was 0.05 M pH 4.00 citrate buffer with 0.10 M KNO₃ as supporting electrolyte.

To achieve an acceptable correlation between the experimental and simulated data, a pure capacitor (C) was replaced by a constant phase element (CPE) in the fitting procedure. The impedance of CPE is defined as

$$Z_{CPE} = \frac{1}{Q(j\omega)^n} \quad (\text{Eq. 4.9})$$

where ω is the pulsation, Q is the combination of the surface and the electroactive properties of species which is independent of frequency and n are achieved from the Bode plot (slope of $\log |Z|$ vs. $\log f$). The relation of Q can be written as

$$Q = \frac{C_{dl}^n}{R_s^{(1-n)}} \quad (\text{Eq. 4.10})$$

As can be seen from **Figure 4.14**, at the higher frequencies, modified electrodes showed resistance behaviour. For SA PB-PPy (20), at lower frequencies, due to capacitive behaviour, there was a sharp increase in the imaginary part of the impedance and the curve shows a vertical line (Oraon et al., 2016; W. Wang & Wu, 2017) in the curve **d**, **Figure 4.14**. This condition can be predicted as transition-metal hexacyanoferrates (PB) with the combination of conducting polymers (PPy) which has been widely used for the construction of supercapacitor (Ghasemi, Hosseini, & Asen, 2015; Luo et al., 2015)

Figure 4.15 represents the evolution of (C') (the real part of the capacitance) vs. frequency for all modified electrodes. For SA PB-PPy (20), by decreasing the frequency, C' has sharply increased, showing less frequency dependent which the electrode structure and the electrode/electrolyte interface characteristic is. On the other hand, at higher values, the capacitance is strongly depending on the frequency.

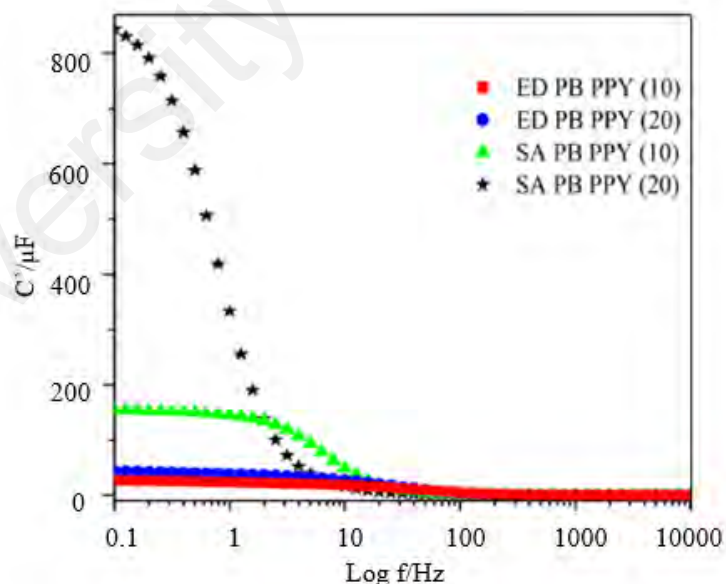


Figure 4.15: Evolution of the real part vs. frequency of ED PB-PPy (10), ED PB-PPy (20), SA PB-PPy (10) and SA PB-PPy (20). Electrolyte used was 0.05 M pH 4.00 citrate buffer with 0.10 M KNO₃ as supporting electrolyte.

For all spectra, some characteristic frequencies are given in **Figure 4.16** which depicts the change of C'' (the imaginary part of the capacitance) vs. frequency. The plot for SA PB-PPy (20) shows its maximum at a frequency f_0 , defining a time constant as $\tau_0 = 1/f_0 = 1.25$ s, which is related to dielectric relaxation time, as the characteristic of the whole system, where the transition between resistive and capacitive conduction occurs from high frequency to low frequency (Lvovich, 2012). The obtained relaxation time is in good agreement with the supercapacitor characteristic described in the literature (Taberna, Simon, & Fauvarque, 2003)

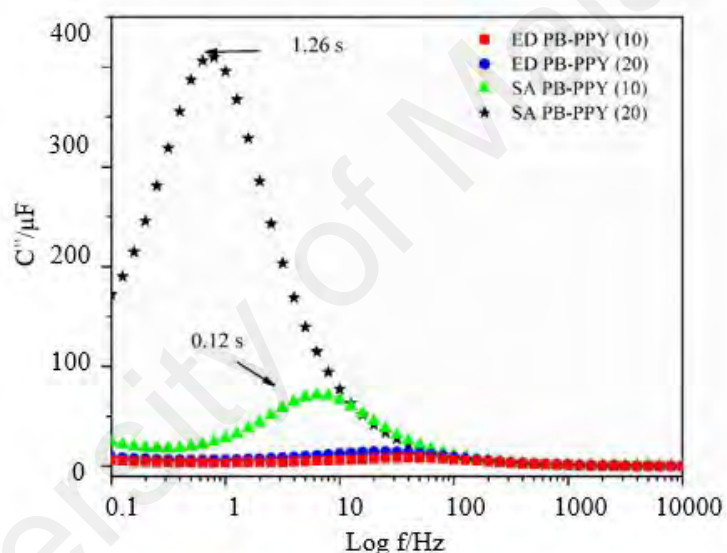


Figure 4.16: Evolution of imaginary capacitance vs. frequency of ED PB-PPy (10), ED PB-PPy (20), SA PB-PPy (10) and SA PB-PPy (20). Electrolyte used was 0.05 M pH 4.00 citrate buffer with 0.10 M KNO_3 as supporting electrolyte.

From **Table 4.2**, the R_{ct} of the electrode was arranged in the following orders: (R_{ct}): ED PB-PPy (10) > ED PB-PPy (20) > SA PB-PPy (10) > SA PB-PPy (20). The R_{ct} of ED PB-PPy electrode decreased by increasing the number of electrodeposition cycle.

Table 4.2: Electrochemical parameters obtained by fitting of EIS results.

	$R_s(\Omega)$	$R_{ct} (k\Omega)$	$Q(\mu Mho)$	N	W(mMho)	T (mMho)	B
ED PB-PPy (10)	173	448	26.2	0.939	-	-	-
ED PB-PPy (20)	153	312	43.9	0.939	-	-	-
SA PB-PPy (10)	138	91.2	155	0.978	-	-	-
SA PB-PPy (20)	113	0.05	23.9	0.633	7.69	3.05	0.316

The SA PB-PPy (20) electrode has the lowest R_{ct} value, which can be associated to a remarkably high CV current of this modified electrode as mentioned in **Section 4.1.3.1** and thus revealing the high conductivity and low internal resistance of the SA PB-PPy (20) electrode. This is presumably due to the increasing amount of the deposited conducting polymers on the electrode as only nuclei of polypyrrole was deposited on the surface of the electrode for SA PB-PPy (10). The finding agrees with the FESEM images obtained above, where the amount of PB-PPy loaded is increased with the electrodeposition repetitions which attributed to the overlapping of polypyrrole together with the formation of new polymer nuclei, thus increasing the linkages network of these PPy.

Figure 4.17 shows that the phase plot agrees with the results obtained from the Nyquist plot. The phase angle would be near 80° at high frequencies if the resistance of the surface increases (Y. W. Park, 2010). Thus, the modified electrode with highest R_{ct} is ED PB-PPy (10), followed by ED PB-PPy (20), SA PB-PPy (10), which also supports the R_{ct} obtained from the equivalent circuit.

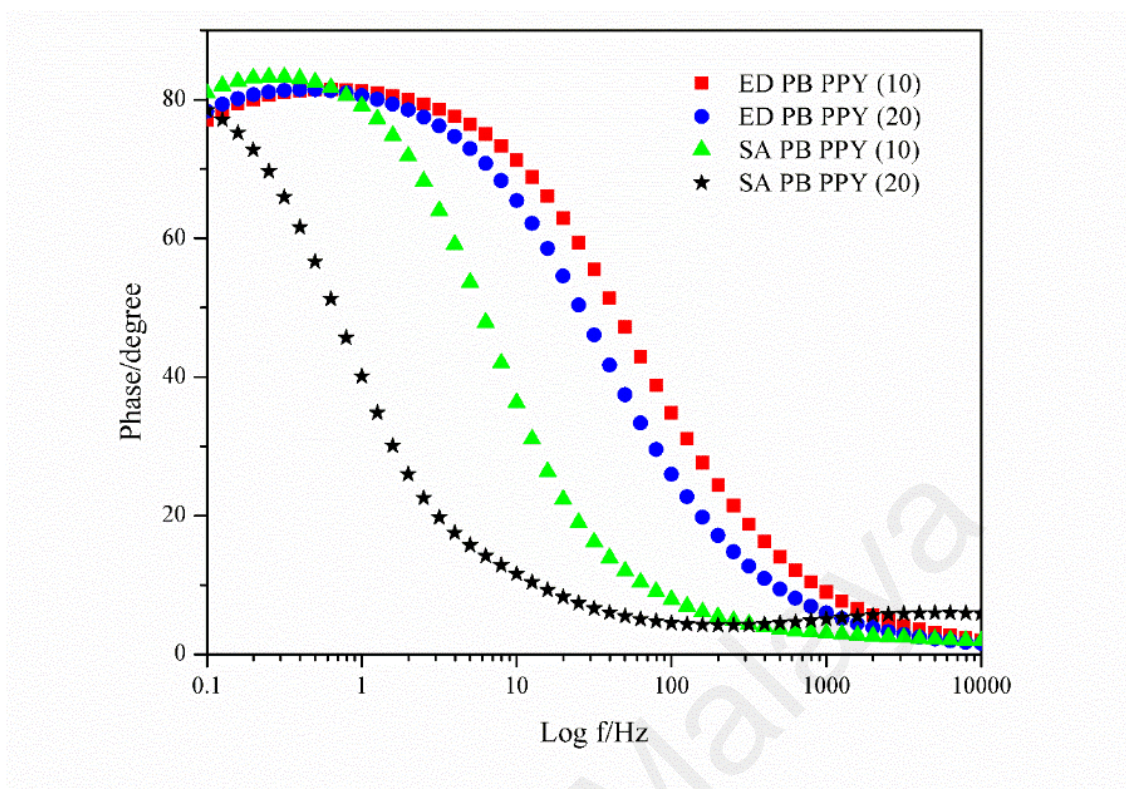


Figure 4.17: Bode phase of ED PB-PPy (10), ED PB-PPy (20), SA PB-PPy (10) and SA PB-PPy (20). Electrolyte used is 0.05 M pH 4.00 citrate buffer with 0.10 M KNO₃ as supporting electrolyte.

The nucleation of the polymer can be divided into a few stages (Hwang, Santhanam, & Lin, 2001). Firstly, nuclei of the polypyrrole were formed on a bare surface substrate once pyrrole was oxidized. Following from there, the nuclei grew on its former position until it overlapping with/or additional formation of new nuclei due to more polypyrrole was deposited on the substrate. Finally, the surface was fully covered by a layer of polypyrrole film. Hence, the first stage can be related to SA PB-PPy (10), where only the nuclei of polypyrrole was formed on the surface as shown in FESEM image of SA PB-PPy (10) (**Figure 4.2(C)**). Next, multiple polypyrrole nuclei grew on its former position, overlapped with each other together with the new nuclei formed when the deposition cycle increase to 20. This overlapping/linkage of the polymer was clearly shown in the FESEM image of SA PB-PPy 20 (**Figure 4.2 (D)**).

To further support the findings, EIS experiment for SA PB-PPy (30) was performed, which indicates the surface was covered by a layer of thicker polypyrrole film. The EIS data of SA PB-PPy (30) revealed that the surface was covered by an increasing amount of polypyrrole film. This is due to the effect of conducting polymer was more noticeable in SA PB-PPy (30) as a typical impedance response of electroactive polymer in solution-polymer metal systems as shown in **Figure 4.18** (Lvovich, 2012). This EIS spectra of SA PB-PPy (30) can be explained as follows:

- A high impedance response to charges carriers in bulk polymer denoted by a parallel combination film of film resistance R_{bulk} and capacitance (Q_{bulk}) in series with uncompensated solution resistance R_{sol} .
- Another parallel combination of charge-transfer resistance R_{ct} and double layer
 - i. capacitive Q_{dl} features at medium frequency representing the electrode-polymer
 - ii. interface (electron transfer) and polymer-solution interface (counter-ion transfer)
- The original supercapacitive -90° line observed in SA PB-PPy (20) was gradually substituted by a partially capacitive resistive transmission-line model, with slopes different from an ideal -90° in that case with the deactivation of the metal film (SA PB-PPy (30)).
- This transmission line at low frequency indicating pseudocapacitive charging of the film.

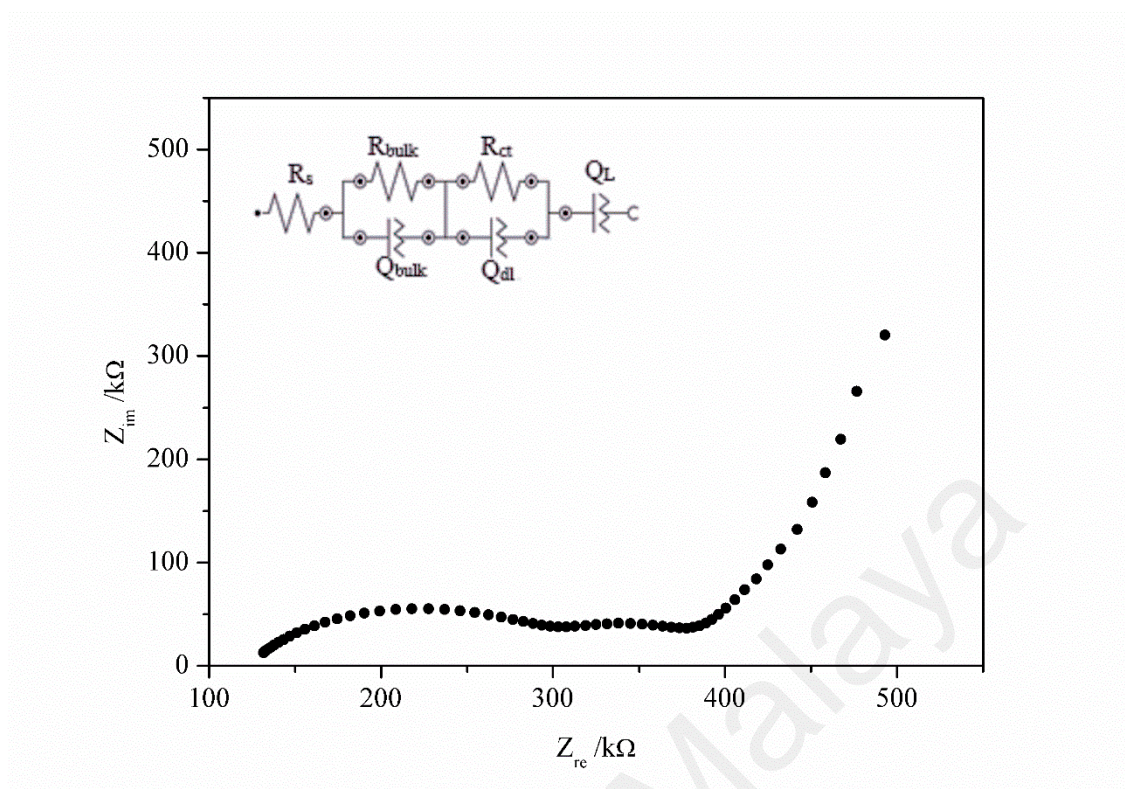


Figure 4.18: Nyquist plot of SA PB-PPy (30). Inset: Equivalent circuit. Electrolyte used was 0.05 M pH 4.00 citrate buffer with 0.10 M KNO_3 as supporting electrolyte.

The bode phase of SA-PB-PPy as shown in **Figure 4.19** supported the equivalent circuit selected (inset of **Figure 4.18**) due to two semicircle features were observed in the bode phase. The value of parameters fitted was as shown in **Table 4.3**.

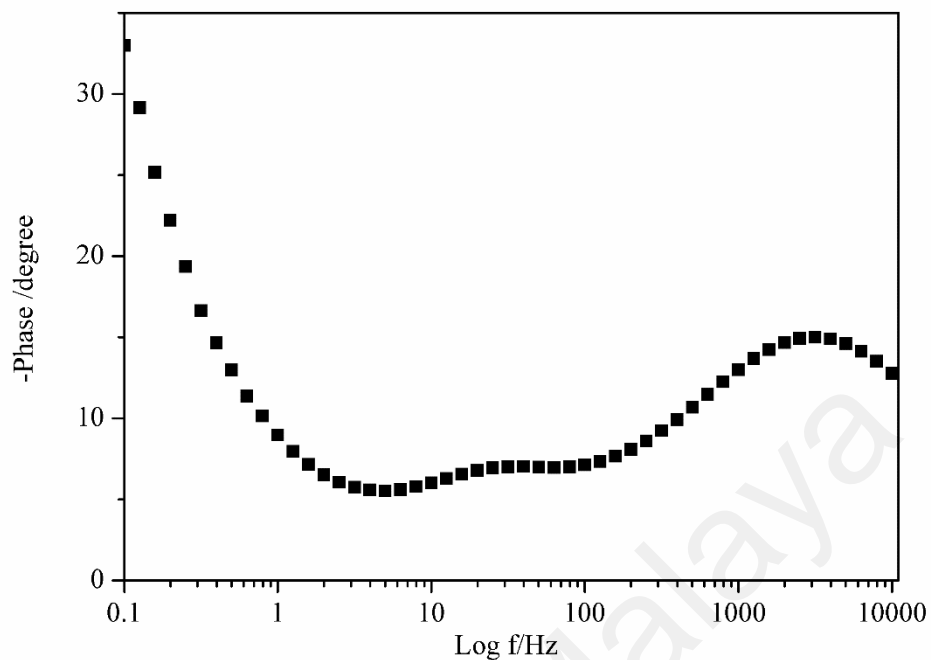


Figure 4.19: Bode phase of SA PB-PPy (30). Electrolyte used is 0.05 M pH 4.00 citrate buffer with 0.10 M KNO₃ as supporting electrolyte.

Table 4.3: Electrochemical parameters of SA PB-PPy (30) obtained by fitting of EIS results.

Element	Value
R _s (Ω)	123
R _{bulk} (Ω)	184
Q _{bulk} (μMhO)	12.6
N	0.655
R _{ct} (Ω)	87
Q _{dl} (μMhO)	380
N	0.726
Q _L (mMHO)	430
N	0.788

Hence, SA PB-PPy electrode had a lower R_{ct} than ED PB-PPy electrode, demonstrating an enhanced electroactivity.

4.1.4 Electrochemical sensing of H₂O₂

Figure 4.20 presents the CV of SA and ED PB-PPy electrodes toward the electrocatalytic reduction of H₂O₂ in 0.05 M citrate buffer (pH 4.00) with 0.10 M KNO₃ as the supporting electrolyte. Similar to PB, the voltammetric peak for H₂O₂ reduction at prepared PB-PPy nanocomposites started at the potential where the reduction of PB occurs (Derwinska et al., 2003). The CV reduction current enhanced in the presence of H₂O₂ (curve **b**), which is, in contrast, to curve **a** in the absence of H₂O₂. As indicated in **Figure 4.20 (A)**, the peak-to-peak separation of ED PB-PPy electrode increased, as compared to the SA PB-PPy (10) electrode as shown in **Figure 4.21 (B)**, which demonstrated the decreases of electron-transfer rate. Moreover, the oxidation peak of ED PB-PPy decreased to a greater extent than SA PB-PPy electrode during the sensing of H₂O₂, indicated that it was not as stable as PB-PPy which was prepared by the SA method.

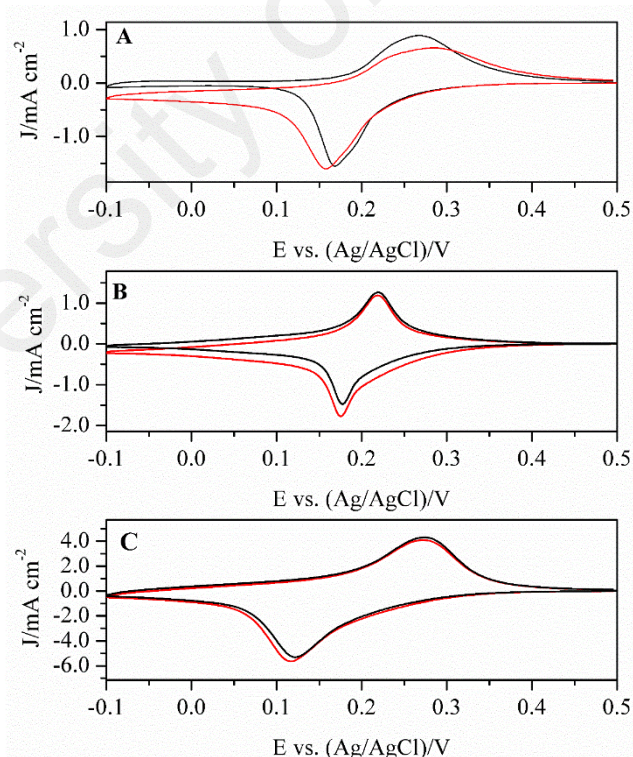


Figure 4.20: CV of (A) ED PB-PPy (20), (B) SA PB-PPy (10) and (C) SA PB-PPy (20) modified electrode in the absence (a) and the presence of 1 mM H₂O₂ (b) in 0.05 M pH 4.00 citrate buffer with 0.10 M KNO₃ as supporting electrolyte.

On the other hand, for SA PB-PPy electrode, 20 NDC was too thick for the SA PB-PPy electrode, thus it induced a decrease in sensitivity towards H₂O₂ according to **Figure 4.20 (C)**. The phenomenon which could be attributed to the electron transfer of Fe (II/III) was impeded and the diffusion of H₂O₂ was blocked with the increasing film deposition cycles. Thus, SA PB-PPy (10) displayed an enhanced electrocatalytic reduction towards H₂O₂.

As can be seen in **Figure 4.21 (A)**, the cathodic peak current of SA PB-PPy (10) electrode is increased and the anodic current is decreased, whereas the cathodic peak current is proportional to the H₂O₂ concentration. This obviously pointed out its electrocatalytic reduction behaviour (Razmi, Mohammad-Rezaei, & Heidari, 2009). Therefore, the PB-PPy electrode prepared by the SA method was a better potential electrode for the sensing of H₂O₂ if compared to the electrode synthesised via the ED method, owing to its simplicity and advanced electrocatalytic effect. The detection of H₂O₂ was repeated for three times and the RSD for each measurement did not exceed 5% as shown in **Figure 4.21 (B)**. The linear equation was $J \text{ (mA cm}^{-2}\text{)} = -0.3847 \text{ (mA mM}^{-1}\text{cm}^{-2}\text{)} - 1.374$ and the $R_2 = 0.991$.

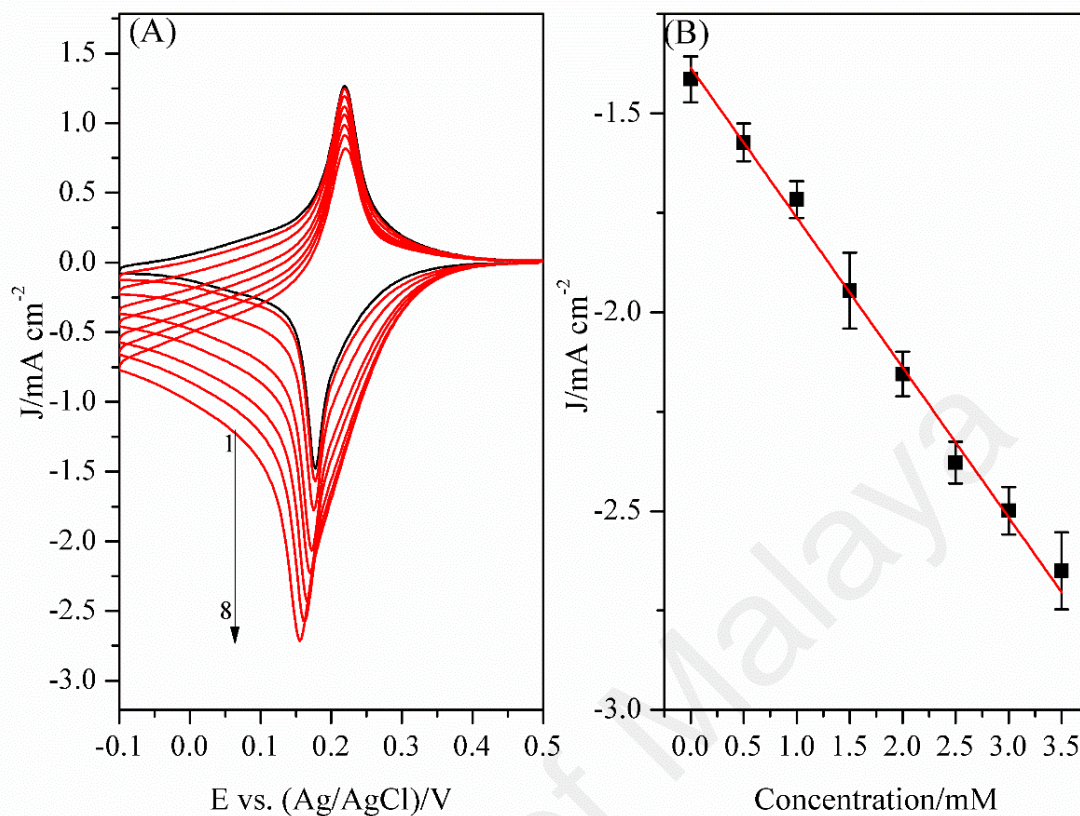


Figure 4.21: (A) CV of the SA PB-PPy (10) in 0.05 M pH 4.00 citrate buffer with 0.10 M KNO_3 as supporting electrolyte at various concentration of H_2O_2 (1–8): 0, 0.5, 1, 1.5, 2, 2.5, 3 and 3.5 mM, potential scan rate: 50 mV s^{-1} . (B) The plot of catalytic peak current vs. H_2O_2 concentration.

4.1.4.1 Interference study

To study the anti-interference ability on the optimum PB-PPy modified electrode-SA PB-PPy (10), the influence of some common electrochemical interfering species (glucose, fructose, ascorbic acid and uric acid) to the current response of 1 mM H₂O₂ was investigated. The current responses were generated due to the fact that these interfering species were negligible, indicating high selectivity of the sensor as seen in **Figure 4.22**.

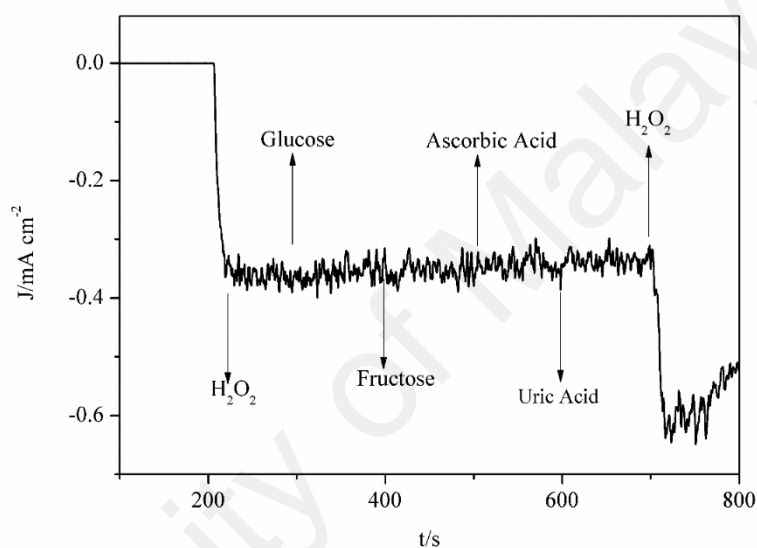


Figure 4.22: SA PB-PPy (10) electrode response to H₂O₂ (1 mM) and glucose, fructose, ascorbic acid and uric acid as interfering compounds (1 mM) in 0.05 M pH 4 citrate buffer with 0.10 M KNO₃ as supporting electrolyte Applied potential: 0.10 V vs. (Ag/AgCl)/V.

4.1.4.2 Comparison with other work

A comparison of the electrochemical performance of the SA PB-PPy electrode with previous reported PB-modified sensors is listed in **Table 4.4**. The sensitivity of SA PB-PPy modified electrode is considerably higher compared to other PB based H₂O₂ electrochemical sensors.

Table 4.4: Comparison of several PB-based H₂O₂ electrochemical sensors.

Modified electrode	Analysis method	Sensitivity (mA M ⁻¹ cm ⁻²)	Ref.
Chemical deposition PB on glassy carbon paste	Amperometry	188	Ricci, Amine, Moscone, & Palleschi, (2003)
PPy/PB nano electrodeposited under ultrasound conditions	Cyclic voltammetry	5.4	Hostert et al. (2016)
PB electroless self-assembled on carbon ceramic electrode	Cyclic voltammetry	232	Razmi et al. (2009)
GCE modified by graphene/PB composite nanosheets by casting the active material with Nafion [®] solution	Amperometry	2.2	Roig, Navarro, Garcia, & Vicente, (1994)
Electrodeposition of PB NPs on Polyaniline coated halloysite nanotube	Amperometry	0.98	Sheng et al. (2015)
Self-assembled PB-PPy on GCE	Cyclic voltammetry	384.7	This work

4.2 Self-assembly of PB analogue-CuHCF-PPy nanocomposite as nicotine electrochemical sensor

SA approach can precisely control the thickness of the nanocomposites and consequently its sensitivity towards analyte and its electrochemical behaviours, as well as can achieve in-situ modification of the electrode. Taking the account of the low-cost, simplicity and the ability to simultaneously formation of two components, the direct SA technique has become one of the most promising technique to produce MeHCF films (Chu et al., 2017).

Apart of PB, its analogues such as copper (Gonales et al., 2011; Gonçalves et al., 2013; Oliveira et al., 2018), cobalt (Damiri, Oskoei, & Fouladgar, 2016) and nickel hexacyanoferrate (Z.Wang et al., 2012), have been extensively evaluated in the development of electrochemical sensors for various analytes. It is expected that the same synthesis method to prepare PB can be used to produce PB analogues due to the similar reaction between the metal cation and metal cyanide anion for synthesis. Hence, it is interesting to investigate whether other PB analogues-conducting PPy nanocomposites can be formed by a similar method for sensing usage. Among the metal substituted analogues of Prussian blue, copper hexacyanoferrate (CuHCF) is considered here for the following reasons: CuHCF, an open framework material with the Prussian blue crystal structure was selected for this purpose as it is negatively charged and water-dispersible, hence, compatible with the layer-by-layer (LBL) SA approach (Nyström et al., 2015). Besides that, the potential of the redox couple of CuHCF located at approximately +0.7 V vs. Ag/AgCl (sat. KCl), which is close to the palladium hexacyanoferrate (PdHCF) composites that previously employed for nicotine sensing (C. Y. Yang et al., 2016). Hence, CuHCF can be a cheaper alternative for electrochemical detection of nicotine. In addition, rGO was used as a support layer for CuHCF-PPy, permitting the preparation of nanocomposites with high stability for the development of electrochemical sensors.

4.2.1 Electrodeposition of rGO as substrate

In this current work, CuHCF-PPy film was deposited on the reduced graphene oxide (rGO) surface via electrochemical reduction by scanning repetitively the GCE in GO solution. The easiest, a fastest and most environmentally friendly method to reduce GO is via this method (Golsheikh, Huang, Lim, Zakaria, & Yin, 2013). To examine the charge transfer properties of the rGO electrode, the redox probe $\text{Fe}(\text{CN})_6^{3-/4-}$ was used as it is sensitive to surface chemistry of carbon-based electrodes (P. Chen, Fryling, & McCreery, 1995). The increased current response of GO/GCE in redox probe solution demonstrating the enhanced electrochemical active sites by ED surface alteration. Overall there is no saturation of peak current for the ED cycles from 1 to 15, but initially, the peak-to-peak separation (ΔE_p) was decreased at first 10 scanning cycles, and when the cycles increased from 10 to 15, the separation becomes slightly higher as shown in **Figure 4.23**. The value of ΔE_p was tabulated in **Table 4.5**.

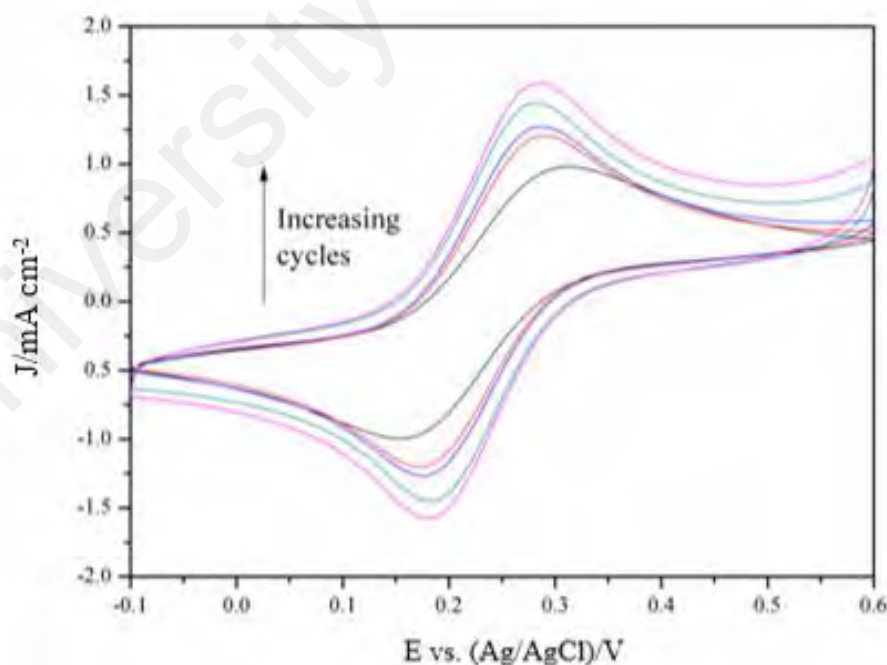


Figure 4.23: rGO/GCE with different deposition cycle (from 1 to 15 cycles) in 5 mM $\text{Fe}(\text{CN})_6^{3-/4-}$ with 0.1 M KCl as supporting electrolyte. Scan rate: 50 mV s^{-1} .

Table 4.5: Peak-to-peak separation (ΔE_p) of $[\text{Fe}(\text{CN})_6]^{3-/4-}$ for different layers of rGO.

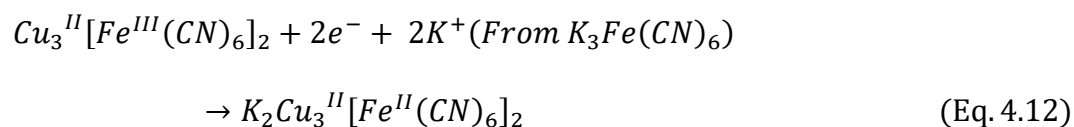
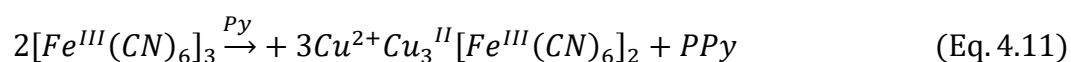
Layers of rGO electrodeposited	ΔE_p (mV)
1	157.69
3	117.19
5	109.87
10	97.65
15	104.98

This increase in the ΔE_p is caused by delay in electron transfer rate. Thus, the optimal electrodeposition cycles were selected as 10 cycles as ΔE_p become wider after that.

4.2.2 Mechanism of formation of CuHCF-PPy nanocomposite

In the formation of CuHCF-PPy nanocomposites, the Cu^{2+} was reacted with the $\text{Fe}^{\text{III}}(\text{CN})_6^{3-}$ to produce $\text{Cu}^{\text{II}}-\text{N}\equiv\text{Fe}^{\text{III}}$ solution instantaneously prior to film deposition as described in Eq. 4.11. Firstly, the $\text{Cu}^{\text{II}}-\text{N}\equiv\text{Fe}^{\text{III}}$ were adsorbed to the rGO surface when the electrode immersed in $\text{Cu}^{\text{II}}-\text{N}\equiv\text{Fe}^{\text{III}}$ solution. This is attributed to ferric ions which possess a high affinity to adsorb on hydrophilic carbon surface (Borisova et al., 2009). After that, the copper $\text{Cu}^{\text{II}}-\text{N}\equiv\text{Fe}^{\text{III}}$ was reduced to $\text{Cu}^{\text{II}}-\text{N}\equiv\text{Fe}^{\text{II}}$ by pyrrole as in Eq. 4.11. Simultaneously, the pyrrole was polymerised by the $\text{Cu}^{\text{II}}-\text{N}\equiv\text{Fe}^{\text{III}}$ which acted as an oxidant. Similarly to ferric ions, pyrrole monomer was deposited on the carbon surface to form PPy layer, attributed to its sp^2 bond nature which is having similar behaviour to the bonds of carbon (Ye, Luo, Ding, Chen, & Liu, 2011). As a result, a layer of CuHCF-PPy nanocomposite was deposited on the surface of the electrode. Repetitive self-assembly deposition cycle produced a denser film.

The mechanism of preparation of CuHCF-PPy is as below:



The suggested formation mechanism of CuHCF-PPy is shown in the schematic diagram in **Figure 4.24**.

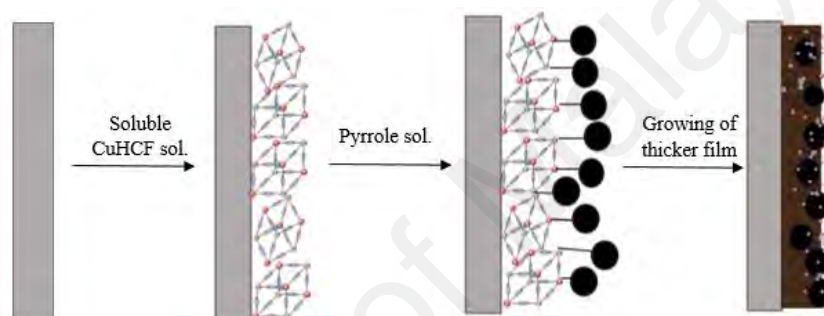


Figure 4.24: Schematic diagram of the self-assembly process of CuHCF-PPy film.

4.2.3 Surface characterisation of CuHCF-PPy film

4.2.3.1 Field-emission scanning microscopy

Figure 4.25 shows FESEM of (A) rGO/CuHCF-PPy in low magnification (6,000 x) and (A)(i),(ii) rGO/CuHCF-PPy, (B) rGO/CuHCF, (C) CuHCF-PPy and (D) CuHCF in high magnification (50,000 x). As seen in the FESEM images of CuHCF-PPy nanocomposite, the films portrayed a mixture of cubic CuHCF with PPy globules on the wrinkled surface of rGO (A) or GCE (C). The particles size (measured using the software "Image J") of nanocomposites CuHCF formed with PPy was found to be approximately 80 nm, attributed to the full growth of CuHCF that enhanced with the addition of PPy as the host to the metal particles (Hostert et al., 2016). Alternatively, the CuHCF formed in

the absence of PPy was irregular and in mesh form, as shown in **Figure 4.25 (B) and (C)**. Besides that, the CuHCF nanoparticles existed in a smaller size (approximately 20 nm). This formation of smaller nanoparticles was due to the increase of copper concentration at the electrode surface as a pyrrole solution was not used in the SA process of CuHCF. The variation of concentration was able to promote the nucleation step which thus contributed to the small particles (Oliveira et al., 2018). Albeit smaller particles formed favours the catalytic effect due to the high surface/inner atom ratio, overlapping between diffusion layers of these nanoparticles will lead to a reduction of signal in CV response when more and more nanoparticles exist at the electrode surface (Campbell & Compton, 2010).

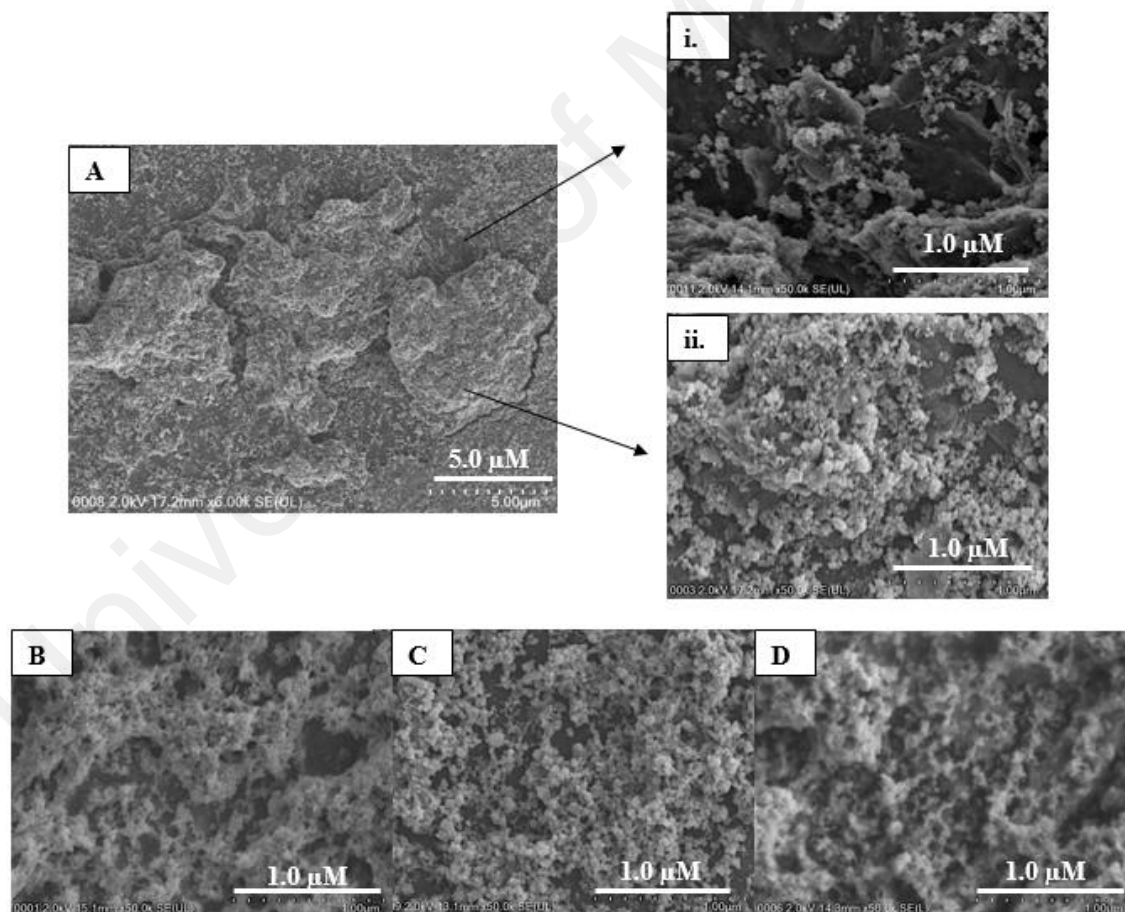


Figure 4.25: FESEM images of (A) rGO/CuHCF-PPy at low magnification (6,000 x) (i) and (ii) of rGO/CuHCF-PPy, (B) rGO/CuHCF and (C) CuHCF-PPy and (D) CuHCF at high magnification (50,000 x).

4.2.3.2 Energy dispersive X-ray spectroscopy

Figure 4.26 portrays the EDX spectra of CuHCF-PPy, rGO/CuHCF and rGO/CuHCF-PPy. Element Cu and Fe were found in the spectrum, indicating that CuHCF was formed on the electrode surface. In addition, the elements C, N and O were observed, suggesting that PPy was successfully polymerised on the electrode. The recorded high percentage of C value was attributed to the nanocomposites were deposited on a glassy carbon plate for screening.

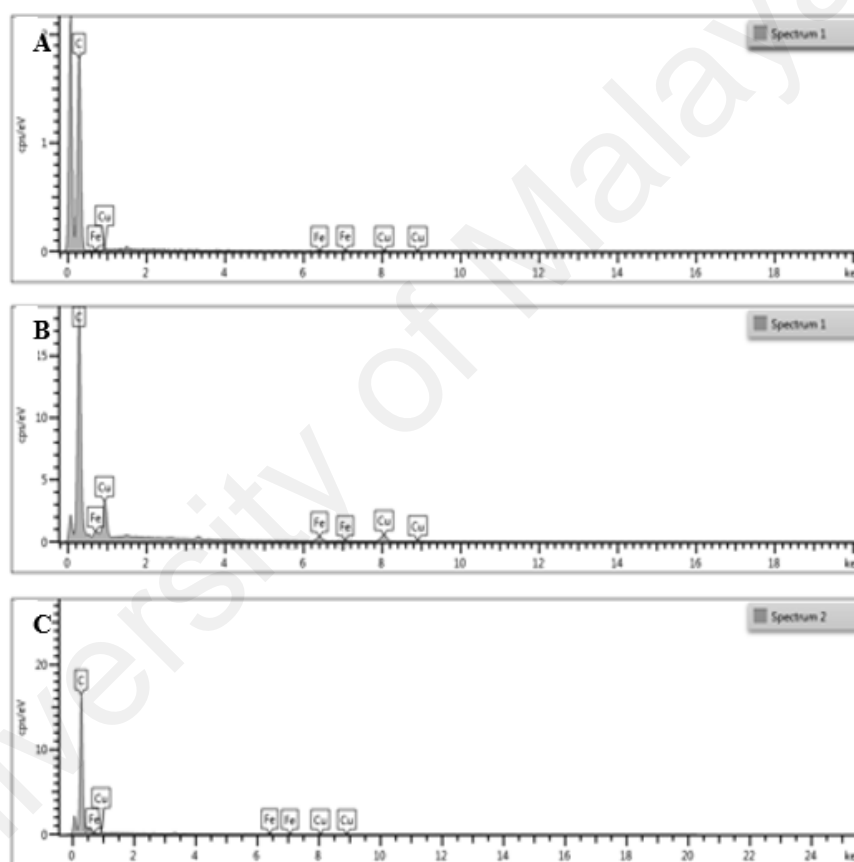


Figure 4.26: EDX spectrum for (A) CuHCF, (B) rGO/CuHCF and (C) rGO/CuHCF-PPy.

4.2.3.3 Fourier transform infrared spectroscopy

The FTIR spectrum of GO is presented in **Figure 4.27 (a)**. The characteristic peaks for GO are located at 3430 (O-H hydroxyl group), 1723 (C=O carboxyl or carbonyl stretching vibration, 1224 (C-OH stretching vibration) and 1060 cm^{-1} (C-O stretching vibration in C-O-C in epoxide) (Wu et al., 2012), whereas the peak at 1621 cm^{-1} might be related to some oxygen-containing groups. For instance, ester, absorbed H_2O or the unoxidised graphitic domains (Mei & Ouyang, 2011). As displayed in FTIR spectra of rGO/CuHCF and rGO/CuHCF-PPy in **Figure 4.27 (b)** and **(c)**, respectively, most of the peaks of oxygen functional groups in rGO disappeared or decreased after the electrochemical reduction of GO, suggesting the successful reduction by electrochemical ways. Besides that, the most representative band of CuHCF which can be observed in all three electrodes was located at 2090 cm^{-1} . This peak was associated with CN stretching absorption band of CN group in Fe^{2+} -CN- Fe^{3+} of CuHCF (Planche et al., 1994). For CuHCF-PPy nanocomposite, there were other peaks related to the N-H stretching vibration in PPy rings, which positioned at 3300 and 2904 cm^{-1} . Additionally, the peaks at 1353 cm^{-1} (Jang & Oh, 2005) and 1079 cm^{-1} were related to the C-N stretching vibration and C-H in plane ring bending of PPy, respectively. These peaks evidenced the formation of CuHCF-PPy nanocomposite on rGO.

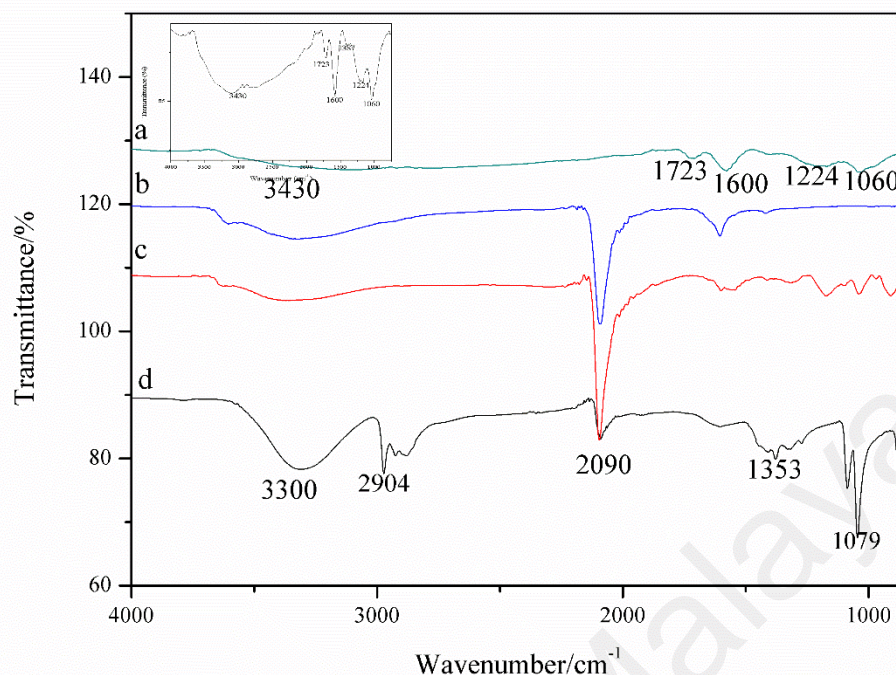


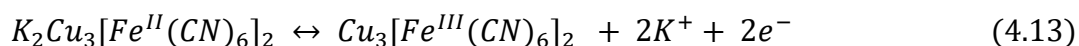
Figure 4.27: FTIR spectrum of (a) GO, (b) rGO/CuHCF and (c) rGO/CuHCF-PPy and (d) CuHCF-PPy. Inset: Magnification of GO spectrum.

4.2.4 Electrochemical behaviour of modified electrode

4.2.4.1 Cyclic voltammogram

Figure 4.28 shows the CV of CuHCF, CuHCF-PPy, rGO, rGO/CuHCF and rGO/CuHCF-PPy. A unique redox couple in the CV presented in Figure 4.28 at approximately +0.7 V was observed once the CuHCF was self-assembled rGO surface. This redox pairs are owing to the redox reaction of [Cu(II)-CN-Fe(III)]/[Cu(II)-CN-Fe(II)] (S.-M. Chen, Li, & Thiagarajan, 2007).

The overall equation for the redox process of CuHCF can be written as follows (Malik & Kulesza, 1996):



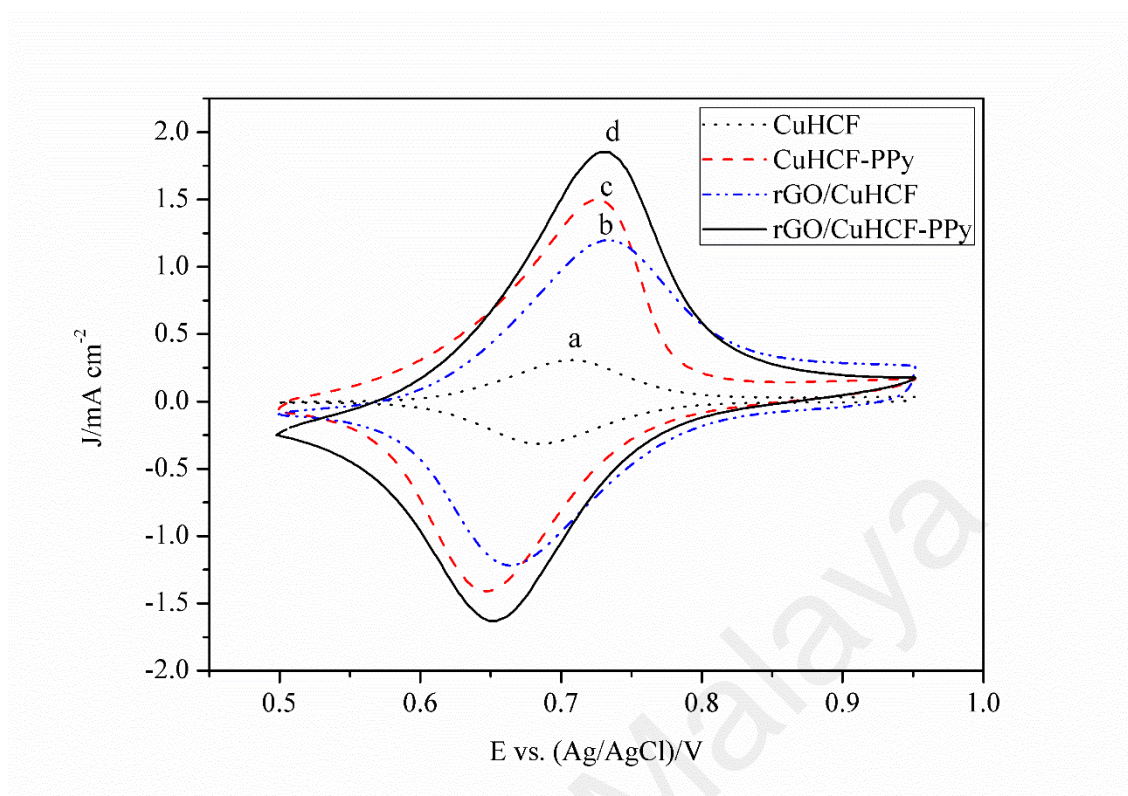


Figure 4.28: CV of (a) CuHCF and (b) CuHCF-PPy (c) rGO/CuHCF, (d) rGO/CuHCF-PPy. The scan rate is 50 mV s^{-1} . The electrolyte used was 0.1 M KCl .

The curve **c** in **Figure 4.28** displays a significant enhancement of CV current response when the conducting PPy formed nanocomposites with CuHCF. This current response of CuHCF was lower than CuHCF/PPy, verifies that the presence of the high number of nanoparticles leads to decrease in CV response as presented in FESEM images above. Nevertheless, the vital factor that contributed to the increase of current response was the existence of conducting PPy which able to improve the conductivity of the whole system. Also, this observation can be attributed to the synergistic effect presents between metal-polymer composite (Nia, Woi, Lorestani, Mahmoudian, & Alias, 2015).

As shown in **Figure 4.29**, there was an enhancement of both anodic and cathodic current when rGO was electrodeposited on the GCE. This finding reveals rGO improved the conductivity of the bare electrode.

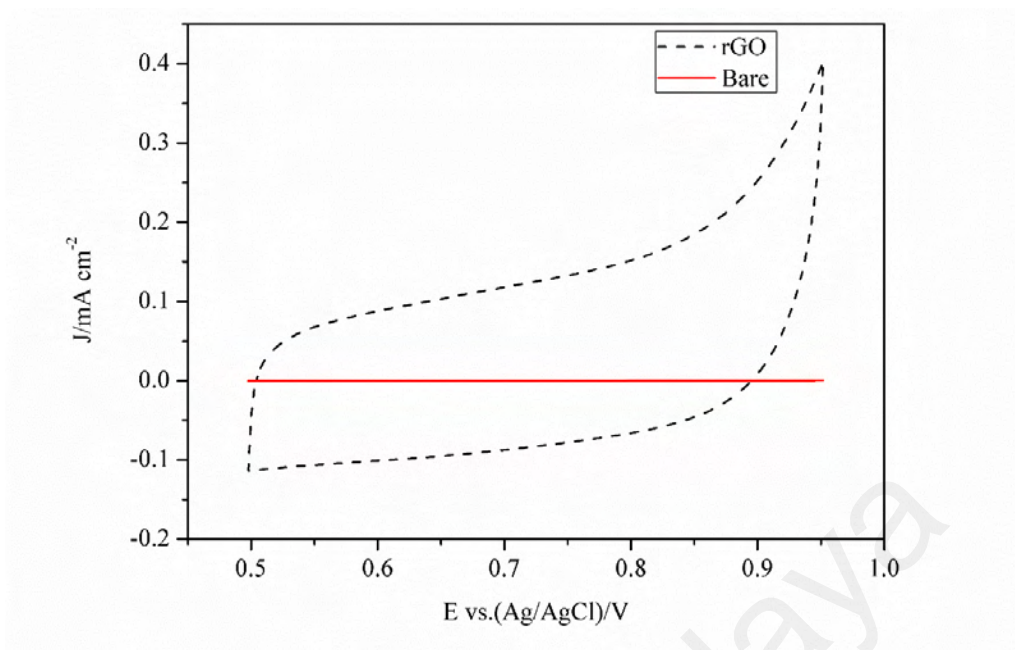


Figure 4.29: CV of (i) Bare GCE and (ii) rGO. The scan rate is 50 mV s^{-1} . The electrolyte used was 0.1 M KCl .

4.2.4.2 Electrochemical impedance spectroscopy

Subsequently, the EIS technique was employed to further study the electrochemical behaviours of the electrodes. The EIS measurements were conducted via the amplitude of a sine wave of 5 mV applied in a frequency range of 10 kHz to 0.1 Hz at open circuit potential (OCP) in $5 \text{ mM Fe(CN)}_6^{3-/4-}$ redox probe with 0.1 M KCl as supporting electrolyte. NOVA 1.11 software was used to fit the experimental data with an equivalent circuit by analysing the Nyquist plot and Bode plot.

As shown in **Figure 4.30**, Nyquist plot of impedance spectra for modified electrodes of CuHCF, CuHCF-PPy and rGO, comprised of semicircle portion at higher frequencies, which correlated to the electron transfer limited process, and its diameter is equivalent to the charge-transfer resistance (R_{ct}) (Nia, Woi, & Alias, 2015). On the other hands, a linear portion (45°) at lower frequencies is correlated to the diffusion process by the transport of ions, which can be represented by a Warburg element (W) (Nia, Woi, & Alias, 2017). Hence, the Randles equivalent circuit was used in the fitting of these modified electrodes.

The Randles model contains ohmic resistance of the solution (R_s), constant phase element (Q), charge transfer resistance (R_{ct}) which occurs across the electrode-electrolyte interface and a Warburg element. This mentioned Randles circuit was presented in the **inset** of **Figure 4.30**. A pure capacitor (C) was substituted by a constant phase element (CPE) in the fitting procedure with the aim to obtain a satisfactory relationship between the experimental and fitting data (Petovar, Xhanari, & Finšgar, 2017).

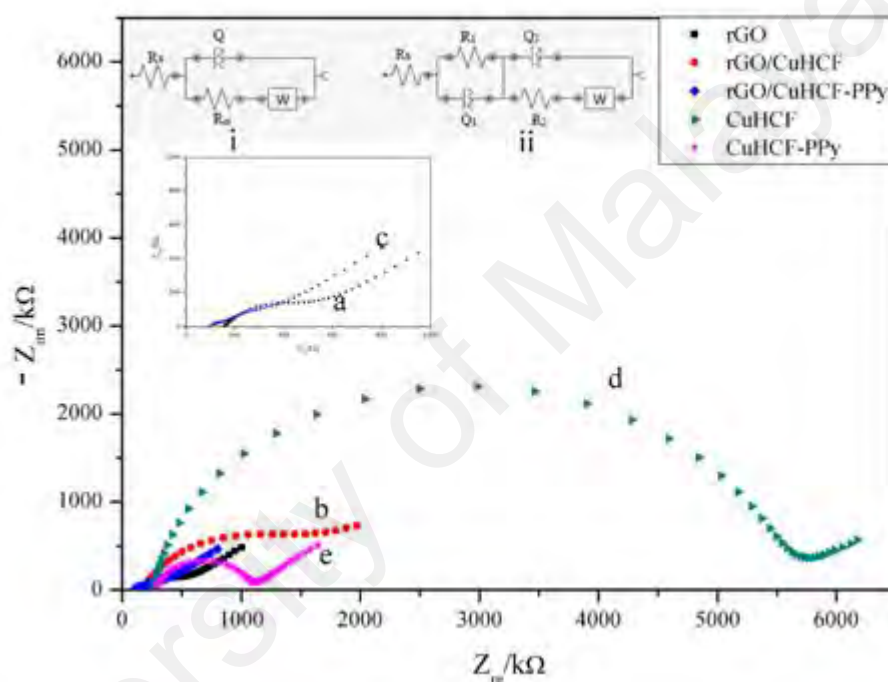


Figure 4.30: Nyquist plot (a) rGO, (b) rGO/CuHCF, (c) rGO/CuHCF-PPy, (d) CuHCF (20). Inset: Equivalent circuit (i) for rGO, CuHCF, CuHCF-PPy and (ii) rGO/CuHCF and rGO/CuHCF-PPy. Electrolyte used is 0.1 M KCl solution containing 5 mM $\text{Fe}(\text{CN})_6^{3-/4-}$ (1:1).

The diameter of the semicircle decreases significantly when rGO was used as the base material as shown in curve **a**, **b** and **c** in **Figure 4.30**. The results revealed that the modification of GCE by rGO reduced the resistance of the electrodes tremendously due to the fact that the rGO has a small band gap (P. Chen et al., 1995).

On the other hand, two semicircle features can be observed from the high and medium frequencies of rGO/CuHCF and rGO/CuHCF-PPy based on the Nyquist plot in **Figure 4.30**. From the Nyquist plot, a smaller semicircle appeared at higher frequencies, followed by second larger semicircle at medium frequencies and lastly, Warburg diffusion was observed in low frequencies. This phenomenon is expected due to the presence of two layers of materials comprising of rGO and metal layer (CuHCF) or metal-polymer layer (CuHCF-PPy) on the electrodes. In addition, two phase angles were observed in the Bode plot in **Figure 4.31**.

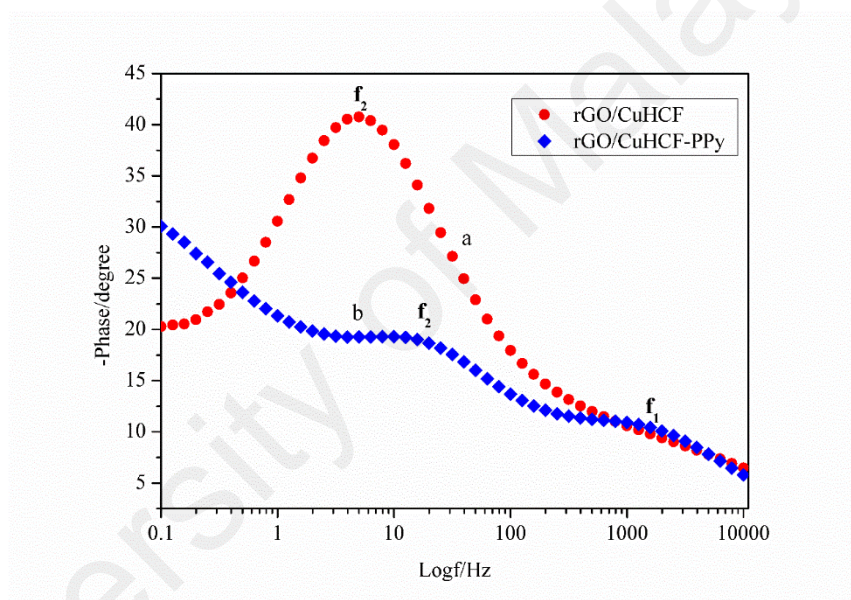


Figure 4.31: Bode phase of (a) rGO/ CuHCF and (b) rGO/CuHCF-PPy.

The phase angle in the high (f_1) frequency regions is attributed to the R_{ct} which happens across the electrode-electrolyte interface (CuHCF or CuHCF-PPy/solution) whereas the second phase angle (f_2) is due to CuHCF or CuHCF-PPy/rGO interface. Hence, two R|CPE combinations were used to fit the corresponding data and demonstrated in the inset (ii) of **Figure 4.30**. The results show that both R_{ct} are lower with the presence of conducting PPy.

From **Table 4.6**, the R_{ct} can be organised in such order: CuHCF > CuHCF-PPy > rGO > rGO/CuHCF > rGO-CuHCF-PPy. The result obtained from the fitting was in good agreement with the Bode plot, in which f_2 intensity of rGO/CuHCF was considerably higher than rGO/CuHCF-PPy. This indicates that the surface resistance decreases significant from rGO/CuHCF to rGO/CuHCF-PPy (Y. W. Park, 2010). Also, these findings confirmed sequences of current intensity demonstrated in the above CV.

In addition, the CuHCF-PPy/rGO has a higher Warburg impedance value than CuHCF/rGO, indicated a higher diffusion of electrolytic ions (Maitra et al., 2017). Henceforth, conducting PPy increases the conductivity of the nanocomposites as well as enhances the diffusion of electrolytic ion transportation at the electrode-electrolyte interface (G. Yang, Cui, Yang, & Wang, 2014).

Table 4.6: Electrochemical parameters obtained by fitting EIS results.

Types of electrode	R_s (Ω)	R_{ct1} (k Ω)	Q_1 (uMho)	N	R_{ct2} (Ω)	Q_2 (uMho)	N	W (mMho)
CuHCF	261	5.28	1.17	0.914	-	-	-	1.46
CuHCF-PPy	284	0.80	1.33	0.870	-	-	-	1.64
rGO	156	0.42	1.83	0.675	-	-	-	1.83
rGO/CuHCF	102	0.12	297	0.449	1.46	111	0.82	1.60
rGO/CuHCF-PPy	98	0.05	33.6	0.707	0.26	240	0.68	1.84

4.2.5 Electrochemical sensing towards nicotine

The following study investigated the quantitative detection and electrocatalytic behaviour of rGO/CuHCF-PPy film towards nicotine. As seen in **a** and **b** **Figure 4.32**, a small increase of current was observed on the unmodified GCE and rGO with a potential of 0.9 V in the presence of nicotine. On the other hand, **curve c** showed the rise of anodic peak current and decreasing of cathodic peak current, indicating the electrocatalytic

oxidation of CuHCF towards nicotine (S.-M. Chen, Li, & Thiagarajan, 2007; Razmi et al., 2009). In addition, the oxidation potential of nicotine was able to lower down from +0.9 V to +0.72 V, suggesting that CuHCF modifier is necessary for the electrocatalytic oxidation of NIC (Jing, Yuan, et al., 2016). Also, the current response of rGO/CuHCF-PPy increases in proportional to the concentration of nicotine.

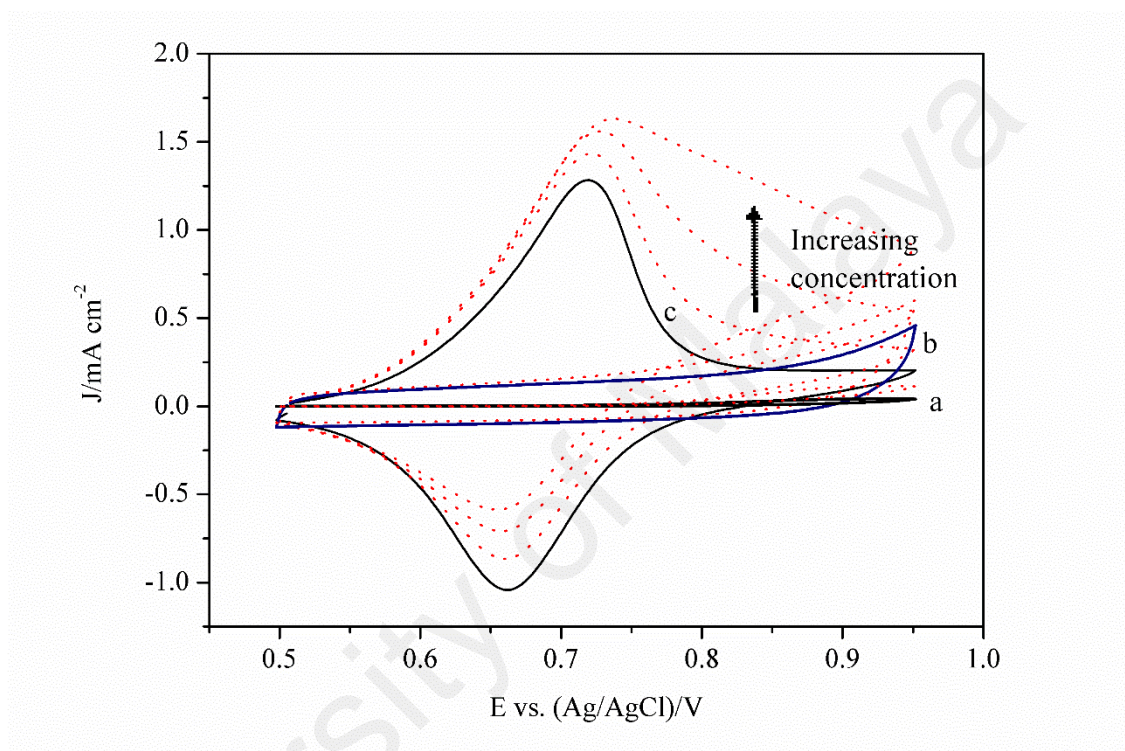


Figure 4.32: CV of (a) GCE and (b) rGO in the absence (solid) and presence (dotted line) of 1 mM nicotine; c) rGO/CuHCF-PPy in the absence (solid) and presence (dotted line) of 1 to 3 mM nicotine with 0.1 M KCl as supporting electrolyte.

The mechanism of nicotine oxidation can be expressed as in **Figure 4.33** (Li et al., 2017). Prior to amperometric testing, the optimum working potential was investigated.

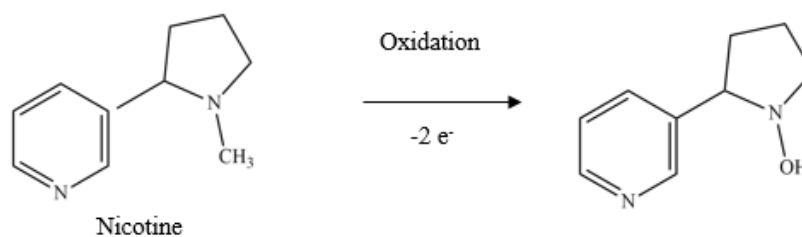


Figure 4.33: Mechanism of nicotine oxidation.

Figure 4.34 shows the applied potential effects towards the oxidation current response of 1 mM nicotine in the range from +0.75 V to +0.9 V. This potential range was selected due to the current increment was more obvious at the higher potential (after the E_{pa} located at approximately +0.72 V) as presented in **Figure 4.32**). More importantly, the conversion of CuHCF to its oxidised species was more favourable at higher potential and hence able to promote the electrocatalytic reaction between the oxidised CuHCF and nicotine. Also, this explained the reason that the amperometric current response towards nicotine was in proportional to the applied potential from +0.75 V to +0.90 V. The steady-state current increased drastically when the potential used was set as +0.85 V. Thus, the applied potential +0.85 V was chosen as the working potential in this study, instead of +0.90 V. This is due to the first potential that leads to the significant increase in current response towards 1 mM nicotine should be chosen as working potential to avoid interference effect at high potential (Lorestani, Nia, Alias, & Manan, 2015).

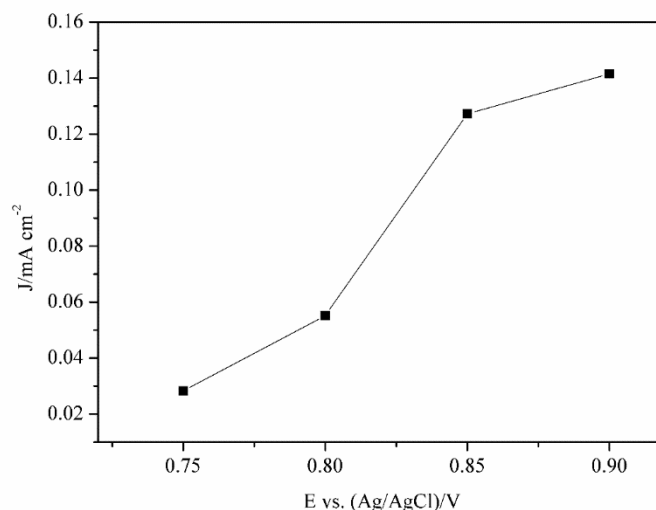


Figure 4.34: Oxidation current response of 1 mM nicotine vs. applied potential.

The influence of the NDC layer of CuHCF-PPy in the electrochemical detection of nicotine was investigated. The amperometric response recorded in **Figure 4.35** on concentration ranges from 1 to 5 mM of nicotine. It was noticed that the current intensity was increased from 5 to 10 layers, but then reduced back when NDC was 15. This phenomenon could be owing to the electron transfer was obstructed due to the film thickness. These results show the sensitivity of the modified electrode towards nicotine sensing can be controlled just by adjusting NDC during the SA preparation process. Therefore, the rGO/CuHCF-PPy (10) was used for the nicotine determination.

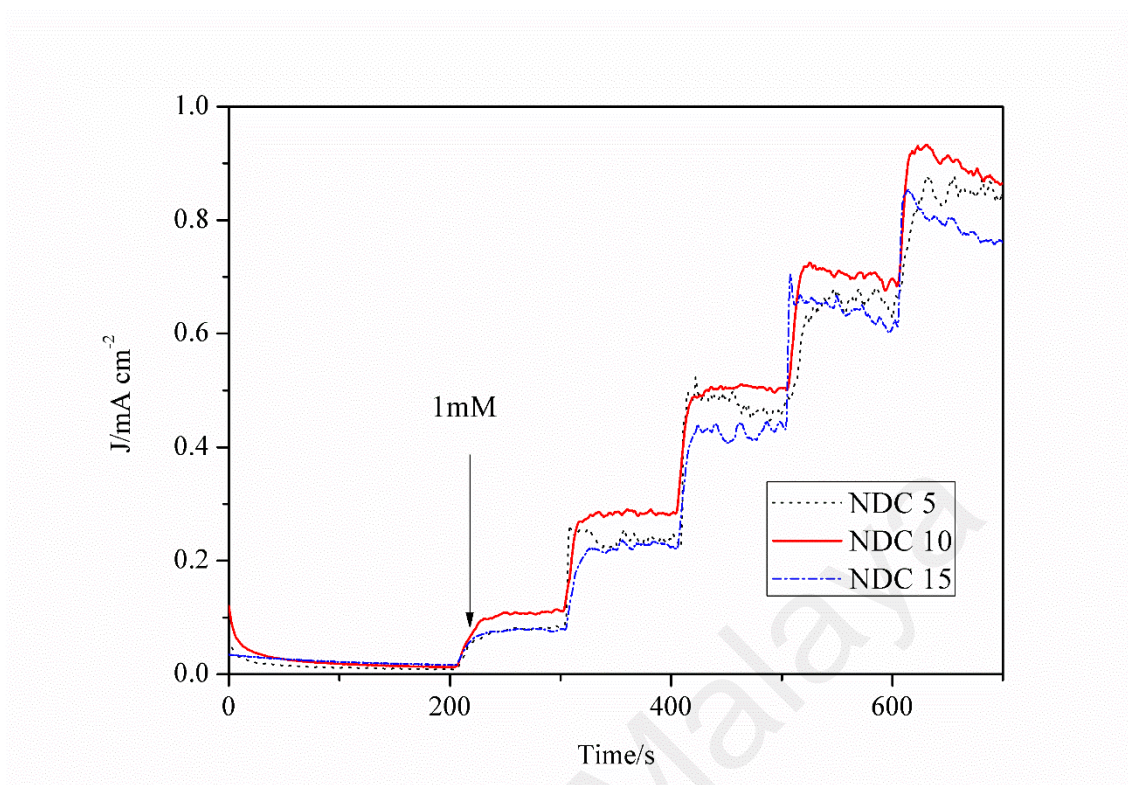


Figure 4.35: Amperometric curve of rGO/CuHCF-PPy with 5 to 15 NDC towards 1 mM to 5 mM nicotine.

Also, it is in common practise where researchers will choose average pH 5 to 10 for the detection of nicotine (Cinková, Dianová, Vojs, Marton, & Švorc, 2015; Fekry, Azab, Shehata, & Ameer, 2015; Goodarzi et al., 2015; Levent, Yardim, & Senturk, 2009; Li et al., 2017) as nicotine exists prevalently in the deprotonated state in acidic pH (pH 2.0-2.7) which presumably difficult for the oxidation of nicotine. On the other hand, the monoprotonated form of nicotine presents in the range of pH 4.5-7 and un-protonated free base forms in pH > 9 (Li et al., 2017).

In addition, CV response of CuHCF-PPy in alkaline condition was not stable as its redox peak diminished right after the first half of CV scan, which is attributed to the hydrolysis reaction as follows (Gholivand, Khodadadian, & Omidi, 2013):





Furthermore, it is worth to mention that the measured pH of the e-cigarettes sample which purchased from the market was also closed to pH 5.5. Thus, 0.1 M KCl (pH measured as 5.5) was used as supporting analyte in further studies.

Besides that, it can be clearly seen that the analytical performance of CuHCF was drastically enhanced with the presence of conducting PPy. The amperometric curve of pristine CuHCF towards nicotine was sluggish and not stable as demonstrated in the **Figure 4.36** curve (a). However, PPy alone will not demonstrate any analytical response towards nicotine as shown in the **inset** of **Figure 4.36**. The stability and sensitivity for the amperometric response of CuHCF-PPy are further improved when it self-assembled on wrinkle rGO surface as compared to on bare GCE surface. This can be credited to the high surface area provided by rGO for the attachment of CuHCF-PPy. Thus, the best nanocomposite towards the nicotine detection was rGO/CuHCF-PPy due to the presence of conducting polymer and support layer of rGO that provided a larger surface area, thus better performance in term of sensitivity and stability.

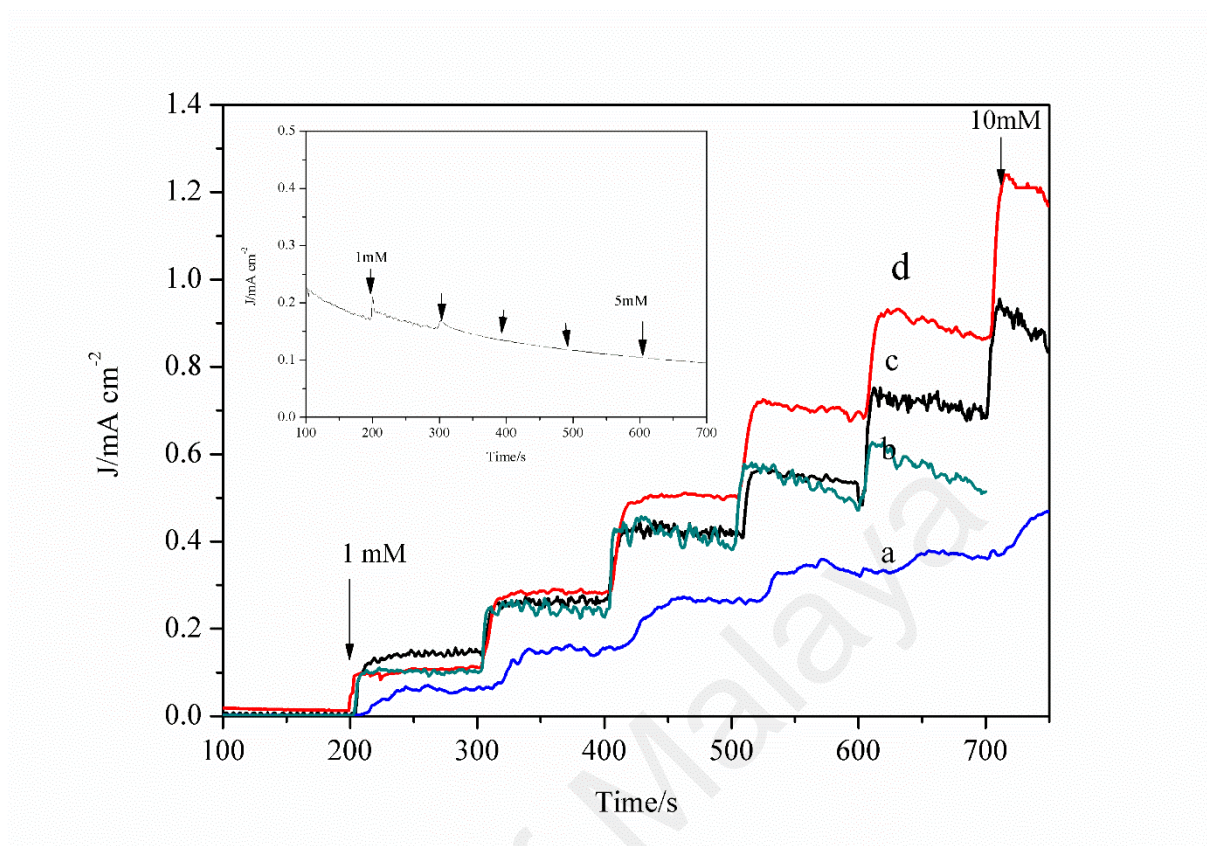


Figure 4.36: Amperometric testing curve of various modified electrodes: (a) CuHCF, (b) CuHCF-PPy, (c) rGO/CuHCF and (d) rGO/CuHCF-PPy; Insets: Amperometric curve of PPy towards 1 to 5 mM nicotine.

Moreover, the good linearity between the I_{pa} and the scan rate ($R^2= 0.996$) presented in **Figure 4.37 (A)** reveals that the nicotine oxidation process on rGO/CuHCF-PPy modified electrode is an adsorption controlled process (B. Yang, Bin, Zhang, Du, & Majima, 2018). According to Laviron's equation, the charge transfer coefficient (α) and electron transfer rate constant (k_s) can be calculated from the slope of peak potential (E_p) versus the logarithm of scan rates for an adsorption-controlled process. Nevertheless, this term is only applied for the condition where the $\Delta E_p/n > 200$ mV. Hence, $\alpha= 0.5$ is used for this case whereas the relative error on k_s is at maximum 6% (Laviron, 1979). The same α value was also applied in the previous report mentioned (M. Wang et al., 2018). The k_s was evaluated via the following Laviron's equation:

$$\log k_s = \alpha \log(1 - \alpha) + (1 - \alpha) \log \alpha - \log \frac{RT}{nFv} - \alpha (1 - \alpha) nF \frac{\Delta E_p}{2.3} RT \quad (\text{Eq. 4.16})$$

Where v is the scan rate, n is the number of transferred electrons, R is gas constant and T is temperature.

Besides that, the n value can be calculated using the slope of E_{pa} vs. logarithm of scan rate as displayed in **Figure 4.37 (A)**. The graph E_{pa} vs. logarithm scan rate as shown in **Figure 4.37 (B)** displayed a linear relationship between 20 to 100 mV s^{-1} . The slope for the linear equation corresponding to E_{pa} is equal to $2.3 RT / (1 - \alpha) nF$ (given $\alpha = 0.5$) (Anuar, Basirun, Ladan, Shalauddin, & Mehmood, 2018). Here, the n obtained was $1.95 \approx 2$, where 2 of the electrons were involved in the electrochemical oxidation of nicotine. The result obtained further confirmed the hypothesis of the same number of electrons involved in nicotine oxidation by Suffredini and co-workers 2005. Based on this information, the k_s value calculated from Eq. 4.16 is 1.83 s^{-1} .

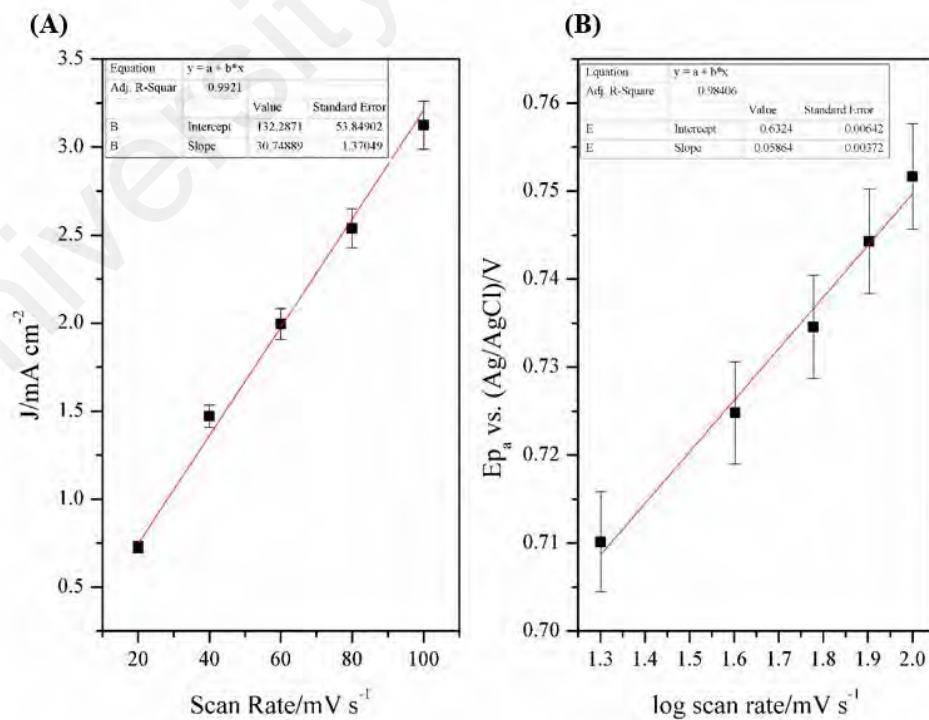
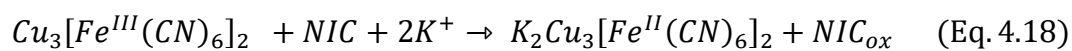
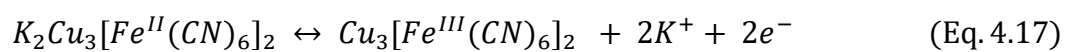


Figure 4.37: (A) Plot I_{pa} vs. scan rate and (B) Plot of E_{pa} vs. $\log v$.

Hence, the mechanism of the electrocatalytic reaction of CuHCF towards nicotine can be written as follows:



During the electrocatalytic process, [Cu(II)-CN-Fe(II)] is regenerated by a chemical reaction between nicotine and [Cu(II)-CN-Fe(III)].

University of Malaya

4.2.6 Application as nicotine sensor

Amperometry method under stirred conditions was used to quantify the amount of nicotine to calculate the limit of quantification (LoQ) and limit of detection (LoD). **Figure 4.38** shows the typical amperometric response upon successive addition of nicotine under stirred condition from 0.03 mM to 5 mM at rGO/CuHCF-PPy electrode at working potential of +0.85 V. The linear equation can be expressed as: $J \text{ (mA cm}^{-2}\text{)} = 0.2115 \text{ (mA cm}^{-2}\text{ mM}^{-1}\text{)} + 0.211 \text{ (R}^2=0.995\text{)}$. The calculated LoQ and LoD is at 7.76 nM and 0.0258 μM (S/N= 3), respectively.

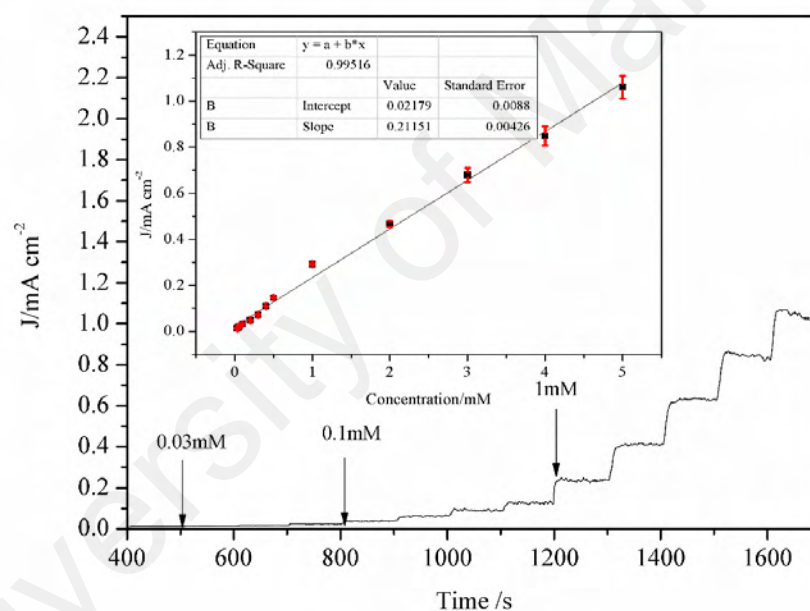


Figure 4.38: Amperometric response of rGO/CuHCF-PPy electrode upon successive addition of nicotine from 0.2 to 5 mM. Operating potential: +0.85 V. Inset: Calibration curve.

4.2.6.1 Interference test, stability and reproducibility

Figure 4.39 shows a typical amperometric curve of some interference species including glycerin, propylene glycol (PG), glucose, sucrose, H_2O_2 , and uric acid (UA). The targeted real sample in our study—vape solution, normally only contains glycerin, PG and various concentration of nicotine (range from 0 mg mL^{-1} to 24 mg mL^{-1}). Albeit the H_2O_2 interfered the sensor response, H_2O_2 was generated from the auto-oxidation of polyphenolic species in the formation of cigarette smoke (Hu, Zhang, & Yang, 2007) and its response was lower than nicotine. Moreover, the interference test for the nicotine sensor was relatively insignificant, attributed to the low concentration of other minor alkaloids (0.2-0.5 %). Furthermore, cotinine (COT), which is the main metabolites of nicotine, is electrochemical inactive and to our best knowledge, no direct electrochemical detection of COT have been published up to date (Švorc, Stanković, & Kalcher, 2014). Nevertheless, the interference test for tobacco products, especially cigarettes still remains as a major challenge as there are around 4000 chemical compounds found in cigarettes (Smith & Hansch, 2000).

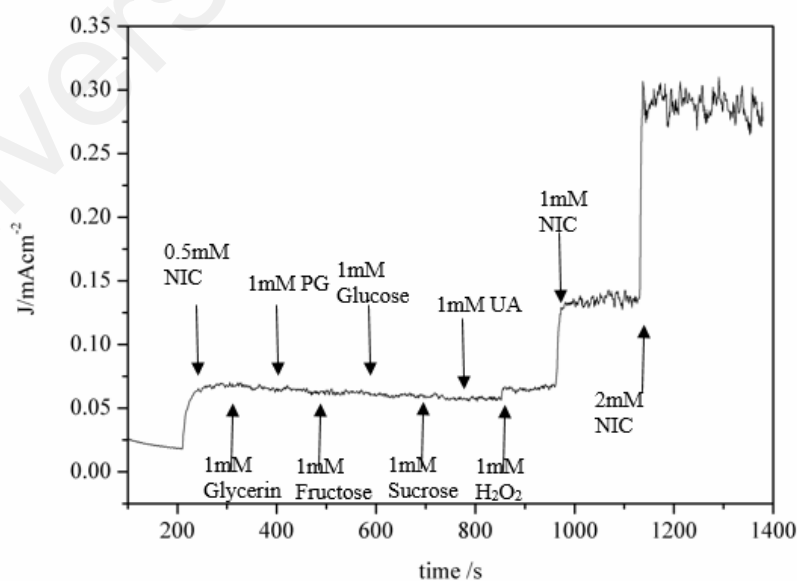


Figure 4.39: Amperometric current response of CuHCF-PPy to the addition of 0.5 mM nicotine (NIC), 1 mM glycerin, propylene glycol (PG), fructose, glucose, sucrose, uric acid (UA), H_2O_2 , 1 mM nicotine (NIC) and 2 mM nicotine (NIC) at operating potential +0.85 V.

To evaluate the reproducibility of the proposed nicotine sensor, five electrodes were used to detect 1 mM nicotine. The relative standard deviation (RSD) obtained was 5%, demonstrating satisfactory reproducibility for electrode modified by self-assembly method. The long-term stability was investigated by testing the modified electrode every week for three weeks consecutively. The current response of the modified electrode was remained at 98.6 % of their original activity as present in **Figure 4.40**. Thus, the proposed modified electrode has excellent stability.

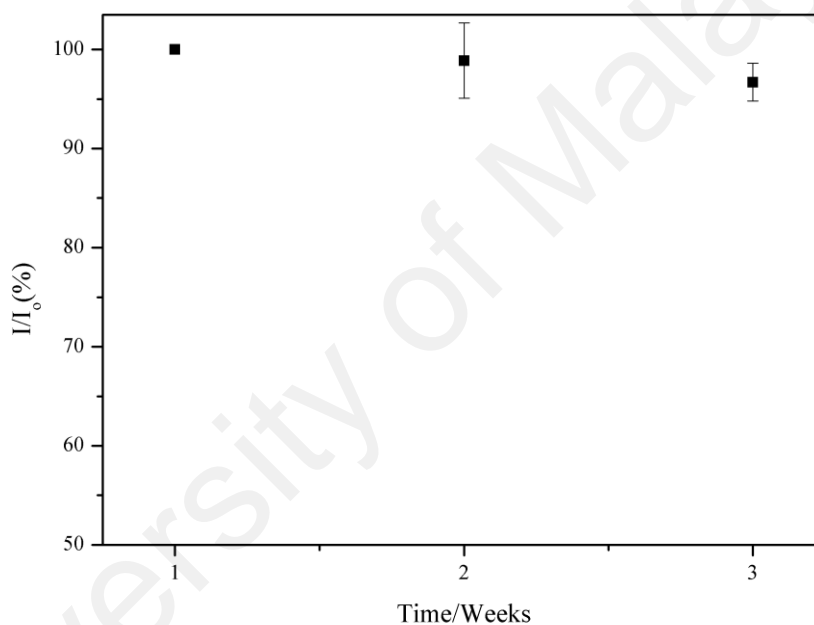


Figure 4.40: Stability of modified electrode in three weeks.

4.2.6.2 Real sample application

The real application of rGO/CuHCF-PPy was tested by two means: i) spiked sample analysis and ii) detecting nicotine concentration in e-cigarette solution containing nicotine. Standard addition method was employed for these testings. The pre-treatment of the sample was stated in the methodology part above. The results obtained for the vape sample by the proposed method and the comparison with an established HPLC method (Vlase, Filip, Mîndruțău, & Leucuța, 2005) are stated in **Table 4.8**. The retention time of nicotine was approximately 3.25 min (with * label) as shown in **Figure 4.41**. The standard deviation of the calibration curve was plotted but the value was too small to be noticed as presented in **Figure 4.42**.

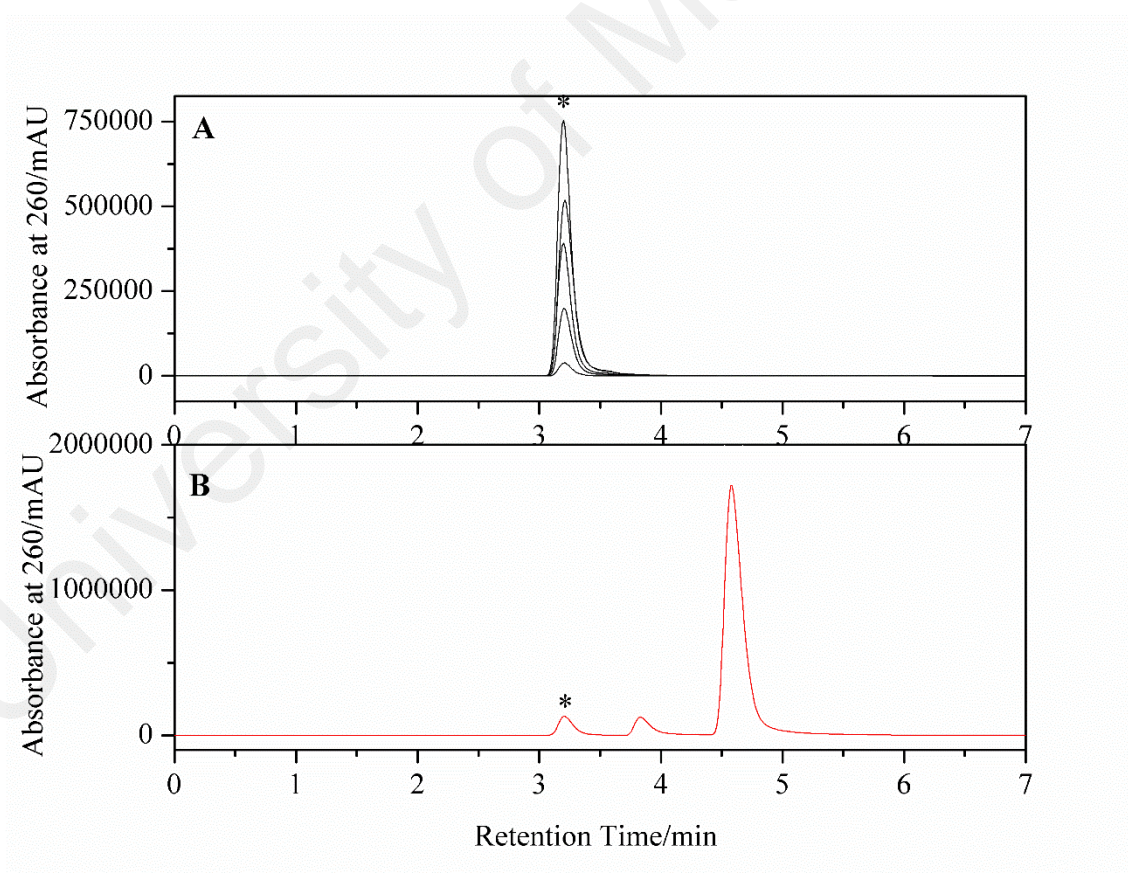


Figure 4.41: (A) HPLC response of standard nicotine solution from 0 to 20 mM. (B) HPLC response of e-cigarettes (vape) solution.

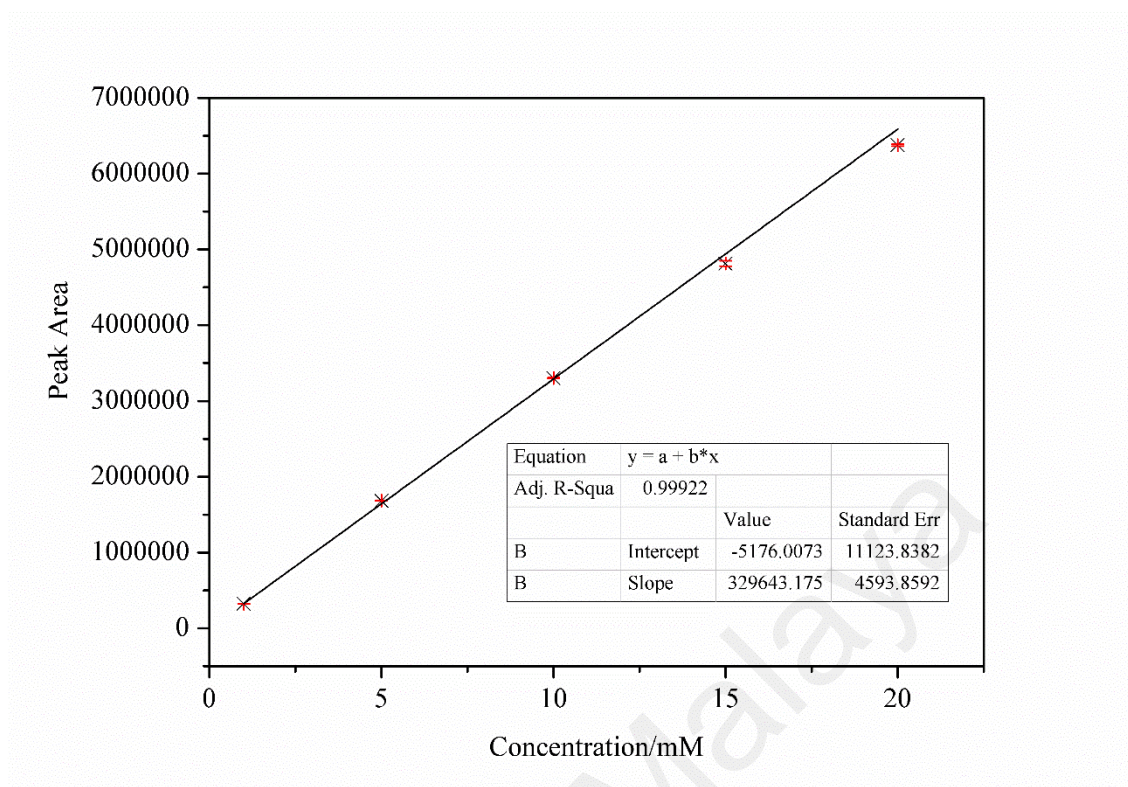


Figure 4.42: HPLC calibration curve for nicotine standard solution.

Table 4.7: The recovery of nicotine spiked in vape product (0 mg mL⁻¹ nicotine) and detection of nicotine in vape sample.

Sample	Added (mM)	Detected (mM)	Recovery (%)	RSD (%)
1	0.1	0.095	95	5
2	0.5	0.5	100	4
Sample	HPLC-UV Determined (mM)	Detected (mM)	Recovery (%)	RSD (%)
A	7.6	0.72*	97.4	2.77

*The sample was diluted 10 times with 0.1M KCl.

4.2.6.3 Comparison with other work

The performance of nanocomposites obtained is compatible with those reported in the previous study as listed in **Table 4.7** albeit relative facile procedure and cheaper material were employed. In addition, the present rGO/CuHCF-PPy modified electrode can complement a higher concentration range of nicotine detection (from 0.03 to 5 mM) as compared to the earlier literature. The highest concentration detected in the previous

report was only up to 1 mM (Sims, Rees, Dickinson, & Compton, 2010). Furthermore, most of the preceding work focused on detecting nicotine in the μM range, due to different targeted sample and limitation of the proposed sensor. As the concentration of nicotine in vape (e-cigarettes) solution can be up to 24 mg mL^{-1} (148 mM) (Palazzolo, 2013), the sensor proposed in our work will be relatively practical for detection of tobacco products as compared to other modified electrode, especially dealing with this kind of vape sample which are now widely available in market nowadays.

Table 4.8: Comparison of nicotine amperometric sensors.

Modified electrode	Analysis method	E (vs. Ag/AgCl)/V	Sensitivity ($\text{mA cm}^{-2} \text{mM}^{-1}$)	LoD (μM)	Linear range (mM)	Ref.
Palladium hexacyanoferrate incorporated graphene oxide	Amp.	+0.75	1.208	0.8	0.008-0.24	C. Y. Yang et al. (2016)
rGO-supported gold NPs	Amp.	+0.93	NA	0.015	0.0005 - 0.05	Jing, Lin, et al. (2016)
Screen-printed carbon electrode modified with nitrogen-doped graphene sheets	Amp.	+0.85	0.627	0.047	Up to 0.02	Li et al. (2017)
MWCNT-alumina coated silica nanocomposites	Amp.	+0.7	NA	1.42	0.005-0.2	(S. J. Wang et al., 2009)
Self-assembled CuHCF-PPy on GCE	Amp.	+0.85	0.21	0.026	0.03 – 5	This work

NA=not applicable

CHAPTER 5: CONCLUSION AND RECOMMENDATIONS

5.1 Summary

This research project was conducted to investigate a facile novel approach to synthesise MeHCF-based nanocomposites and the influence of the different fabrication methods towards the characteristics of the nanocomposites formed. Also, this study has sought to explore the applications of these MeHCF-based nanocomposites as electrochemical sensors, as well as the other possible electrochemical applications. It was later discovered that one of the MeHCF-based nanocomposites-PB-PPy nanocomposites can be used to form energy storage material. Coincidentally, there were few pieces of recent literatures which revealed the MeHCF-based nanocomposites as both electrochemical sensors and as electrochemical capacitors, proposes an open opportunity for exploration of dual-functional materials. Hence, a summarised of the findings was tabulated based on the objectives as presented in the following paragraph:

- i. To synthesise and fabricate MeHCF-based nanocomposites by a novel facile method.**

The PB-PPy nanocomposite was deposited directly on a glassy carbon electrode (GCE) by novel self-assembly (SA) method based on multiple sequential adsorptions of $\text{FeCl}_3\text{-K}_3[\text{Fe}(\text{CN})_6]$ and pyrrole. It was the first time a MeHCF based nanocomposite adsorbed on GCE surface without any linkers (in-situ synthesis). Previously, the in-situ synthesis of PB or its nanocomposite was often achieved by electrodeposition whereas chemical reaction approach usually forms PB nanocomposites before adhering onto an electrode.

ii. To compare the new method of electrode modification with the conventional method.

The PB-PPy nanocomposite was also prepared by existing one-pot electrodeposition (ED) method for comparison. It is worth to mention the adapted ED method (Özkale et al., 2014; Zolotukhina et al., 2014) was designated based on the consideration of imitating the SA method to the greatest extent.

The research findings revealed the PB-PPy synthesised with SA and ED methods possess respective distinguish characteristics. The FESEM images demonstrated that morphology of SA PB-PPy nanocomposites was in random spherical shape in which PB and PPy overlapped/combined with each other, whereas electrodeposited PB-PPy was in nanocubic framework under the presence of PPy layer.

It is well known that morphology affects the electrochemical performances of the modified electrode in term of conductivity, stability and its applications. ED PB-PPy exhibited unusual peaks splitting as observed in CV due to its nanocubic morphology. In addition, the electrocatalytic reduction towards H_2O_2 was not as stable as SA PB-PPy. This is due to some of the PB or PPy were re-dissolved in bath solution in the phase of opposite applied potential. This phenomenon reducing the adhesion of PB-PPy towards the electrode, suggesting it will be easier to prepare in-situ PB-PPy nanocomposites (one-layer with a combination of MeHCF and polymer) by the SA method.

iii. To demonstrate the synthesised nanocomposite as the electrochemical sensor.

The SA PB-PPy nanocomposites were demonstrated as H₂O₂ electrochemical sensors with the sensitivity of 384.7 mA M⁻¹ cm⁻² whereas a SA CuHCF-PPy nanocomposite was prepared for this sensing of nicotine. Additionally, rGO was deposited on the GCE first to increase the stability of CuHCF-PPy in sensing of nicotine. The sensing performance of CuHCF-PPy without the support of rGO demonstrated a sluggish amperometric curve towards nicotine. This proposed sensor nicotine detection in a high concentration range up to 5 mM with compatible sensitivity of 211.5 mA M⁻¹ cm⁻², which significantly ousted the previously reported nicotine detection range and feasible for real application. For its real sample application, e-cigarettes solution was used as the target sample.

iv. To investigate the potential of the synthesised nanocomposite as energy storage materials

The supercapacitor characteristic shown by SA PB-PPy (20) in the previous section was further investigated in preliminary result for further study. The result indicated that the direct SA method can synthesise MeHCF-PPy nanocomposites as an electrochemical sensor, as well as act as an energy storage material, which makes this nanocomposite multifunctional, suggested that the proposed SA method is capable to tune the electrochemical properties of the material. The synthesised PB-PPy nanocomposite demonstrated intercalation pseudocapacitive behaviour, which is an intermediate between pseudocapacitor behaviour and battery behaviour.

5.2 Preliminary result for MeHCF-PPy nanocomposite as potential energy storage material

Previously, the synthesis of PB-PPy nanocomposite via direct self-assembly (SA) approach without any linking agents on the glassy carbon electrode (GCE) was reported for the first time and its application as hydrogen peroxide electrochemical sensor was investigated in the **Section 4.1**. It was later found that PB-PPy nanocomposite which formed by 20 deposition cycles exhibited the pseudocapacitor behaviour, which indicated that the nanocomposites with different electrochemical behaviour can be tuned and fabricated, simply by adjusting its deposition cycles. The observed phenomenon leads to further investigation on the performance of this SA PB-PPy nanocomposite as the pseudocapacitive material. Hence, here in this part, the focus was the applications of PB-PPy as the energy storage material where the PB itself was prepared with the same SA approach on glassy carbon electrode (GCE), acting as a control, and PB-PPy nanocomposites were prepared based on the method developed in **Section 4.1**.

5.2.1 Surface characterisation of PB and PB-PPy

5.2.1.1 Field emission scanning microscopy

Figure 5.1 portrays the FESEM of PB and PB-PPy electrode. As shown in **Figures (A)** and **(B)** it can be clearly seen that there was only nanocubic PB formed. However, most of the PB crystals showed the incomplete characteristic of nanocube. The size of the PB particles was approximately 40 nm (measured by software *Image J*). On the other hand, the PPy was connected to the PB particles and they were overlapping with each other due to the fact that the conducting polymer acts as the host to the PB particles.

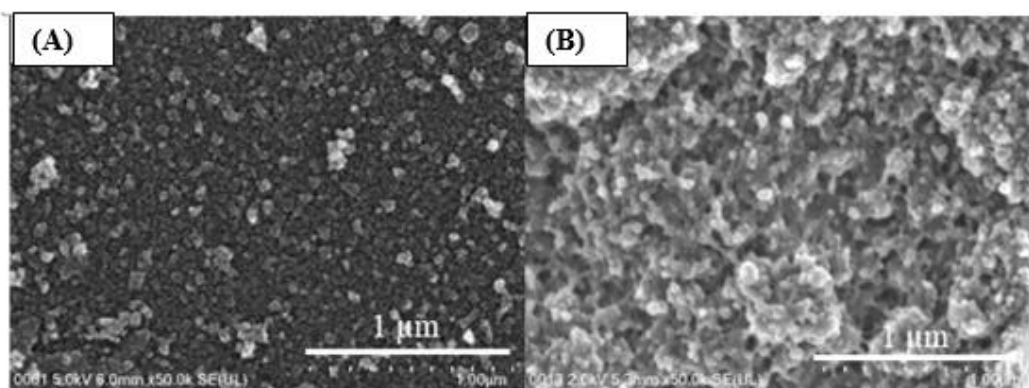


Figure 5.1: FESEM images of (A) PB and (B) PB-PPy in 50,000 x magnification.

5.2.1.2 Fourier transform infrared spectroscopy

Figures 5.2 (A) and (B) illustrate the FTIR spectrum of PB and PB-PPy, respectively. For the PB FTIR, the wavenumber, 2090 cm^{-1} was corresponding to CN stretching absorption band of the CN group in $\text{Fe}^{2+}\text{-CN-Fe}^{3+}$ of PB, whereas the wavenumber, 2181 cm^{-1} can be attributed to the $\nu(\text{CN})$ band for PB. The FTIR for PB-PPy was similar to the FTIR spectra in **Section 4.1.2.3**.

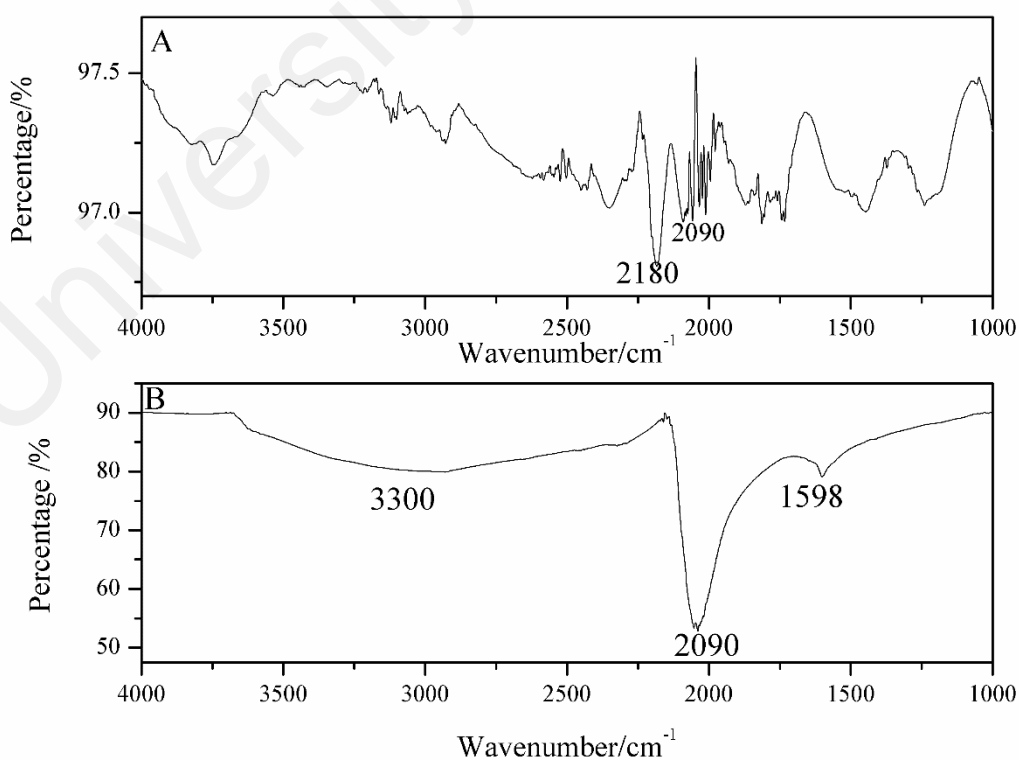


Figure 5.2: FT-IR spectrum of (A) PB and (B) PB-PPy on glassy carbon electrode.

5.2.2 Electrochemical behaviour of modified electrode

Two well-defined redox pairs as shown in **Figure 5.3** were attributed to the conversion of Prussian white (PW) to Prussian blue (PB), and PB to Berlin green (BG) (Ojani et al., 2016), respectively. The first couple of redox peaks (≈ 0.2 V) were attributed to the redox reaction of the high-spin system $\text{Fe}^{3+}/\text{Fe}^{2+}$, which was the reversible redox reaction of PB to PW. On the other hand, the redox pairs were at a more positive potential (≈ 1.0 V) that corresponded to the redox reaction of the low spin $\text{Fe}(\text{CN})_6^{3-/4-}$, which was the reversible reaction of PB to BG. The Berlin green was generated when the applied potential increased (Kong et al., 2015). The equations will be expressed in the following section. The CV peak current of PB-PPy rose significantly, as compared to pristine PB which could be attributed to the synergistic effect of metal-polymer composite and the higher amount of PB which can be deposited on the electrode under the presence of PPy. This phenomenon is presumably due to the adhesion features of PPy itself towards the electrode, which acts as the host for PB nanoparticles to form on it at the surface of the electrode (Hostert et al., 2016). The mechanism of formation of PB-PPy was explained in details in **Section 4.1.1**.

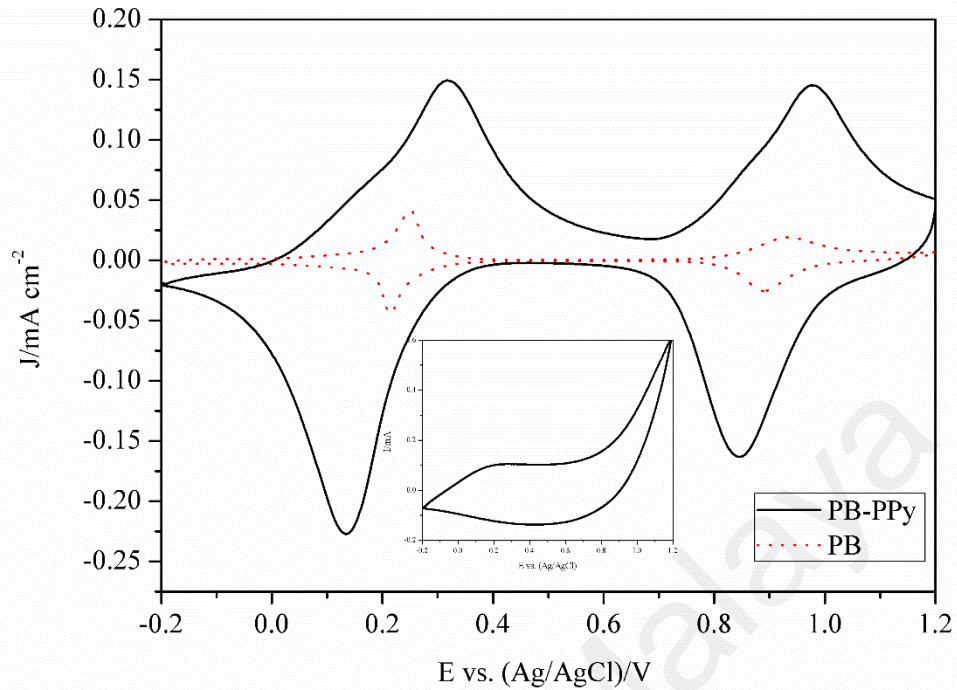
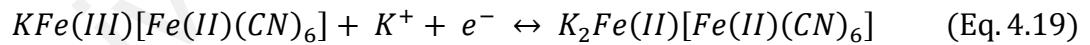


Figure 5.3: Cyclic voltammograms of PB-PPy and PB in 1.0 M KNO₃ as electrolyte. **Insets:** CV of PPy. The potential range was from -0.2 V to 1.2 V with scan rate 50 mV s⁻¹.

As shown in **Figure 5.3**, two redox couples were displayed in the full potential range from -0.2 V to 1.2 V. The overall intercalation of oxidation and reduction of K⁺ ions reaction into PB-PPy can be expressed as (Koncki, 2002):



PB PW



PB BG

In general, there are two types of supercapacitors: electrical double-layer supercapacitors (EDLC) and pseudocapacitors in which the pseudocapacitor has been considered as a transition from EDLC to a battery behaviour. Lately, a new electrochemical behaviour which connects the gap between pseudocapacitive behaviour and the battery behaviour known as intercalation pseudocapacitive behaviour has been introduced (Zukalová, Kalbáč, Kavan, Exnar, & Graetzel, 2005). One of the characteristics of intercalation pseudocapacitive is that the system possesses distinct redox peaks in cyclic voltammograms and hence, its electrochemical profile is identical to the battery. The redox reaction is associated with the intercalation of cations in the crystalline structure of the electrode material. However, the kinetics of the redox reaction (b -value ≈ 1) and the reversibility is higher than the battery which is similar to those classic pseudocapacitors of RuO_2 or MnO_2 (Y. Wang, Song, & Xia, 2016). Therefore, PPy was not discussed here as it did not demonstrate any redox peaks as shown in the **inset** of **Figure 5.3**. Moreover, the PPy here was prepared by electrodeposition method as SA method is unable to form pristine PPy.

Therefore, the pseudocapacitive performances of PB and PB-PPy were studied by a $\log(i) - \log(v)$ plot as shown in **Figure 5.4**. In general, the relationship of current, i and scan rate, v can be summarised as (Augustyn et al., 2013; Y. Wang et al., 2016; Yue et al., 2015). :

$$i = av^b \quad (\text{Eq. 4.21})$$

The b -value that is equal/approximately to 1 is proof that intercalation pseudocapacitive behaviour occurs in the electrode materials (Yue et al., 2015). The b -value of the battery materials is normally at 0.5. A b -value of 0.5 would show that the current is controlled by a semi-infinite linear diffusion whereas a value of 1 indicates that the current is surface-controlled. From **Figure 5.4 (A)**, the b -value obtained for PB is 1,

indicating a main feature of intercalation pseudocapacitance characteristic. For PB-PPy, the b-value of PB-PPy is between 0.7 and 0.8 from 1 to 20 mV s⁻¹ as shown in **Figure 5.4 (B)**. The same b-value had also been reported previously (Augustyn et al., 2013; Yue et al., 2015). The b-value for the scan rate ranging from 1 to 20 mV s⁻¹ is approximately to 1 due to the fact that the kinetics were surface-controlled and hence, indicating it to be rapid (Augustyn et al., 2013).

It can be observed that there are changes in the slope of the anodic and cathodic peaks of PB-PPy in which the b-value reduced when the scan rate increased as indicated in **Figure 5.4 (B)**. This is attributed to several factors, including an increase of ohmic contribution (active material resistance, solid-electrolyte interphase resistance) and/or diffusion limitation (M. Park, Zhang, Chung, Less, & Sastry, 2010).

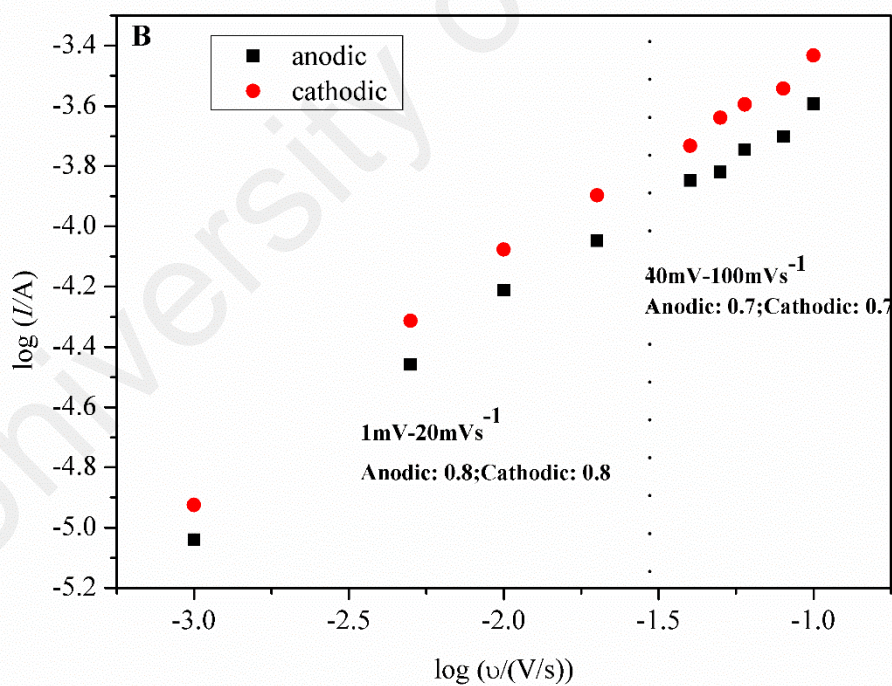
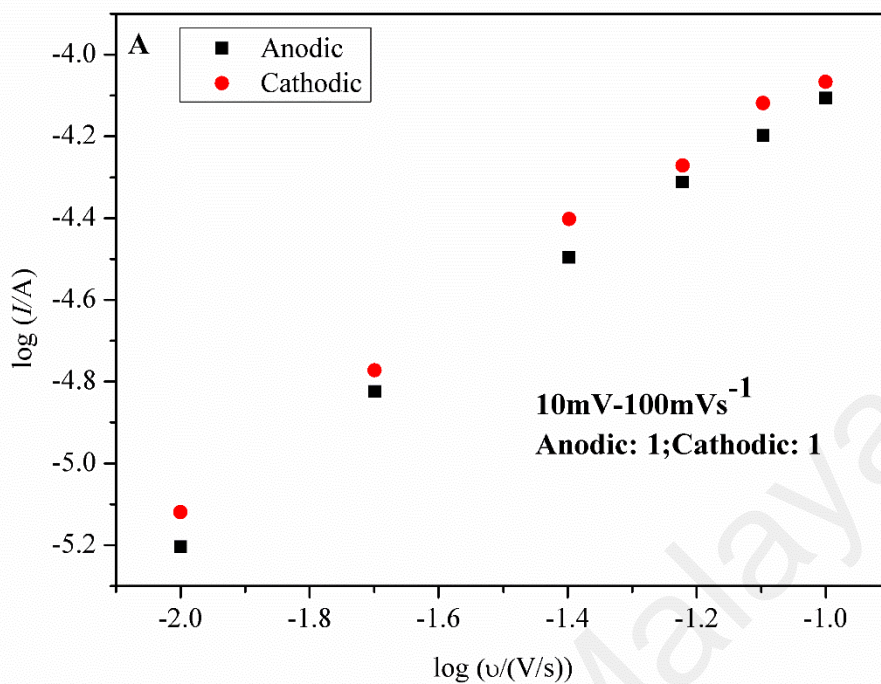


Figure 5.4: Log (i)- log (v) (A) PB and (B) PB-PPy. Determination of b-value from the peak anodic and cathodic current.

5.2.2.1 Galvanostatic charge/discharge test

Furthermore, the performance of the pseudocapacitive materials was also investigated by the GDC at various current densities between 0 to 1.0 V vs. Ag/AgCl as shown in **Figure 5.5**. The potential range of 0 to 1.0 V was selected in order to avoid the gas evolution (Zhong et al., 2015) which might possibly trigger the rupture of the electrochemical supercapacitor cell. It is well known that hydrogen evolution occurs at a negative electrode potential at approximately 0.197 V vs. Ag/AgCl, and oxygen evolution occurs at the positive electrode potential at around 1.033 V (Conway, 1999). From **Figure 5.5**, the voltage-time profile is not the classic triangle shape of an EDLC but similar to those pseudocapacitor which has been reported previously (Jadhav, Pawar, Jadhav, Thorat, & Seo, 2016; Y.Wang et al., 2017; Yue et al., 2015; M.Zhang et al., 2017). This noticeable charge/discharge plateaus were resulted from the non-linear redox reactions that happened at the modified electrode during the charging and discharging which contributed to the pseudocapacitive behaviour (Lei, Markoulidis, Wilson, & Lekakou, 2016; J. H. Park et al., 2002). The plateaus reduced in size at a high current density due to the dominance of an electrical double layer capacitance instead of the contribution of redox reaction towards the pseudocapacitive feature (Xu et al., 2018). The obtained data was reproducible as the relative standard deviation of discharging time in GDC from three different PB-PPy modified electrodes was only 5%.

It can also be seen that the charge and discharge time of PB were significantly lower than PB-PPy as shown in **Figure 5.5 (B)**.

The areal capacitance (F cm^{-2}) is calculated from the following equation (Huang et al., 2013):

$$C = \frac{It}{\Delta V} \quad (\text{Eq. 4.22})$$

Where J is current density ($A\ cm^{-2}$), t is the discharge time (s), and ΔV is the voltage window (V).

Table 5.1: Areal capacitance of PB and PB-PPy calculated from GDC.

Current density (mA cm ⁻²)	Areal capacitance of PB (mF cm ⁻²)	Areal capacitance of PB-PPy (mF cm ⁻²)
0.2	2.3	40.8
0.5	2.1	49.7
1	2.2	36.1
2	2.3	21.4

The capacitance calculated is as shown in **Table 5.1**. The discharge areal capacitance is more than 10 times of the capacitance of the electrode based on pristine PB. This showed that the capacitance was greatly enhanced when PPy was introduced into the nanocomposites.

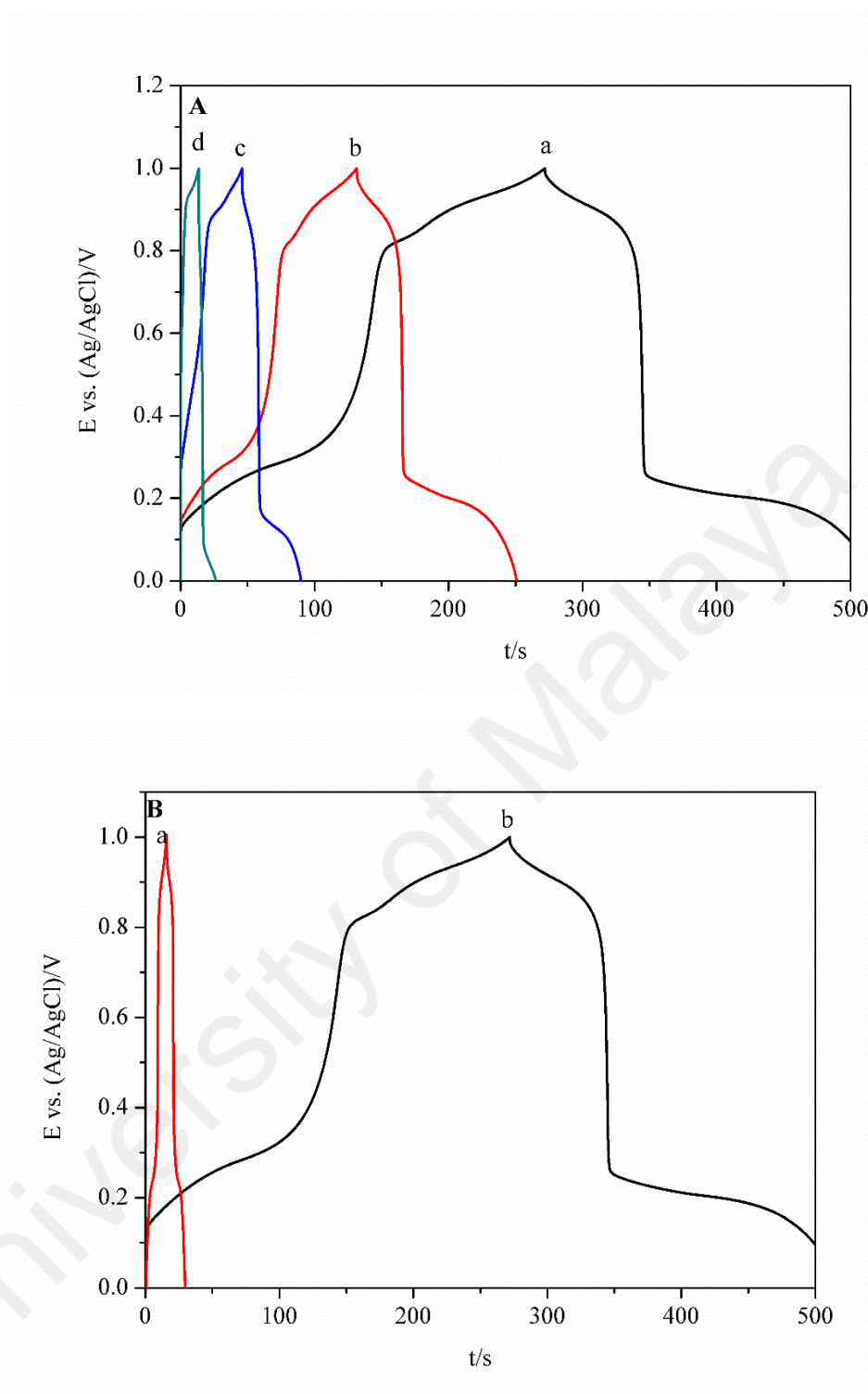


Figure 5.5: Galvanostatic charge/discharge curve (GDC) of (A) PB-PPy at current density (a) 0.2, (b) 0.5, (c) and (d) 2 mA cm⁻²; (B) comparison of (a) PB and (b) PB-PPy at 0.2 mA cm⁻² in 1.0 M KNO₃.

The cyclic stability was analysed by galvanostatic charge/discharge at the same condition over 100 cycles. As shown in **Figure 5.6**, capacitance losses were observed, probably due to the fast cation migration that gradually destroyed the crystal structure of Prussian blue (Yue et al., 2015).

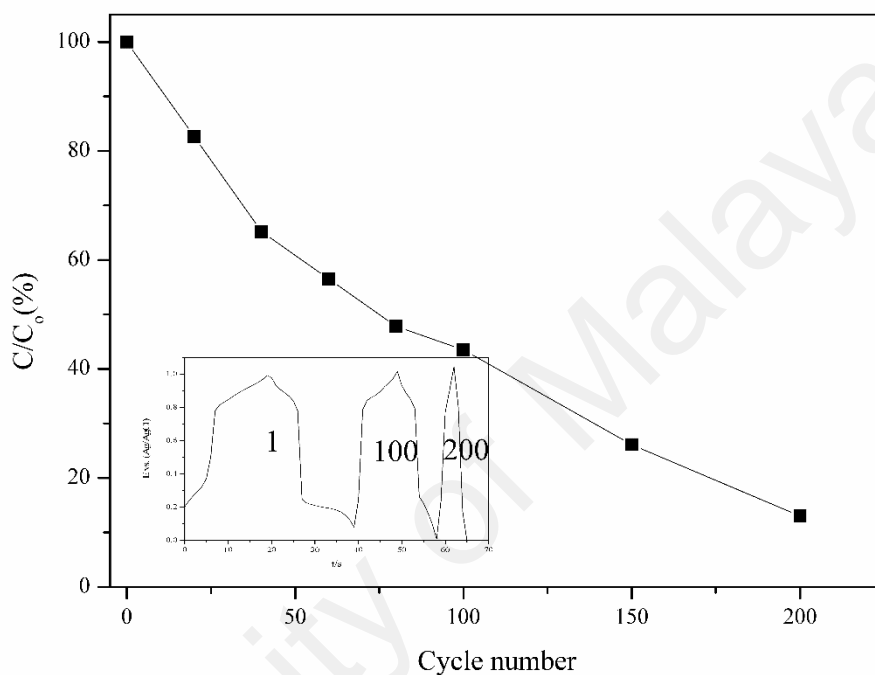


Figure 5.6: Normalised specific capacitances derived from galvanostatic charge/discharge at high current density 2 mA cm^{-2} in 1 M KNO_3 . Inset: Charge/discharge plot at 1, 100 and 200 cycles, respectively.

5.2.2.2 Electrochemical impedance spectroscopy

Electrochemical impedance spectroscopy (EIS) was employed to investigate the characteristic of the modified and bare electrode surface. The frequency ranging from 10 kHz to 0.1 Hz and the amplitude of a sine wave of 5 mV in 0.1 M KNO₃ electrolyte containing 5.0 mM Fe(CN)₆^{4-/3-} was used. Open circuit potential (OCP) was applied in this EIS testing. As shown in the Nyquist plot in **Figure 5.7 (A)**, the semicircle of PB-PPy is the smallest, followed by PB and the bare GCE. It is well-known that the diameter of the semicircle indicates the R_{ct} of the respective electrode. The proposed equivalent circuits are also portrayed in **Figure 5.7 (C)**.

There were three different types of equivalent circuits used to fit the EIS data. Bare GCE was fitted with the simplest Randles circuit due to a semicircle at a high frequency and a straight line at an angle of 45° at a low frequency as seen in its Nyquist plot. However, there were two peaks/ semicircles feature distinguished in the Bode phase of PB and PB-PPy as displayed in **Figure 5.7 (B)**. Hence, their equivalent circuits contain two-time constants (RQ). R_s , R_{ct} and $R_{coating/GCE}$ are the resistance connotations for solution, charge transfer resistances and coating/GCE, respectively. The high frequency solution for resistance R_{sol} is followed by a small semicircle that corresponds to the charge transfer resistor (R_{ct}) which happens across the electrode-electrolyte interface. The second $R_{coating/film}$ is due to passage of K⁺ ions through the passivation film of PB-PPy which covered on electrode surface (Lvovich, 2012).

For the fitting of PB, a Warburg diffusion (W) element was added in the equivalent circuit due to a straight line at an approximate 45° which was seen in the Nyquist plot at the low frequency area. This element is used to explain the movement of ions to the electrode surface. On the other hand, a hyperbolic tangent, T, was used in equivalent circuit of PB-PPy as a straight line at approximately 90° in the low frequency region of

Nyquist plot. In addition, knee frequency is only observed in the Nyquist plot of PB-PPy as shown in **Figure 5.7 (A)**. Knee frequency is defined as the point that divides the high-frequency component from the low-frequency component (Taberna et al., 2003). This indicates that the whole capacitance is archived at 398 mHz. The fitted data is shown in **Table 5.2**.

Table 5.2: EIS parameters acquired by equivalent fitting.

	R_{sol} (Ω)	R_{ct} ($k\Omega$)	Y_o (μMho)	N	$R_{coating}$ ($k\Omega$)	Y_o (μMho)	N	W/T(mho)	B
Bare	240	-	-	-	2.15	1.79	0.828	1.41	-
PB	100	0.23	0.63	0.62	1.14	256	0.93	1.75	-
PB-PPy	230	0.023	0.15	1	1.4	18.1	0.273	10.3	1.3

From the EIS results, it can be concluded the R_{ct} of PB-PPy is the lowest which is presumably an attribution to higher conductivity with the presence of conducting polymers, PPy.

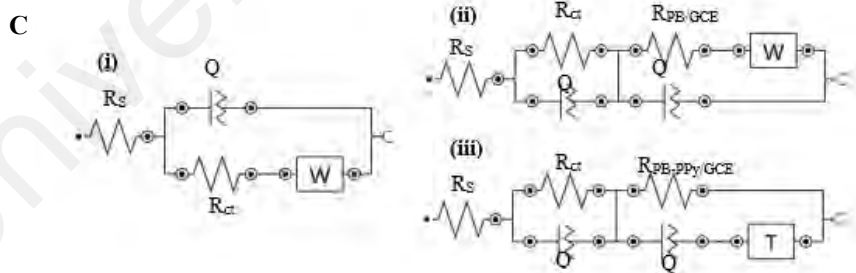
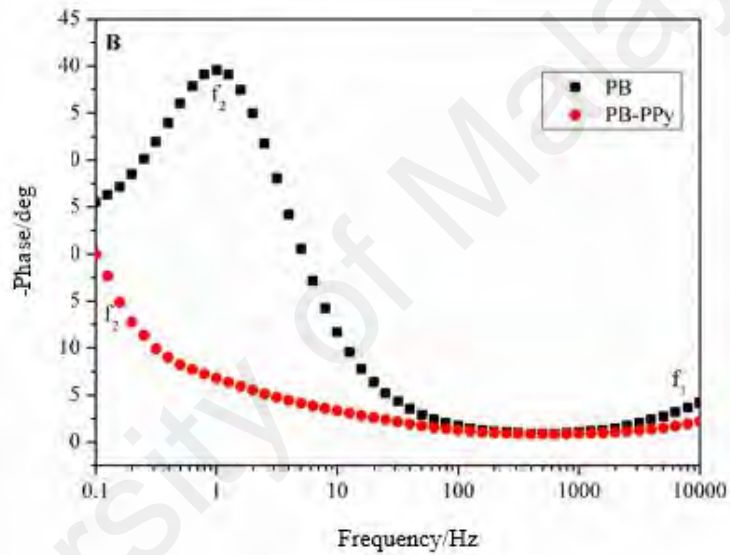
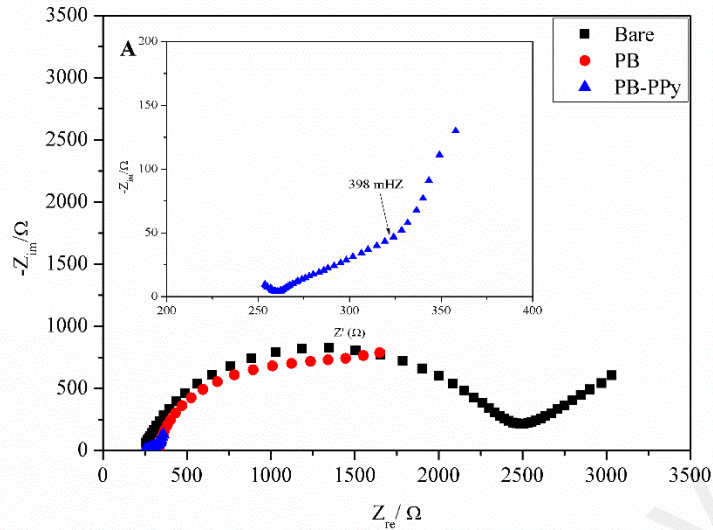


Figure 5.7: (A) Nyquist plot of bare GCE, PB and PB-PPy. Inset: Magnification of Nyquist plot of PB-PPy. (B) Bode plot of PB and PB-PPy (C) Equivalent circuit for (i) bare GCE, (ii) PB and (iii) PB-PPy-modified electrode.

5.3 Limitation of the study

In the nicotine electrochemical sensor studies, the high overpotential for nicotine detection leads to interference of other molecules: The operating potential for CuHCF-PPy nanocomposite for nicotine sensing was +0.85 V vs. Ag/AgCl (sat. KCl). Although this potential is within the range (+0.70 V to +0.93 V vs. Ag/AgCl (sat. KCl)) of other reported electrochemical nicotine sensor, there was interference from other molecules such as H₂O₂. Therefore, the applicability of CuHCF-PPy nanocomposites as electrochemical sensors in real applications which involved more complex sample remains to be further explored.

At the quest to venture into energy storage materials via the SA method, the mass loading on the electrode surface was too low for practical energy storage materials (electrochemical capacitor or battery) application. The current mass loading of PB-PPy nanocomposite was 0.001 mg cm⁻² based on estimated calculation. High mass loading (>1 mg cm⁻²) is more suitable at the device level as the higher the percentage for active material, the more energy the device can store. In short, the high performance of electrochemical capacitors at device level relies on the total mass. In this study, the capacitance of self-assembled PB-PPy nanocomposite was expressed in areal capacitance (F cm⁻²) due the mass loading is too low. It is worth to mention that there were some studies reported in areal capacitance form (Huang et al., 2013; K. Wang, Wu, Meng, Zhang, & Wei, 2012). Nonetheless, the capacitance of all similar MeHCF-based materials was expressed in specific capacitance, C_{sp} (F g⁻¹) form.

REFERENCES

- Abd Mutalib, M., Rahman, M. A., Othman, M. H. D., Ismail, A. F., & Jaafar, J. (2017). Scanning Electron Microscopy (SEM) and Energy-Dispersive X-Ray (EDX) Spectroscopy. In *Membrane Characterization* (pp. 161–179). Elsevier.
- Amand, L. E., & Tullin, C. J. (1999). The Theory Behind FTIR analysis. Retrieved June 18, 2019, from Dep. of Energy Conversion, Chalmers University of Technology, Sweden website: http://turroserver.chem.columbia.edu/pdf_db/theory_ftir.pdf
- Amarnath, C. A., & Sawant, S. N. (2019). Tailoring synthesis strategies for polyaniline-prussian blue composite in view of energy storage and H₂O₂ sensing application. *Electrochimica Acta*, *295*, 294–301.
- Anuar, N. S., Basirun, W. J., Ladan, M., Shalauddin, M., & Mehmood, M. S. (2018). Fabrication of platinum nitrogen-doped graphene nanocomposite modified electrode for the electrochemical detection of acetaminophen. *Sensors and Actuators, B: Chemical*, *266*, 375–383.
- Augustyn, V., Come, J., Lowe, M. A., Kim, J. W., Taberna, P. L., Tolbert, S. H., ... Dunn, B. (2013). High-rate electrochemical energy storage through Li⁺ intercalation pseudocapacitance. *Nature Materials*, *12*(6), 518–522.
- Azman, N. H. N., Lim, H. N., & Sulaiman, Y. (2016). Effect of electropolymerization potential on the preparation of PEDOT/graphene oxide hybrid material for supercapacitor application. *Electrochimica Acta*, *188*, 785–792.
- Bai, X., & Shiu, K. K. (2015). Spontaneous deposition of prussian blue on reduced graphene oxide - gold nanoparticles composites for the fabrication of electrochemical biosensors. *Electroanalysis*, *27*(1), 74–83.
- Balint, R., Cassidy, N. J., & Cartmell, S. H. (2014). Conductive polymers: Towards a smart biomaterial for tissue engineering. *Acta Biomaterialia*, *10*(6), 2341–2353.
- Bard, A., & Faulkner, L. (2002). *Electrochemical Methods: Fundamentals and Applications*. New York: John Wiley & Sons, Inc.
- Bellezza, F., Cipiciani, A., Costantino, U., & Elena Negozio, M. (2002). Zirconium phosphate and modified zirconium phosphates as supports of lipase. Preparation of the composites and activity of the supported enzyme. *Langmuir*, *18*(23), 8737–8742.
- Borisova, A. V., Karyakina, E. E., Costlier, S., & Karyakin, A. A. (2009). Current-free deposition of prussian blue with organic polymers: Towards improved stability and mass production of the advanced hydrogen peroxide transducer. *Electroanalysis*, *21*(3–5), 409–414.
- Brezesinski, T., Wang, J., Tolbert, S. H., & Dunn, B. (2010). Ordered mesoporous α -MoO₃ with iso-oriented nanocrystalline walls for thin-film pseudocapacitors. *Nature Materials*, *9*(2), 146–151.
- Campbell, F. W., & Compton, R. G. (2010). The use of nanoparticles in electroanalysis:

An updated review. *Analytical and Bioanalytical Chemistry*, 396(1), 241–259.

- Cao, L., Liu, Y., Zhang, B., & Lu, L. (2010). In situ controllable growth of Prussian blue nanocubes on reduced graphene oxide: Facile synthesis and their application as enhanced nanoelectrocatalyst for H₂O₂ reduction. *ACS Applied Materials and Interfaces*, 2(8), 2339–2346.
- Chen, P., Fryling, M. A., & McCreery, R. L. (1995). Electron Transfer Kinetics at Modified Carbon Electrode Surfaces: The Role of Specific Surface Site. *Analytical Chemistry*, 67(18), 3115–3122.
- Chen, S.-M., Li, S.-H., & Thiagarajan, S. (2007). Preparation of Bilayer Platinum and Copper Hexacyanoferrate Hybrid Film Modified Electrode and Its Electrocatalytic Properties. *Journal of The Electrochemical Society*, 154(8), E123–E130.
- Chen, W., Cai, S., Ren, Q. Q., Wen, W., & Zhao, Y. Di. (2012). Recent advances in electrochemical sensing for hydrogen peroxide: A review. *Analyst*, 137(1), 49–58.
- Choi, H. C., Shim, M., Bangsaruntip, S., & Dai, H. (2002). Spontaneous reduction of metal ions on the sidewalls of carbon nanotubes. *Journal of the American Chemical Society*, 124(31), 9058–9059.
- Christensen, P. A., Harriman, A., Neta, P., & Richoux, M. C. (1985). Photo-oxidation of water using Prussian Blue as catalyst. *Journal of the Chemical Society, Faraday Transactions 1: Physical Chemistry in Condensed Phases*, 81(10), 2461–2466.
- Chu, Z., Liu, Y., & Jin, W. (2017). Recent progress in Prussian blue films: Methods used to control regular nanostructures for electrochemical biosensing applications. *Biosensors and Bioelectronics*, 96, 17–25.
- Cinková, K., Dianová, L., Vojs, M., Marton, M., & Švorc, L. (2015). Rapid electrochemical platform for nicotine sensing in cigarettes and chewing gums. *Acta Chimica Slovaca*, 8(2), 166–171.
- Clemente, P. N., Reig García-Galbis, M., & Martínez-Espinosa, R. M. (2018). Effects of the Usage of l-Cysteine (l-Cys) on Human Health. *Molecules*, 23(3), Article#575.
- Conway, B. E. (1999). *Electrochemical Supercapacitors*. Boston, MA: Springer US.
- Damiri, S., Oskoei, Y. M., & Fouladgar, M. (2016). Highly sensitive voltammetric and impedimetric sensor based on an ionic liquid/cobalt hexacyanoferrate nanoparticle modified multi-walled carbon nanotubes electrode for diclofenac analysis. *Journal of Experimental Nanoscience*, 11(18), 1384–1401.
- DeLongchamp, D. M., & Hammond, P. T. (2004). Multiple-color electrochromism from layer-by-layer-assembled polyaniline/Prussian Blue nanocomposite thin films. *Chemistry of Materials*, 16(23), 4799–4805.
- Deng, K., Li, C., Qiu, X., Zhou, J., & Hou, Z. (2015). Synthesis of Cobalt hexacyanoferrate decorated graphene oxide/carbon nanotubes-COOH hybrid and their application for sensitive detection of hydrazine. *Electrochimica Acta*, 174, 1096–1103.

- Derwinska, K., Miecznikowski, K., Koncki, R., Kulesza, P. J., Glab, S., & Malik, M. A. (2003). Application of Prussian Blue Based Composite Film with Functionalized Organic Polymer to Construction of Enzymatic Glucose Biosensor. *Electroanalysis*, *15*(2324), 1843–1849.
- Devadas, B., Yeh, H. T., Chen, S. M., & Piraman, S. (2014). Electrochemical preparation of yttrium hexacyanoferrate on reduced graphene oxide and its application to analgesic drug sensor. *Electroanalysis*, *26*(8), 1712–1720.
- Ding, Y., Hu, Y. L., Gu, G., & Xia, X. H. (2009). Controllable synthesis and formation mechanism investigation of prussian blue nanocrystals by using the polysaccharide hydrolysis method. *Journal of Physical Chemistry C*, *113*(33), 14838–14843.
- Draouil, H., Alvarez, L., Causse, J., Flaud, V., Zaibi, M. A., Bantignies, J. L., ... Cambedouzou, J. (2017). Copper hexacyanoferrate functionalized single-walled carbon nanotubes for selective cesium extraction. *New Journal of Chemistry*, *41*(15), 7705–7713.
- Ensafi, A. A., Ahmadi, N., & Rezaei, B. (2015). Electrochemical preparation and characterization of a polypyrrole/nickel-cobalt hexacyanoferrate nanocomposite for supercapacitor applications. *RSC Advances*, *5*(111), 91448–91456.
- Fekry, A. M., Azab, S. M., Shehata, M., & Ameer, M. A. (2015). A novel electrochemical nicotine sensor based on cerium nanoparticles with anionic surfactant. *RSC Advance*, *5*(64), 51662–51671.
- Ferlay, S., Mallah, T., Ouahès, R., Veillet, P., & Verdaguer, M. (1995). A room-temperature organometallic magnet based on prussian blue. *Nature*, *378*(6558), 701–703.
- Fiorito, P. A., Brett, C. M. A., & Córdoba De Torresi, S. I. (2006). Polypyrrole/copper hexacyanoferrate hybrid as redox mediator for glucose biosensors. *Talanta*, *69*(2 SPEC. ISS.), 403–408.
- Geert-Jan Janssen. (2005). Information on the FESEM (Field-emission Scanning Electron Microscope) Radboud University Nijmegen. Retrieved June 18, 2019, from Fesem website: www.vcbio.science.ru.nl/fesem
- Ghasemi, S., Hosseini, S. R., & Asen, P. (2015). Preparation of graphene/nickel-iron hexacyanoferrate coordination polymer nanocomposite for electrochemical energy storage. *Electrochimica Acta*, *160*, 337–346.
- Gholivand, M. B., Khodadadian, M., & Omid, M. (2013). Amperometric sensor based on a graphene/copper hexacyanoferrate nano-composite for highly sensitive electrocatalytic determination of captopril. *Materials Science and Engineering: C*, *33*(2), 774–781.
- Golsheikh, A. ., Huang, N. M., Lim, H. N., Zakaria, R., & Yin, C. Y. (2013). One-step electrodeposition synthesis of silver-nanoparticle-decorated graphene on indium-tin-oxide for enzymeless hydrogen peroxide detection. *Carbon*, *62*, 405–412.
- Gonales, V. R., Matsubara, E. Y., Rosolen, J. M., & Córdoba De Torresi, S. I. (2011).

Micro/nanostructured carbon composite modified with a hybrid redox mediator and enzymes as a glucose biosensor. *Carbon*, 49(9), 3039–3047.

Gonçales, V. R., Gaitán, M. H., Bragatto, A. de O. P., Soler-Illia, G. J. A. A., Baraldo, L. M., & Córdoba De Torresi, S. I. (2013). Correlation between pore size and reactivity of macro/mesoporous iron and copper hexacyanoferrates for H₂O₂ electrocatalysis. *Journal of Electroanalytical Chemistry*, 706, 48–54.

Goodarzi, Z., Maghrebi, M., Zavareh, A. F., Mokhtari-Hosseini, Z.-B., Ebrahimi-hoseinzadeh, B., Zarmi, A. H., & Barshan-tashnizi, M. (2015). Evaluation of nicotine sensor based on copper nanoparticles and carbon nanotubes. *Journal of Nanostructure in Chemistry*, 5(3), 237–242.

Granqvist, C. G., Avendaño, E., & Azens, A. (2003). Electrochromic coatings and devices: Survey of some recent advances. *Thin Solid Films*, 442(1–2), 201–211.

Griffith, W. P. (1962). Cyanide complexes of the transition metals. *Quarterly Reviews, Chemical Society*, 16(2), 188–207.

Hall, B. J., Wells, C., Allenby, C., Lin, M. Y., Hao, I., Marshall, L., ... Levin, E. D. (2014). Differential effects of non-nicotine tobacco constituent compounds on nicotine self-administration in rats. *Pharmacology Biochemistry and Behavior*, 120, 103–108.

Hara, S., Tanaka, H., Kawamoto, T., Tokumoto, M., Yamada, M., Gotoh, A., ... Sakamoto, M. (2007). Electrochromic thin film of Prussian blue nanoparticles fabricated using wet process. *Japanese Journal of Applied Physics, Part 2: Letters*, 46(36–40).

Hostert, L., Alvarenga, G. de, Marchesi, L. F., Soares, A. L., & Vidotti, M. (2016). One-Pot sonoelectrodeposition of poly(pyrrole)/Prussian blue nanocomposites: Effects of the ultrasound amplitude in the electrode interface and electrocatalytical properties. *Electrochimica Acta*, 213, 822–830.

Hu, Y., Zhang, Z., & Yang, C. (2007). The determination of hydrogen peroxide generated from cigarette smoke with an ultrasensitive and highly selective chemiluminescence method. *Analytica Chimica Acta*, 601(1), 95–100.

Huang, L., Chen, D., Ding, Y., Feng, S., Wang, Z. L., & Liu, M. (2013). Nickel-cobalt hydroxide nanosheets coated on NiCo₂O₄ nanowires grown on carbon fiber paper for high-performance pseudocapacitors. *Nano Letters*, 13(7), 3135–3139.

Husmann, S., Nossol, E., & Zarbin, A. J. G. (2014). Carbon nanotube/Prussian blue paste electrodes: Characterization and study of key parameters for application as sensors for determination of low concentration of hydrogen peroxide. *Sensors and Actuators, B: Chemical*, 192, 782–790.

Hwang, B. J., Santhanam, R., & Lin, Y. L. (2001). Nucleation and growth mechanism of electroformation of polypyrrole on a heat-treated gold/highly oriented pyrolytic graphite. *Electrochimica Acta*, 46(18), 2843–2853.

Iftikhar, F. J., Baker, P. G. L., Baleg, A. M., Ndagili, P. M., Mailu, S. N., & Iwuoha, E.

- I. (2011). Modulation of the interfacial electrochemistry of surfactant-functionalised polypyrrole chemical sensor systems. *Electrochimica Acta*, 56(14), 5214–5221.
- Itaya, K., Ataka, T., & Toshima, S. (1982). Spectroelectrochemistry and Electrochemical Preparation Method of Prussian Blue Modified Electrodes. *Journal of the American Chemical Society*, 104(18), 4767–4772.
- Jadhav, H. S., Pawar, S. M., Jadhav, A. H., Thorat, G. M., & Seo, J. G. (2016). Hierarchical Mesoporous 3D Flower-like $\text{CuCo}_2\text{O}_4/\text{NF}$ for High-Performance Electrochemical Energy Storage. *Scientific Reports*, 6, 2–13.
- Jang, J., & Oh, J. H. (2005). Fabrication of a highly transparent conductive thin film from polypyrrole/poly(methyl methacrylate) core/shell nanospheres. *Advanced Functional Materials*, 15(3), 494–502.
- Jang, S.-C., Hong, S.-B., Yang, H.-M., Lee, K.-W., Moon, J.-K., Seo, B.-K., ... Roh, C. (2014). Removal of Radioactive Cesium Using Prussian Blue Magnetic Nanoparticles. *Nanomaterials*, 4(4), 894–901.
- Jang, S. C., Haldorai, Y., Lee, G. W., Hwang, S. K., Han, Y. K., Roh, C., & Huh, Y. S. (2015). Porous three-dimensional graphene foam/Prussian blue composite for efficient removal of radioactive ^{137}Cs . *Scientific Reports*, 5(1), Article#17510.
- Jiang, H., Chen, Z., Cao, H., & Huang, Y. (2012). Peroxidase-like activity of chitosan stabilized silver nanoparticles for visual and colorimetric detection of glucose. *Analyst*, 137(23), 5560–5564.
- Jin, E., Bian, X., Lu, X., & Wang, C. (2012). Fabrication of multiwalled carbon nanotubes/polypyrrole/Prussian blue ternary composite nanofibers and their application for enzymeless hydrogen peroxide detection. *Journal of Materials Science*, 47(10), 4326–4331.
- Jin, E., Lu, X., Cui, L., Chao, D., & Wang, C. (2010). Fabrication of graphene/prussian blue composite nanosheets and their electrocatalytic reduction of H_2O_2 . *Electrochimica Acta*, 55(24), 7230–7234.
- Jin, W., Toutianoush, A., Pyrasch, M., Schnepf, J., Gottschalk, H., Rammensee, W., & Tiede, B. (2003). Self-Assembled Films of Prussian Blue and Analogues: Structure and Morphology, Elemental Composition, Film Growth, and Nanosieving of Ions. *The Journal of Physical Chemistry B*, 107(44), 12062–12070.
- Jing, Y., Lin, E., Su, X., Liu, Y., Li, H., Yuan, X., ... Fan, Y. (2016). Electrodeposition of Au nanoparticles on poly(diallyldimethylammonium chloride) functionalized reduced graphene oxide sheets for voltammetric determination of nicotine in tobacco products and anti-smoking pharmaceuticals. *RSC Advances*, 6(31), 26247–26253.
- Jing, Y., Yuan, X., Yuan, Q., He, K., Liu, Y., Lu, P., ... Li, G. (2016). Determination of nicotine in tobacco products based on mussel-inspired reduced graphene oxide-supported gold nanoparticles. *Scientific Reports*, 6, 29230–29238.
- Kao, J., Thorkelsson, K., Bai, P., Rancatore, B. J., & Xu, T. (2013). Toward functional nanocomposites: Taking the best of nanoparticles, polymers, and small molecules.

Chemical Society Reviews, 42(7), 2654–2678.

- Karyakin, A. A. (2001). Prussian blue and its analogues: Electrochemistry and analytical applications. *Electroanalysis*, 13(10), 813–819.
- Karyakin, A. A., & Chaplin, M. F. (1994). Polypyrrole-Prussian Blue films with controlled level of doping: codeposition of polypyrrole and Prussian Blue. *Journal of Electroanalytical Chemistry*, 370(1–2), 301–303.
- Karyakin, A. A., Gitelmacher, O. V., & Karyakina, E. E. (1994). A high-sensitive glucose amperometric biosensor based on prussian blue modified electrodes. *Analytical Letters*, 27(15), 2861–2869.
- Karyakin, A. A., Karyakina, E. E., & Gorton, L. (1999). On the mechanism of H₂O₂ reduction at Prussian Blue modified electrodes. *Electrochemistry Communications*, 1(2), 78–82.
- Karyakin, A. A., Karyakina, E. E., & Gorton, L. (2000). Amperometric biosensor for glutamate using Prussian Blue-based “artificial peroxidase” as a transducer for hydrogen peroxide. *Analytical Chemistry*, 72(7), 1720–1723.
- Karyakin, A. A., Puganova, E. A., Budashov, I. A., Kurochkin, I. N., Karyakina, E. E., Levchenko, V. A., ... Varfolomeyev, S. D. (2004). Prussian Blue Based Nanoelectrode Arrays for H₂O₂ Detection. *Analytical Chemistry*, 76(2), 474–478.
- Koncki, R. (2002). Chemical sensors and biosensors based on Prussian blues. *Critical Reviews in Analytical Chemistry*, 32(1), 79–96.
- Kong, B., Selomulya, C., Zheng, G., & Zhao, D. (2015). New faces of porous Prussian blue: interfacial assembly of integrated hetero-structures for sensing applications. *Chemistry Society Review*, 44(22), 7997–8018.
- Kong, B., Tang, J., Wu, Z., Wei, J., Wu, H., Wang, Y., ... Zhao, D. (2014). Ultralight mesoporous magnetic frameworks by interfacial assembly of prussian blue nanocubes. *Angewandte Chemie - International Edition*, 53(11), 2988–2992.
- Kraft, A. (2008). On the Discovery and History of Prussian Blue. *Bulletin History of Chemistry*, 32(2), 61–67.
- Kulesza, P. J., Miecznikowski, K., Malik, M. A., Galkowski, M., Chojak, M., Caban, K., & Wieckowski, A. (2001). Electrochemical preparation and characterization of hybrid films composed of Prussian blue type metal hexacyanoferrate and conducting polymer. *Electrochimica Acta*, 46(26–27), 4065–4073.
- Laviron, E. (1979). General expression of the linear potential sweep voltammogram in the case of diffusionless electrochemical systems. *Journal of Electroanalytical Chemistry*, 101(1), 19–28.
- Leake, L. L. (2006). Electronic noses and tongues. *Food Technology*, 60(6), 96–102.
- Lei, C., Markoulidis, F., Wilson, P., & Lekakou, C. (2016). Phenolic carbon cloth-based electric double-layer capacitors with conductive interlayers and graphene coating.

- Levent, A., Yardim, Y., & Senturk, Z. (2009). Voltammetric behavior of nicotine at pencil graphite electrode and its enhancement determination in the presence of anionic surfactant. *Electrochimica Acta*, 55(1), 190–195.
- Li, H. B., Yu, M. H., Wang, F. X., Liu, P., Liang, Y., Xiao, J., ... Yang, G. W. (2013). Amorphous nickel hydroxide nanospheres with ultrahigh capacitance and energy density as electrochemical pseudocapacitor materials. *Nature Communications*, 4(1), Article#1894.
- Li, X., Zhao, H., Shi, L., Zhu, X., Lan, M., Zhang, Q., & Hugh Fan, Z. (2017). Electrochemical sensing of nicotine using screen-printed carbon electrodes modified with nitrogen-doped graphene sheets. *Journal of Electroanalytical Chemistry*, 784, 77–84.
- Limachi, D. G. B., Gonçales, V. R., Cintra, E. P., & Córdoba De Torresi, S. I. (2013). Controlling hydrophilicity and electrocatalytic properties of metallic hexacyanoferrates/conducting polymers hybrids for the detection of H₂O₂. *Electrochimica Acta*, 110, 459–464.
- Lisko, J. G., Tran, H., Stanfill, S. B., Blount, B. C., & Watson, C. H. (2015). Chemical composition and evaluation of nicotine, tobacco alkaloids, pH, and selected flavors in E-Cigarette cartridges and refill solutions. *Nicotine and Tobacco Research*, 17(10), 1270–1278.
- Liu, S. Q., Xu, J. J., & Chen, H. Y. (2002). Electrochemical behavior of nanosized Prussian blue self-assembled on Au electrode surface. *Electrochemistry Communications*, 4(5), 421–425.
- Liu, X. W., Yao, Z. J., Wang, Y. F., & Wei, X. W. (2010). Graphene oxide sheet-prussian blue nanocomposites: Green synthesis and their extraordinary electrochemical properties. *Colloids and Surfaces B: Biointerfaces*, 81(2), 508–512.
- Liu, Y., Chu, Z., & Jin, W. (2009). A sensitivity-controlled hydrogen peroxide sensor based on self-assembled Prussian Blue modified electrode. *Electrochemistry Communications*, 11(2), 484–487.
- Lorestani, F., Nia, P. M., Alias, Y., & Manan, N. S. A. (2015). One-Step Synthesis of Different Silver-Polyaniline Composite Morphologies for Enzymless Hydrogen Peroxide Detection. *Journal of the Electrochemical Society*, 162(7), B193–B200.
- Luo, M., Dou, Y., Kang, H., Ma, Y., Ding, X., Liang, B., ... Li, L. (2015). A novel interlocked Prussian blue/reduced graphene oxide nanocomposites as high-performance supercapacitor electrodes. *Journal of Solid State Electrochemistry*, 19(6), 1621–1631.
- Lvovich, V. F. (2012). *Impedance spectroscopy: Applications to Electrochemical and Dielectric Phenomena*. Hoboken, NJ, USA: John Wiley & Sons, Inc.
- Maitra, A., Das, A. K., Karan, S. K., Paria, S., Bera, R., & Khatua, B. B. (2017). A Mesoporous High-Performance Supercapacitor Electrode Based on Polypyrrole

Wrapped Iron Oxide Decorated Nanostructured Cobalt Vanadium Oxide Hydrate with Enhanced Electrochemical Capacitance. *Industrial and Engineering Chemistry Research*, 56(9), 2444–2457.

- Makowski, O., Stroka, J., Kulesza, P. J., Malik, M. A., & Galus, Z. (2002). Electrochemical identity of copper hexacyanoferrate in the solid-state: Evidence for the presence and redox activity of both iron and copper ionic sites. *Journal of Electroanalytical Chemistry*, 532(1–2), 157–164.
- Malik, M. A., & Kulesza, P. J. (1996). Preparation and characterization of Ag-intercalated copper hexacyanoferrate films on electrodes. *Electroanalysis*, 8(2), 113–116.
- Martínez-García, R., Knobel, M., Goya, G., Gimenez, M. C., Romero, F. M., & Reguera, E. (2006). Heat-induced charge transfer in cobalt iron cyanide. *Journal of Physics and Chemistry of Solids*, 67(11), 2289–2299.
- Mei, X., & Ouyang, J. (2011). Ultrasonication-assisted ultrafast reduction of graphene oxide by zinc powder at room temperature. *Carbon*, 49(15), 5389–5397.
- Miao, Y., & Liu, J. (2009). Assembly and electroanalytical performance of Prussian blue/polypyrrole composite nanoparticles synthesized by the reverse micelle method. *Science and Technology of Advanced Materials*, 10(2), Article#025001.
- Millward, R. C., Madden, C. E., Sutherland, I., Mortimer, R. J., Fletcher, S., & Marken, F. (2001). Directed assembly of multilayers—the case of prussian blue. *Chemical Communications*, 1(19), 1994–1995.
- Ni, P., Zhang, Y., Sun, Y., Shi, Y., Dai, H., Hu, J., & Li, Z. (2013). Facile synthesis of Prussian blue @ gold nanocomposite for nonenzymatic detection of hydrogen peroxide. *RSC Advances*, 3(36), 15987–15992.
- Nia, P. M., Woi, P. M., & Alias, Y. (2015). Hydrogen peroxide sensor: Uniformly decorated silver nanoparticles on polypyrrole for wide detection range. *Applied Surface Science*, 357, 1565–1572.
- Nia, P. M., Woi, P. M., & Alias, Y. (2017). Facile one-step electrochemical deposition of copper nanoparticles and reduced graphene oxide as nonenzymatic hydrogen peroxide sensor. *Applied Surface Science*, 413, 56–65.
- Nia, P. M., Woi, P. M., Lorestani, F., Mahmoudian, M. R., & Alias, Y. (2015). Electrodeposition of copper oxide/polypyrrole/reduced graphene oxide as a nonenzymatic glucose biosensor. *Sensors and Actuators, B: Chemical*, 209, 100–108.
- Nyström, G., Marais, A., Karabulut, E., Wågberg, L., Cui, Y., & Hamed, M. M. (2015). Self-assembled three-dimensional and compressible interdigitated thin-film supercapacitors and batteries. *Nature Communications*, 6, Article#7259.

- Ojani, R., Hamidi, P., & Raoof, J. B. (2016). Efficient nonenzymatic hydrogen peroxide sensor in acidic media based on Prussian blue nanoparticles-modified poly(o-phenylenediamine)/glassy carbon electrode. *Chinese Chemical Letters*, 27(3), 481–486.
- Oliveira, P. R., Kalinke, C., Mangrich, A. S., Marcolino-Junior, L. H., & Bergamini, M. F. (2018). Copper hexacyanoferrate nanoparticles supported on biochar for amperometric determination of isoniazid. *Electrochimica Acta*, 285, 373–380.
- Oraon, R., De Adhikari, A., Tiwari, S. K., Bhattacharyya, S., & Chandra Nayak, G. (2016). Hierarchical self-assembled nanoclay derived mesoporous CNT/polyindole electrode for supercapacitors. *RSC Advances*, 6(69), 64271–64284.
- Orazem, M. E., & Tribollet, B. (2014). *Electrochemical Impedance Spectroscopy*. Hoboken, NJ, USA: John Wiley & Sons, Inc.
- Özkale, B., Pellicer, E., Zeeshan, M. A., López-Barberá, J. F., Nogués, J., Sort, J., ... Pané, S. (2014). One-pot electrosynthesis of multi-layered magnetic metallopolymer nanocomposites. *Nanoscale*, 6(9), 4683–4690.
- Pajerowski, D. M., Watanabe, T., Yamamoto, T., & Einaga, Y. (2011). Electronic conductivity in Berlin green and Prussian blue. *Physical Review B - Condensed Matter and Materials Physics*, 83(15), 153202.
- Palazzolo, D. L. (2013). Electronic Cigarettes and Vaping: A New Challenge in Clinical Medicine and Public Health. A Literature Review. *Front Public Health*, 1, Article#56.
- Pan, C., Gu, H., & Dong, L. (2016). Synthesis and electrochemical performance of polyaniline @MnO₂/graphene ternary composites for electrochemical supercapacitors. *Journal of Power Sources*, 303, 175–181.
- Pandey, P. C., Pandey, A. K., & Chauhan, D. S. (2012). Nanocomposite of Prussian blue based sensor for l-cysteine: Synergetic effect of nanostructured gold and palladium on electrocatalysis. *Electrochimica Acta*, 74, 23–31.
- Pandey, P. C., Singh, R., & Pandey, Y. (2015). Controlled synthesis of functional Ag, Ag-Au/Au-Ag nanoparticles and their Prussian blue nanocomposites for bioanalytical applications. *RSC Advances*, 5(61), 49671–49679.
- Paolella, A., Faure, C., Timoshevskii, V., Marras, S., Bertoni, G., Guerfi, A., ... Zaghbi, K. (2017). A review on hexacyanoferrate-based materials for energy storage and smart windows: Challenges and perspectives. *Journal of Materials Chemistry A*, 5(36), 18919–18932.
- Park, J. H., Park, O. O., Shin, K. H., Jin, C. S., & Kim, J. H. (2002). An Electrochemical Capacitor Based on a Ni(OH)₂/Activated Carbon Composite Electrode. *Electrochemical and Solid-State Letters*, 5(2), H7–H10.
- Park, M., Zhang, X., Chung, M., Less, G. B., & Sastry, A. M. (2010). A review of conduction phenomena in Li-ion batteries. *Journal of Power Sources*, 195(24), 7904–7929.

- Park, Y. W. (2010). Editorial for the Conducting Polymers for Carbon Electronics themed issue. *Chemical Society Reviews*, 39(7), Article#2352.
- Pasta, M., Wessells, C. D., Liu, N., Nelson, J., McDowell, M. T., Huggins, R. A., ... Cui, Y. (2014). Full open-framework batteries for stationary energy storage. *Nature Communications*, 5(1), Article#3007.
- Pellitero, M. A., Guimerà, A., Kitsara, M., Villa, R., Rubio, C., Lakard, B., ... Del Campo, F. J. (2017). Quantitative self-powered electrochromic biosensors. *Chemical Science*, 8(3), 1995–2002.
- Petovar, B., Khanari, K., & Finšgar, M. (2017). A detailed electrochemical impedance spectroscopy study of a bismuth-film glassy carbon electrode for trace metal analysis. *Analytica Chimica Acta*, 1004, 10–21.
- Planche, M. F., Thiéblemont, J. C., Mazars, N., & Bidan, G. (1994). Kinetic study of pyrrole polymerization with iron (III) chloride in water. *Journal of Applied Polymer Science*, 52(13), 1867–1877.
- Prasanth, R., Shankar, R., Gupta, N., Rana, S., & Ahn, J. H. (2015). Application of carbon nanotubes for resolving issues and challenges on electrochemical capacitors. In *Handbook of Polymer Nanocomposites. Processing, Performance and Application: Volume B: Carbon Nanotube Based Polymer Composites* (pp. 415–446). Berlin, Heidelberg: Springer Berlin Heidelberg.
- Puganova, E. A., & Karyakin, A. A. (2005). New materials based on nanostructured Prussian blue for development of hydrogen peroxide sensors. *Sensors and Actuators, B: Chemical*, 109(1), 167–170.
- Qiu, J. D., Peng, H. Z., Liang, R. P., Li, J., & Xia, X. H. (2007). Synthesis, characterization, and immobilization of Prussian blue-modified Au nanoparticles: Application to electrocatalytic reduction of H₂O₂. *Langmuir*, 23(4), 2133–2137.
- Quik, M., O'Leary, K., & Tanner, C. M. (2008). Nicotine and Parkinson's disease: Implications for therapy. *Movement Disorders*, 23(12), 1641–1652.
- Rapecki, T., Donten, M., & Stojek, Z. (2010). Electrodeposition of polypyrrole-Au nanoparticles composite from one solution containing gold salt and monomer. *Electrochemistry Communications*, 12(5), 624–627.
- Rawool, C. R., Punde, N. S., Rajpurohit, A. S., Karna, S. P., & Srivastava, A. K. (2018). High energy density supercapacitive material based on a ternary hybrid nanocomposite of cobalt hexacyanoferrate/carbon nanofibers/polypyrrole. *Electrochimica Acta*, 268, 411–423.
- Razmi, H., Mohammad-Rezaei, R., & Heidari, H. (2009). Self-assembled prussian blue nanoparticles based electrochemical sensor for high sensitive determination of H₂O₂ in acidic media. *Electroanalysis*, 21(21), 2355–2362.
- Reilly, C. A., & Aust, S. D. (1997). Peroxidase substrates stimulate the oxidation of hydralazine to metabolites which cause single-strand breaks in DNA. *Chemical Research in Toxicology*, 10(3), 328–334.

- Ricci, F., Amine, A., Moscone, D., & Palleschi, G. (2003). Prussian Blue modified carbon nanotube paste electrodes: A comparative study and a biochemical application. *Analytical Letters*, 36(9), 1921–1938.
- Roig, A., Navarro, J., Garcia, J. J., & Vicente, F. (1994). Voltammetric study of the stability of deposited Prussian blue films against successive potential cycling. *Electrochimica Acta*, 39(3), 437–442.
- Rosseinsky, D. R., & Mortimer, R. J. (2001, June 1). Electrochromic systems and the prospects for devices. *Advanced Materials*, Vol. 13, pp. 783–793. John Wiley & Sons, Ltd.
- Safavi, A., Kazemi, S. H., & Kazemi, H. (2011). Electrochemically deposited hybrid nickel-cobalt hexacyanoferrate nanostructures for electrochemical supercapacitors. *Electrochimica Acta*, 56(25), 9191–9196.
- Sahoo, N. G., Jung, Y. C., So, H. H., & Cho, J. W. (2007). Polypyrrole coated carbon nanotubes: Synthesis, characterization, and enhanced electrical properties. *Synthetic Metals*, 157(8–9), 374–379.
- Santos, P. L., Katic, V., Toledo, K. C. F., & Bonacin, J. A. (2018). Photochemical one-pot synthesis of reduced graphene oxide/Prussian blue nanocomposite for simultaneous electrochemical detection of ascorbic acid, dopamine, and uric acid. *Sensors and Actuators, B: Chemical*, 255, 2437–2447.
- Sheng, Q., Zhang, D., Wu, Q., Zheng, J., & Tang, H. (2015). Electrodeposition of Prussian blue nanoparticles on polyaniline coated halloysite nanotubes for nonenzymatic hydrogen peroxide sensing. *Analytical Methods*, 7(16), 6896–6903.
- Sims, M. J., Rees, N. V., Dickinson, E. J. F., & Compton, R. G. (2010). Effects of thin-layer diffusion in the electrochemical detection of nicotine on basal plane pyrolytic graphite (BPPG) electrodes modified with layers of multi-walled carbon nanotubes (MWCNT-BPPG). *Sensors and Actuators, B: Chemical*, 144(1), 153–158.
- Siong, V. L. E., Lai, C. W., Juan, J. C., Lee, K. M., Leo, B. F., & Khe, C. S. (2018). One-step solvothermal synthesis of rGO/TiO₂ nanocomposite for efficient solar photocatalytic degradation of Methylene Blue dye. *Current Nanoscience*, Article#14.
- Smith, C. J., & Hansch, C. (2000). The relative toxicity of compounds in mainstream cigarette smoke condensate. *Food and Chemical Toxicology*, 38(7), 637–646.
- Smits, P., Temme, L., & Thien, T. (1993). The cardiovascular interaction between caffeine and nicotine in humans. *Clinical Pharmacology & Therapeutics*, 54(2), 194–204.
- Somani, P., & Radhakrishnan, S. (2002). Charge transport processes in conducting polypyrrole/Prussian Blue bilayers. *Materials Chemistry and Physics*, 76(1), 15–19.
- Song, N., Zhu, Y., Ma, F., Wang, C., & Lu, X. (2018). Facile preparation of Prussian blue/polypyrrole hybrid nanofibers as robust peroxidase mimics for colorimetric detection of L-cysteine. *Materials Chemistry Frontiers*, 2(4), 768–774.

- Song, Z., Yuan, R., Chai, Y., Yin, B., Fu, P., & Wang, J. (2010). Multilayer structured amperometric immunosensor based on gold nanoparticles and Prussian blue nanoparticles/nanocomposite functionalized interface. *Electrochimica Acta*, 55(5), 1778–1784.
- Suffredini, H. B., Santos, M. C., De Souza, D., Codognoto, L., Homem-de-Mello, P., Honório, K. M., ... Avaca, L. A. (2005). Electrochemical Behavior of Nicotine Studied by Voltammetric Techniques at Boron-Doped Diamond Electrodes. *Analytical Letters*, 38(10), 1587–1599.
- Sumorok, N., & Goldfarb, D. S. (2013). Update on cystinuria. *Current Opinion in Nephrology and Hypertension*, 22(4), 427–431.
- Švorc, L., Stanković, D. M., & Kalcher, K. (2014). Boron-doped diamond electrochemical sensor for sensitive determination of nicotine in tobacco products and anti-smoking pharmaceuticals. *Diamond & Related Materials*, 42, 1–7.
- Taberna, P. L., Simon, P., & Fauvarque, J. F. (2003). Electrochemical Characteristics and Impedance Spectroscopy Studies of Carbon-Carbon Supercapacitors. *Journal of The Electrochemical Society*, 150(3), Article#292.
- Tao, J. Z., Xu, G. R., Hao, H. L., Yang, F. X., Ahn, K. S., & Lee, W. Y. (2013). Poly(m-phenylenediamine)-Prussian blue hybrid film formed by one-step electrochemical deposition for glucose biosensor. *Journal of Electroanalytical Chemistry*, 689, 96–102.
- Tennakone, K., Wickramanayake, S., & Fernando, N. (1987). Photocatalytic properties of cupric ferrocyanide. *Solar Energy Materials*, 16(6), 467–470.
- Thévenot, D. R., Toth, K., Durst, R. A., & Wilson, G. S. (2001). Electrochemical biosensors: Recommended definitions and classification. *Biosensors and Bioelectronics*, 16(1–2), 121–131.
- Tsiafoulis, C. G., Trikalitis, P. N., & Prodromidis, M. I. (2005). Synthesis, characterization and performance of vanadium hexacyanoferrate as electrocatalyst of H₂O₂. *Electrochemistry Communications*, 7(12), 1398–1404.
- Tuo, X., Li, B., Chen, C., Huang, Z., Huang, H., Li, L., & Yu, X. (2016). Facile assembly of polypyrrole/Prussian blue aerogels for hydrogen peroxide reduction. *Synthetic Metals*, 213, 73–77.
- Vlase, L., Filip, L., Mîndruțău, I., & Leucuța, S. E. (2005). Determination of Nicotine From Tobacco By Lc-Ms-Ms. *Studia Universitatis Babes-Bolyai, L*, 19–24.
- Wang, C., Zhang, L., Guo, Z., Xu, J., Wang, H., Shi, H., ... Zhuo, X. (2010). A new amperometric hydrazine sensor based on prussian blue/single-walled carbon nanotube nanocomposites. *Electroanalysis*, 22(16), 1867–1872.
- Wang, F., Wu, X., Yuan, X., Liu, Z., Zhang, Y., Fu, L., ... Huang, W. (2017). Latest advances in supercapacitors: From new electrode materials to novel device designs. *Chemical Society Reviews*, 46(22), 6816–6854.

- Wang, H., Yi, H., Chen, X., & Wang, X. (2014). Asymmetric supercapacitors based on nano-architected nickel oxide/graphene foam and hierarchical porous nitrogen-doped carbon nanotubes with ultrahigh-rate performance. *Journal of Materials Chemistry A*, 2(9), 3223–3230.
- Wang, J. (2006a). *Analytical Electrochemistry* (2nd ed.). New York: Wiley-VCH.
- Wang, J. (2006b). Electrochemical biosensors: Towards point-of-care cancer diagnostics. *Biosensors and Bioelectronics*, 21(10), 1887–1892.
- Wang, J. G., Zhang, Z., Liu, X., & Wei, B. (2017). Facile synthesis of cobalt hexacyanoferrate/graphene nanocomposites for high-performance supercapacitor. *Electrochimica Acta*, 235, 114–121.
- Wang, J., Xu, Y., Yan, F., Zhu, J., & Wang, J. (2011). Template-free prepared micro/nanostructured polypyrrole with ultrafast charging/discharging rate and long cycle life. *Journal of Power Sources*, 196(4), 2373–2379.
- Wang, K., Wu, H., Meng, Y., Zhang, Y., & Wei, Z. (2012). Integrated energy storage and electrochromic function in one flexible device: An energy storage smart window. *Energy and Environmental Science*, 5(8), 8384–8389.
- Wang, Ke, Zhou, C., Xi, D., Shi, Z., He, C., Xia, H., ... Qiao, G. (2015). Component-controllable synthesis of $\text{Co}(\text{S}_x\text{Se}_{1-x})_2$ nanowires supported by carbon fiber paper as high-performance electrode for hydrogen evolution reaction. *Nano Energy*, 18, 1–11.
- Wang, L., Tricard, S., Yue, P., Zhao, J., Fang, J., & Shen, W. (2016). Polypyrrole and graphene quantum dots @ Prussian Blue hybrid film on graphite felt electrodes: Application for amperometric determination of l-cysteine. *Biosensors and Bioelectronics*, 77, 1112–1118.
- Wang, L., Ye, Y., Zhu, H., Song, Y., He, S., Xu, F., & Hou, H. (2012). Controllable growth of Prussian blue nanostructures on carboxylic group-functionalized carbon nanofibers and its application for glucose biosensing. *Nanotechnology*, 23(45), Article#455502.
- Wang, M., Ma, Z., Li, J., Zhang, Z., Tang, B., & Wang, X. (2018). Well-dispersed palladium nanoparticles on nickel-phosphorus nanosheets as efficient three-dimensional platform for superior catalytic glucose electro-oxidation and non-enzymatic sensing. *Journal of Colloid and Interface Science*, 511, 355–364.
- Wang, S. J., Liaw, H. W., & Tsai, Y. C. (2009). Low potential detection of nicotine at multiwalled carbon nanotube-alumina-coated silica nanocomposite. *Electrochemistry Communications*, 11(4), 733–735.
- Wang, W., & Wu, S. (2017). A new ternary composite based on carbon nanotubes/polyindole/graphene with preeminent electrocapacitive performance for supercapacitors. *Applied Surface Science*, 396, 1360–1367.
- Wang, Y., Chang, Z., Zhang, Y., Chen, B., Fu, L., Zhu, Y., ... Wu, Y. (2017). CoCO_3 from one-step micro-emulsion method as electrode materials for Faradaic capacitors.

Scientific Reports, 7(1), 1–8.

- Wang, Y., & Chen, Q. (2014). Dual-layer-structured nickel hexacyanoferrate/MnO₂ composite as a high-energy supercapacitive material based on the complementarity and interlayer concentration enhancement effect. *ACS Applied Materials and Interfaces*, 6(9), 6196–6201.
- Wang, Y., Song, Y., & Xia, Y. (2016). Electrochemical capacitors: mechanism, materials, systems, characterization and applications. *Chemistry Society Review*, 45(21), 5925–5950.
- Wang, Z., Sun, S., Hao, X., Ma, X., Guan, G., Zhang, Z., & Liu, S. (2012). A facile electrosynthesis method for the controllable preparation of electroactive nickel hexacyanoferrate/polyaniline hybrid films for H₂O₂ detection. *Sensors and Actuators, B: Chemical*, 171–172, 1073–1080.
- Wang, Z., Yang, H., Gao, B., Tong, Y., Zhang, X., & Su, L. (2014). Stability improvement of Prussian blue in nonacidic solutions via an electrochemical post-treatment method and the shape evolution of Prussian blue from nanospheres to nanocubes. *Analyst*, 139(5), 1127–1133.
- Wei, M., Wei, K., Ichihara, M., & Zhou, H. (2008). Nb₂O₅ nanobelts: A lithium intercalation host with large capacity and high rate capability. *Electrochemistry Communications*, 10(7), 980–983.
- Winter, M., & Brodd, R. J. (2004). What are batteries, fuel cells, and supercapacitors? *Chemical Reviews*, 104(10), 4245–4269.
- Winzer-Serhan, U. H. (2017). Evaluation of Chronic Oral Nicotine Treatment in Food Consumption, Body Weight and [125I] Epibatidine Binding in Adult Mice. *Open Access Journal of Toxicology*, 1(1). Article#555552.
- Wong, M. H., Zhang, Z., Yang, X., Chen, X., & Ying, J. Y. (2015). One-pot in situ redox synthesis of hexacyanoferrate/conductive polymer hybrids as lithium-ion battery cathodes. *Chemical Communications*, 51(71), 13674–13677.
- Wu, N., She, X., Yang, D., Wu, X., Su, F., & Chen, Y. (2012). Synthesis of network reduced graphene oxide in polystyrene matrix by a two-step reduction method for superior conductivity of the composite. *Journal of Materials Chemistry*, 22(33), 17254–17261.
- Xu, J., Liao, K., Song, K., Wu, J., Hu, X., Gao, H., ... Cheng, J. P. (2018). Fast in situ synthesis of CoFe layered double hydroxide onto multi-layer graphene for electrochemical capacitors. *Journal of Solid State Electrochemistry*, 22(4), 1037–1045.
- Yang, B., Bin, D., Zhang, K., Du, Y., & Majima, T. (2018). A seed-mediated method to design N-doped graphene supported gold-silver nanothorns sensor for rutin detection. *Journal of Colloid and Interface Science*, 512, 446–454.
- Yang, C. Y., Chang, M. H., Chen, S. M., & Devadas, B. (2016). Amperometric determination of nicotine using a composite of palladium hexacyanoferrate

incorporated graphene oxide modified electrode. *International Journal of Electrochemical Science*, 11(4), 2650–2658.

Yang, G., Cui, H., Yang, G., & Wang, C. (2014). Self-Assembly of $\text{Co}_3\text{V}_2\text{O}_8$ multilayered nanosheets: Controllable synthesis, excellent li-storage properties, and investigation of electrochemical mechanism. *ACS Nano*, 8(5), 4474–4487.

Yang, T., Gao, Y., Liu, Z., Xu, J., Lu, L., & Yu, Y. (2017). Three-dimensional gold nanoparticles/prussian blue-poly(3,4-ethylenedioxythiophene) nanocomposite as novel redox matrix for label-free electrochemical immunoassay of carcinoembryonic antigen. *Sensors and Actuators, B: Chemical*, 239, 76–84.

Yang, Y., Hao, Y., Yuan, J., Niu, L., & Xia, F. (2015). In situ co-deposition of nickel hexacyanoferrate nanocubes on the reduced graphene oxides for supercapacitors. *Carbon*, 84(1), 174–184.

Yang, Z., Zheng, X., & Zheng, J. (2016). Facile synthesis of prussian blue/hollow polypyrrole nanocomposites for enhanced hydrogen peroxide sensing. *Industrial and Engineering Chemistry Research*, 55(46), 12161–12166.

Ye, D., Luo, L., Ding, Y., Chen, Q., & Liu, X. (2011). A novel nitrite sensor based on graphene/polypyrrole/chitosan nanocomposite modified glassy carbon electrode. *The Analyst*, 136(21), Article#4563.

You, Y., Yao, H.-R., Xin, S., Yin, Y.-X., Zuo, T.-T., Yang, C.-P., ... Goodenough, J. B. (2016). Subzero-Temperature Cathode for a Sodium-Ion Battery. *Advanced Materials*, 28(33), 7243–7248.

Yue, Y., Zhang, Z., Binder, A. J., Chen, J., Jin, X., Overbury, S. H., & Dai, S. (2015). Hierarchically superstructured Prussian blue analogues: Spontaneous assembly synthesis and applications as pseudocapacitive materials. *ChemSusChem*, 8(1), 177–183.

Zhai, C., Sun, X., Zhao, W., Gong, Z., & Wang, X. (2013). Acetylcholinesterase biosensor based on chitosan/prussian blue/multiwall carbon nanotubes/hollow gold nanospheres nanocomposite film by one-step electrodeposition. *Biosensors and Bioelectronics*, 42(1), 124–130.

Zhai, J., Zhai, Y., Wen, D., & Dong, S. (2009). Prussian blue/multiwalled carbon nanotube hybrids: Synthesis, assembly and electrochemical behavior. *Electroanalysis*, 21(20), 2207–2212.

Zhai, X., Wei, W., Zeng, J., Liu, X., & Gong, S. (2006). New nanocomposite based on prussian blue nanoparticles/carbon nanotubes/chitosan and its application for assembling of amperometric glucose biosensor. *Analytical Letters*, 39(5), 913–926.

Zhang, M., Hou, C., Halder, A., Ulstrup, J., & Chi, Q. (2017). Interlocked graphene–Prussian blue hybrid composites enable multifunctional electrochemical applications. *Biosensors and Bioelectronics*, 89, 570–577.

Zhang, R. Z., Pan, B. G., Wang, H. N., Dan, J. M., Hong, C. L., & Li, H. L. (2015). Polydopamine and graphene oxide synergistically modified Prussian blue

electrochemical immunosensor for the detection of alpha-fetoprotein with enhanced stability and sensibility. *RSC Advances*, 5(48), 38176–38182.

Zhang, W., Wang, L., Zhang, N., Wang, G., & Fang, B. (2009). Functionalization of single-walled carbon nanotubes with cubic Prussian blue and its application for amperometric sensing. *Electroanalysis*, 21(21), 2325–2330.

Zhang, X., Tao, L., He, P., Zhang, X., He, M., Dong, F., ... Zhang, Y. (2018). A novel cobalt hexacyanoferrate/multi-walled carbon nanotubes nanocomposite: Spontaneous assembly synthesis and application as electrode materials with significantly improved capacitance for supercapacitors. *Electrochimica Acta*, 259, 793–802.

Zhang, X. Z., Zhou, Y., Zhang, W., Zhang, Y., & Gu, N. (2016). Polystyrene@Au@prussian blue nanocomposites with enzyme-like activity and their application in glucose detection. *Colloids and Surfaces A: Physicochemical and Engineering Aspects*, 490, 291–299.

Zhang, Y., Chen, H., Gao, X., Chen, Z., & Lin, X. (2012). A novel immunosensor based on an alternate strategy of electrodeposition and self-assembly. *Biosensors and Bioelectronics*, 35(1), 277–283.

Zhang, Y., Chu, Z., Shi, L., & Jin, W. (2011). Effect of temperature-controlled poly(diallyldimethylammonium chloride) on morphology of self-assembled Prussian Blue electrode and its high detection sensitivity of hydrogen peroxide. *Electrochimica Acta*, 56(24), 8163–8167.

Zhang, Y., Sun, X., Zhu, L., Shen, H., & Jia, N. (2011). Electrochemical sensing based on graphene oxide/Prussian blue hybrid film modified electrode. *Electrochimica Acta*, 56(3), 1239–1245.

Zhao, H., Yuan, Y., Adeloju, S., & Wallace, G. G. (2002). Study on the formation of the Prussian blue films on the polypyrrole surface as a potential mediator system for biosensing applications. *Analytica Chimica Acta*, 472(1–2), 113–121.

Zhao, J., Liu, J., Tricard, S., Wang, L., Liang, Y., Cao, L., ... Shen, W. (2015). Amperometric detection of hydrazine utilizing synergistic action of prussian blue @ silver nanoparticles / graphite felt modified electrode. *Electrochimica Acta*, 171, 121–127.

Zhao, J., Yue, P., Tricard, S., Pang, T., Yang, Y., & Fang, J. (2017). Prussian blue (PB)/carbon nanopolyhedra/polypyrrole composite as electrode: a high performance sensor to detect hydrazine with long linear range. *Sensors and Actuators, B: Chemical*, 251, 706–712.

Zhao, W., Xu, J. J., Shi, C. G., & Chen, H. Y. (2005). Multilayer membranes via layer-by-layer deposition of organic polymer protected prussian blue nanoparticles and glucose oxidase for glucose biosensing. *Langmuir*, 21(21), 9630–9634.

Zheng, Y., Qiao, J., Yuan, J., Shen, J., Wang, A. jun, & Niu, L. (2017). Electrochemical Removal of Radioactive Cesium from Nuclear Waste Using the Dendritic Copper Hexacyanoferrate/Carbon Nanotube Hybrids. *Electrochimica Acta*, 257, 172–180.

- Zhong, C., Deng, Y., Hu, W., Qiao, J., Zhang, L., & Zhang, J. (2015). A review of electrolyte materials and compositions for electrochemical supercapacitors. *Chemistry Society Review*, 44(21), 7484–7539.
- Zolotukhina, E. V., Bezverkhy, I. S., & Vorotyntsev, M. A. (2014). One-stage periodical anodic-cathodic double pulse deposition of nanocomposite materials. Application to Prussian Blue/polypyrrole film coated electrodes. *Electrochimica Acta*, 122, 247–258.
- Zou, Y., Sun, L. X., & Xu, F. (2007a). Biosensor based on polyaniline-Prussian Blue/multi-walled carbon nanotubes hybrid composites. *Biosensors and Bioelectronics*, 22(11), 2669–2674.
- Zou, Y., Sun, L., & Xu, F. (2007b). Prussian Blue electrodeposited on MWNTs-PANI hybrid composites for H₂O₂ detection. *Talanta*, 72(2), 437–442.
- Zou, Y., Wang, Q., Xiang, C., She, Z., Chu, H., Qiu, S., ... Sun, L. (2016). One-pot synthesis of ternary polypyrrole-Prussian-blue-graphene-oxide hybrid composite as electrode material for high-performance supercapacitors. *Electrochimica Acta*, 188, 126–134.
- Zukalová, M., Kalbáč, M., Kavan, L., Exnar, I., & Graetzel, M. (2005). Pseudocapacitive lithium storage in TiO₂ (B). *Chemistry of Materials*, 17(5), 1248–1255.
- Zuo, Y., Zhang, L., Wu, J., Fritz, J. W., Medeiros, S., & Rego, C. (2004). Ultrasonic extraction and capillary gas chromatography determination of nicotine in pharmaceutical formulations. *Analytica Chimica Acta*, 526(1), 35–39.

LIST OF PUBLICATIONS AND PAPERS PRESENTED

PUBLICATIONS

1. **Lee, P.K.**, Nia, P.M, Woi, P.M. (2017). Facile self-assembled Prussian blue-polypyrrole nanocomposites on glassy carbon: Comparative synthesis methods and its electrocatalytic reduction towards H₂O₂, *Electrochimica Acta*, 246, 841-852.
2. **Lee, P.K.**, Woi, P.M. (2019). Direct self-assembly of CuHCF-PPy nanocomposites on rGO for amperometric nicotine sensing at high concentration range, *Journal of Electroanalytical Chemistry*, 837, 67-75.
3. **Lee, P.K.**, Nia, P.M, Woi, P.M. (2019). Self-assembled Prussian blue-polypyrrole nanocomposites for energy storage application , Short Communication, *Journal of Applied Electrochemistry*, 49(6), 631-638.
4. **Lee, P.K.**, Woi, P.M. (2019). Current innovations of metal hexacyanoferrates-based nanocomposites towards electrochemical sensing: Materials selection and synthesis methods. *Critical Reviews in Analytical Chemistry*, 1-12.

PAPER PRESENTED

1. Oral presentation, “Facile self-assembled Prussian-blue-polypyrrole nanocomposites on glassy carbon: Electrocatalyst towards H_2O_2 and its pseudocapacitive behaviour”, Nanotech Malaysia 2018 in UTM KL, 7-9 May 2018.
2. Poster presentation, “Designing metals hexacyanoferrate nanocomposites: A comparative synthesis and its multifunctional electrochemical applications”, SOKENDAI Asian Winter School 2018 in Institute of Molecular Science, Japan.
3. Poster presentation, “Designing metals hexacyanoferrate nanocomposites: A comparative synthesis and its multifunctional electrochemical applications”, UM-NTU bilateral symposium, University of Malaya. 13 August 2018.